

$\text{J g}^{-1} \text{K}^{-1}$ for all three cathode types. It was shown that the total heat generated inside the batteries increases with increasing amount of electrical energy stored. The maximum total internal heat generated by fully-charged LIBs was found to be 37.3 ± 3.3 , 34.0 ± 1.8 and 13.7 ± 0.4 kJ/cell for LCO, NMC and LFP LIBs, respectively. Additionally, experiments were carried out in which the CSBC technique was combined with cone calorimetry to measure the heat produced in flaming combustion of vented battery materials. The released combustion heat did not show a clear dependence on the stored electrical energy; this heat varied between 35 and 63 kJ/cell for LCO LIBs, 27 and 81 kJ/cell for NMC LIBs, and 36 and 50 kJ/cell for LFP LIBs. Beyond the experimental work, detailed modeling of heat transfer in the CSBC experiments was carried out, by utilizing COMSOL Multiphysics software, to evaluate thermal conductivities of the LIBs and demonstrate the satisfactory accuracy of CSBC experimental analysis in the determination of the battery failure energetics for all examined battery types.

Moreover, it is presented in this study a general methodology to develop a thermo-kinetic model of thermally-induced failure of lithium ion batteries (LIBs), using COMSOL and experimental data collected by CSBC. This methodology is demonstrated specifically on LCO LIBs (T-Energy ICR18650), but it can be easily extended to other battery types. The model was parameterized based on Arrhenius' Law and via an iterative inverse modeling analysis of CSBC test results using COMSOL. These model parameters are dependent on the cells' states of charge (SOCs) and they can effectively represent the tested cells' heat production energetics during failure. The fully-parameterized thermo-kinetic model was then validated against CSBC tests that were not utilized in the model parameterization: CSBC tests on 100% SOC LIB cell with non-standard heating rates ranging from 40 W to 100 W; and CSBC tests on 75% SOC LIB cell with a standard heating rate of 20 W. The agreements between the experimentally measured and

the simulated copper slug temperature histories in these tests were found within in 5% on average. Last but not least, this model was applied to predict the thermally-induced failure of LIB cells in a more complex scenario – cascading LIB failure of 6 LIB cells in a billiard battery pack. The simulated onset time of thermal runaway of each LIB cell in the battery pack were found of excellent agreements with experimental observations.

COMPREHENSIVE CALORIMETRY AND MODELING OF THE THERMALLY-
INDUCED FAILURE OF A LITHIUM ION BATTERY

By

Xuan Liu

Dissertation submitted to the Faculty of the Graduate School of the
University of Maryland, College Park, in partial fulfillment
of the requirements for the degree of
Doctor of Philosophy
2016

Advisory Committee:

Professor Stanislav I. Stoliarov, Chair
Professor Chunsheng Wang, Dean's Representative
Dr. Richard E. Lyon
Professor James A. Milke
Professor Marino diMarzo
Professor Andre W. Marshall

© Copyright by
Xuan Liu
2016

Dedication

To my family

Tongfu Liu, Chuanhua Zhou

Xianda Gu, Yulan Zhai

and most importantly, to:

Yikang “Yuki” Gu (my dear wife)

Angela Yunrui Liu (my lovely daughter)

Acknowledgements

First of all, I'd like to thank my family. My father Tongfu Liu has been my lifetime model, who teaches me how important it is to have a sense of responsibility no matter what I am doing. My mother Chuanhua Zhou, has been a great adviser and supporter, whenever I have encountered challenges, her advice is always encouraging. My father in law, Xianda Gu, is the most kind-hearted man I have ever met, he's always shown incredible amount of support to me and my wife, he teaches me to be optimistic and open-minded all the time. My mother in law, Yulan Zhai also deserves a lot of appreciations. She's a warm hearted but quiet lady, she's offered great help to me, especially after my daughter was born. She's been taking care of Angela during the most final year of my Ph.D program, which was greatly helpful to me so that I could concentrate to my work. Most importantly, I'd like to thank my beautiful wife, Yikang "Yuki" Gu. I really appreciate Yikang's great trust to me. She followed me to the US from the very beginning of my Ph.D program, we learned cooking together, we explored good restaurants in DC area together, we traveled to different places together, and I appreciate every single moment that we shared our joy and sometimes frustrations in this foreign country. The great journey we've come along, is just unforgettable! No words can ever be enough to describe this incredible experience, and I believe the upcoming life journey with her will even be more awesome! Last but not least, to my lovely daughter, Angela Yunrui Liu: daddy thank you for you coming to my life. The happiness you have brought to me has been great and I promise I will take good care of you!

I feel extremely lucky that I have met a lot of nice people during my 6 years at University of Maryland and I have become very good friends with many of them. Derrick Ko has given me great help in my heat transfer class in the first year I came here (I transferred from

Electric Engineering to Fire Protection Engineering/Mechanical Engineering), which truly meant a lot to me. We became very good friends later and I wish him best of luck to his Ph.D. Mark McKinnon is one of my closest friends in my research group. He's helped me understand American culture with his great patience and he's also been greatly helpful in my research. I'm sure he will make great contributions in his field in the upcoming years. Jing Li also deserves special thanks, he's been very kind to share with me his insightful opinions in his research topic, which was truly helpful. Paul Anderson is another close friend of mine, we've shared a lot of opinions in raising kids, cultural difference between China and America, funny things in our daily life and more. It's been great! Fernando Raffan is also a good friend I want to thank. He's never hesitant to help me and provide me guidelines for my research. To all of other groupmates in my long list: Mollie Semmes, Tom Feng, Cameron Novak, Kevin Kover, Xi Ding, Yan Ding, Zhibo Wu, Cara Hamel, Geri Martin, Joshua Swann, Yinghui Zheng, Ryan Fisher, Taylor Mayer, James White, Isaac Leventon, Haiqing Guo, Wei Tang, Cong Zhang, John Pagliaro, Jo Hannes, etc. This journey has been great because all of you, thank you!

I'd like to thank all the great professors whose class I was sitting in: Prof. Jungho Kim, Prof. Peter B. Sunderland, Prof. James Milke, Prof. Arnaud Trouve, Prof. Marshall, Prof. Bao Yang and Prof. Chunsheng Wang. The knowledge that they generously delivered to me had helped form a solid foundation for my research at University of Maryland. The valuable advice given by and the stimulating discussions with Dr. Richard Lyon, Prof. James Quintiere and Dr. Richard Walters were also of great help. I'm very thankful to their advice. I'd also like to thank the amazing staff members at school: Patricia Baker, Sharon Hodgson, Mary Lou, Olga Zeller, Kerri Poppler James, Christine O'Brien, Nicole Hollywood. Life at school was so much easier with all of your help, thank you!

Ford Motor Co. and FAA were the funding sources of my Ph.D project. I'd like to thank them for their financial support and motivations provided throughout.

My dissertation committee deserves acknowledgement for their valuable comments and help that have certainly helped improve this study. The committee consists of the following people: Prof. Chunsheng Wang, Dr. Richard Lyon, Prof. James Milke, Prof. Marino diMarzo, Prof. Andre Marshall.

Most importantly, my advisor, Dr. Stanislav I. Stoliarov deserves the most significant acknowledgement. Dr. Stas is the person who led me to the beautiful world of fire safety research. I sincerely thank him for the great opportunities he has brought to me. I'm truly grateful for the time, motivation, valuable advice, profound comments that he has provided to this project. I've learned from his great work ethic and I'm sure it will be helpful to me for my professional career in the upcoming years. Dr. Stas' understanding and support to me has been extremely encouraging and helpful! Without him, I can't achieve what I have during my 6 years at Maryland. No words can express how grateful I am to him. I'm sure he will keep making great contributions to fire safety research, and I wish Dr. Stas best of luck!

Table of Contents

Dedication	ii
Acknowledgements.....	iii
Table of Contents	vi
List of Tables	ix
List of Figures	x
Nomenclature	xv
Chapter 1: Introduction	1
1.1 Background and Motivation	1
1.2 Previous Experimental Study on Battery Failure	5
1.3 Previous Modeling Study on Battery Failure.....	8
1.4 Scope of Current Study.....	15
Chapter 2: Experimental Methods	18
2.1 Battery Samples	18
2.2 Copper Slug Battery Calorimetry	20
2.3 Power Loss Calibration.....	22
2.4 CSBC Tests to Measure Internal Heat Generation	22
2.5 CSBC Tests to Measure Radial Thermal Conductivity of LIBs.....	24
2.6 CSBC Tests to Measure External Flaming Heat.....	25
2.7 CSBC Tests in Nitrogen Atmosphere	26
2.8 CSBC Tests for Battery Failure Model Validation.....	28
2.9 Cascading Battery Failure Tests	28
Chapter 3: Experimental Data Analysis.....	32

3.1 CSBC Governing Equation.....	32
3.2 CSBC Power Loss Calibration.....	33
3.3 LIB Heat Capacity and Mass	36
Chapter 4: Experimental Results	46
4.1 Timing and Temperature of LIBs’ Thermally-induced Failure.....	46
4.2 Internal Heat Generation.....	50
4.3 Temperature Measurements for Radial Thermal Conductivity of LIBs.....	57
4.4 External Flaming Combustion Heat.....	58
4.5 CSBC Test in Nitrogen Atmosphere.....	64
4.6 CSBC Tests for Model Validations	65
4.6.1 LCO LIBs at 100% SOC Heated by a Range of Heating Rates	65
4.6.2 CSBC Tests on LCO LIBs at 75% SOC.....	67
4.7 Cascading Battery Failure Tests	68
Chapter 5: Numerical Modeling for CSBC Validation.....	73
5.1 Model Construction	73
5.2 Radiative Heat Loss from CSBC to Ambient Air.....	75
5.3 Convective Heat Loss from CSBC to Ambient Air.....	76
5.4 Thermal Conductivity of the Insulation Material	77
5.5 Radial Thermal Conductivity of LIB Cells.....	80
5.6 Validation of Internal Heat Generation Measurements by CSBC.....	82
Chapter 6: Thermo-Kinetic Modeling of Battery Thermal Failure.	88
6.1 Modeling Methodology	88
6.2 Thermo-Kinetic Battery Failure Model Construction and Parameterization.....	89

6.3 Thermo-Kinetic Battery Failure Model Validation	97
6.3.1 LCO LIB at 100% SOC heated by P_{in} of higher than 20 W	97
6.3.2 LCO LIB at 75% SOC heated by P_{in} of 20 W	99
6.4 Application of Thermo-Kinetic Battery Failure Model in Cascading Battery Failure	101
6.4.1 Cascading battery failure model construction.....	101
6.4.2 Modeling Results of Cascading Battery Failure	103
Chapter 7: Conclusions	110
Chapter 8: Future Work	114
Reference	115

List of Tables

Table 1. Specifications of tested LIB cells.....	19
Table 2. Open circuit voltage and electrical energy stored in LIB samples at different SOC's....	20
Table 3. Typical coefficients obtained for the energy loss rate expression (Equations (2) and (3)).	36
Table 4. Averaged mass lost during each failure event for each types of tested LIB.	42
Table 5. Timing and temperature of safety venting and thermal runaway observed in the open atmosphere experiments on LCO LIBs ($P_{in}=20$ W).	48
Table 6. Timing and temperature of safety venting and thermal runaway observed in the open atmosphere experiments on NMC LIBs ($P_{in}=20$ W).	48
Table 7. Timing and temperature of safety venting and thermal runaway observed in the open atmosphere experiments on LFP LIBs ($P_{in}=20$ W).	49
Table 8. Summary of the internal heat generation measurements.	54
Table 9. Summary of the cone calorimetry measurements.	62
Table 10. Settings of dynamic LCO LIB density utilized in thermo-kinetic battery failure model.	92
Table 11. Finalized Arrhenius parameter for the thermo-kinetic model of battery failure	95

List of Figures

Figure 1. Detailed Structure of a Cylindrical Battery Cell.	2
Figure 2. Observations of Thermally-Induced Failure of an LIB: Safety Venting (a) and Thermal Runaway (b).....	4
Figure 3. Tested LIB cells with (left) and without (right) plastic packaging.....	18
Figure 4. Schematic of the CSBC apparatus.....	21
Figure 5. Setup of the battery experiments in open atmosphere.....	23
Figure 6. Setup of the battery experiments in cone calorimeter.	26
Figure 7. Setup of the battery experiments in nitrogen atmosphere.	27
Figure 8. Experiment setup for cascading battery failure tests.	28
Figure 9. Cascading battery failure test in nitrogen environment.....	30
Figure 10. An example of data collected in power loss calibration experiments.	33
Figure 11. Energy loss rates computed from the temperature data collected in the power loss calibration experiments.....	34
Figure 12. Power loss corrected for heating rate dependence.....	35
Figure 13. Representative temperature histories for LCO LIBs measured in the CSBC experiments conducted in open atmosphere ($P_{in}=20$ W).....	37
Figure 14. Representative temperature histories for NMC LIBs measured in the CSBC experiments conducted in open atmosphere ($P_{in}=20$ W).....	38
Figure 15. Representative temperature histories for LFP LIBs measured in the CSBC experiments conducted in open atmosphere ($P_{in}=20$ W).....	39
Figure 16. Heat capacity of LCO LIBs calculated from the results of the CSBC experiments conducted in open atmosphere.....	40

Figure 17. Heat capacity of NMC LIBs calculated from the results of the CSBC experiments conducted in open atmosphere.....	41
Figure 18. Heat capacity of LFP LIBs calculated from the results of the CSBC experiments conducted in open atmosphere.....	41
Figure 19. Representative LCO LIBs mass histories ($P_{in}=20$ W) used in the calculation of failure energetics.	43
Figure 20. Representative NMC LIBs mass histories ($P_{in}=20$ W) used in the calculation of failure energetics.	44
Figure 21. Representative LFP mass histories ($P_{in}=20$ W) used in the calculation of failure energetics.	45
Figure 22. Representative slug temperature histories recorded in the CSBC experiments ($P_{in}=20$ W).	47
Figure 23. Internal heat generation by the processes inside LCO LIBs during their thermal failure ($P_{in} = 20$ W).....	50
Figure 24. Internal heat generation by the processes inside NMC LIBs during their thermal failure ($P_{in} = 20$ W).....	51
Figure 25. Internal heat generation by the processes inside LFP LIBs during their thermal failure ($P_{in} = 20$ W).	52
Figure 26. Dependence of the total internal heat produced (left) and average internal heat generation rate (right) on stored electrical energy. The dashed lines are spline interpolations of the displayed experimental data points. The dotted line (in the left graph) is a hypothetical curve for an LIB if it produced heat equal to the stored electrical energy.	55

Figure 27. Relations between the total mass lost and heat produced inside LIBs at 100% SOC. The points are experimental data. The dashed lines are extrapolations of the experimental data to zero mass loss conditions..... 56

Figure 28. Temperature measurements for radial thermal conductivity of LIBs ($P_{in}=20$ W). ... 57

Figure 29. Heat release rate of flaming non-premixed combustion of ejected LCO LIB materials. 59

Figure 30. Heat release rate of flaming non-premixed combustion of ejected NMC LIB materials..... 60

Figure 31. Heat release rate of flaming non-premixed combustion of ejected LFP LIB materials. 61

Figure 32. Dependence of the total heat of flaming combustion (left) and average rate of production of this heat (right) on stored electrical energy. The dashed lines are spline interpolations of the displayed experimental data points..... 62

Figure 33. Experimental observation of intermittent combustion after the onset of thermal runaway of a 100% SOC LIB. 63

Figure 34. Comparison of the results of nitrogen atmosphere and open atmosphere CSBC experiments performed on 100% SOC NMC LIBs ($P_{in}=20$ W)..... 65

Figure 35. Representative slug temperature histories recorded in CSBC experiments with P_{in} ranging from 40 W to 100 W..... 66

Figure 36. Relations between the heating rate P_{in} and the onset time of thermal runaway for tested LIBs at 100% SOC. 67

Figure 37. Representative slug temperature histories recorded in CSBC experiments with LCO LIB's SOC's ranging from 0% to 100%..... 68

Figure 38. Representative cascading battery failure behaviors, 0 mm spacing test in air. (a) – (c) show thermal runaway of the 1st row LIB, (d) – (f) show thermal runaway of the 2nd row LIBs, (g) – (i) show thermal runaway of the 3rd row LIBs. 69

Figure 39. Average onset time of thermal runaway at different rows and the comparisons between different experimental setups in LCO LIB cascading failure tests. 70

Figure 40. A snapshot of simulated temperature distribution in the CSBC apparatus. The geometric dimensions are in mm; the temperature is in K. 73

Figure 41. Temperature dependent natural convection coefficient utilized in COMSOL simulation. 77

Figure 42. COMSOL simulations of power loss calibration tests for determination of thermal conductivity of insulation material. 80

Figure 43. COMSOL simulation results to determine radial thermal conductivity of LIBs. 82

Figure 44. Results of numerical modeling of the CSBC experiments performed for LCO LIB cells. P_{IHG} is prescribed; T_{slug} is simulated and compared with the experimental data. 85

Figure 45. Results of numerical modeling of the CSBC experiments performed for NMC LIB cells. P_{IHG} is prescribed; T_{slug} is simulated and compared with the experimental data. 86

Figure 46. Results of numerical modeling of the CSBC experiments performed for LFP LIB cells. P_{IHG} is prescribed; T_{slug} is simulated and compared with the experimental data. 87

Figure 47. Results of thermo-kinetic model ($n=1$) of the tested LIB cell’s thermal failure observed in CSBC tests ($P_{in}=20$ W), T_{slug} is simulated and compared with the experimental data. 94

Figure 48. Results of thermo-kinetic model ($n \neq 1$) of the tested LIB cell’s thermal failure observed in CSBC tests ($P_{in} = 20$ W), T_{slug} is simulated and compared with the experimental data. 96

Figure 49. Results of thermo-kinetic model of the tested 100% SOC LIB cell’s thermal failure observed in CSBC tests (P_{in} ranging from 40 W to 100 W), T_{slug} is simulated and compared with the experimental data. 98

Figure 50. Relations between the heating rate P_{in} and the onset time of thermal runaway for LCO LIBs at 100% SOC, with comparisons to simulated data. 99

Figure 51. Results of thermo-kinetic model of the tested 75% SOC LIB cell’s thermal failure observed in CSBC tests ($P_{in} = 20$ W), T_{slug} is simulated and compared with the experimental data. 100

Figure 52. Results of simulation of the LIB cascading failure in billiard battery pack with $k_{LIB} = 1.0$ W m⁻¹ K⁻¹, TC#1 to TC#4 measurements from the battery pack is simulated and compared with the experimental data. 104

Figure 53. Results of simulation of the LIB cascading failure in billiard battery pack with $k_{LIB} = 2.6$ W m⁻¹ K⁻¹, TC#1 to TC#4 measurements from the battery pack is simulated and compared with the experimental data. 106

Figure 54. Simulated cascading battery failure behaviors, 0 mm spacing test in nitrogen. (a) – (c) show thermal runaway of the 1st row LIB, (d) – (f) show thermal runaway of the 2nd row LIBs, (g) – (i) show thermal runaway of the 3rd row LIBs. 107

Figure 55. Results of simulation of the LIB cascading failure in billiard battery pack with $k_{LIB} = 2.6$ W m⁻¹ K⁻¹, onset time of thermal runaway for each LIB in the battery pack is simulated with 3 different meshing sizes and compared with the experimental measurements. 108

Nomenclature

Acronyms

Descriptions

LIBs	Lithium Ion Batteries
SOC	State of Charge
LCO	Lithium Cobalt Oxide
NMC	Lithium Nickel Manganese Cobalt Oxide
LFP	Lithium Iron Phosphate
SEI	Solid Electrolyte Interphase
DSC	Differential Scanning Calorimetry
ARC	Accelerating Rate Calorimetry
MCMF	Meso-Carbon Micro-Fiber
CSBC	Copper Slug Battery Calorimetry
CC	Cone Calorimetry
TC	Thermocouple

Symbols

Descriptions

P_{IHG}	Power of Internal Heat Generation by an LIB [W]
P_{in}	Electric power supplied to CSBC to heat up LIB [W]
P_{loss}	Power of thermal energy transfer in CSBC [W]
$P_{Flaming}$	Power of Flaming Combustion Heat Release [W]
c	Heat Capacity [$\text{J g}^{-1} \text{K}^{-1}$]

t	Time [s]
m	Mass [g]
slug	Copper Slug in CSBC
T	Temperature [K]
dummy	Dummy Battery (copper cylinder in 18650 LIB's dimension)
$A_{0,1,4}, b_{0-4}$	P_{loss} Coefficients (Table 3)
σ	Stefan-Boltzmann Constant, 5.67×10^{-8} [W m ⁻² K ⁻⁴]
T_{∞}	Ambient Air Temperature [K]
ε	Emissivity of Radiating Surfaces
q_{rad}	Radiative Heat Loss [W m ⁻²]
q_{conv}	Convective Heat Loss [W m ⁻²]
h	Convection Coefficient [W m ⁻² K]
Nu	Nusselt Number
Ra	Rayleigh Number
g	Standard Gravity, 9.8 [m s ⁻²]
T_f	Film Temperature at Convective Surface [K]
α	Diffusivity of Air [m ² s]
ν	Kinematic Viscosity of Air [m ² s]
k	Thermal Conductivity [W m ⁻¹ K ⁻¹]
L	Characteristic Length of Convective Surface [m]
r	Reaction Rate [g m ⁻³ s ⁻¹]
$\frac{m_r}{V}$	Concentration of Reactant [g m ⁻³]

$A\left(\frac{T}{T_{ref}}\right)^n$	Pre-exponential Factor [s^{-1}]
E_a	Activation Energy [$J\ mol^{-1}$]
R	Ideal Gas Constant, 8.314 [$J\ mol^{-1}\ K^{-1}$]
h_r	Heat of Reaction [$J\ g^{-1}$]
$P_{reaction}$	Power of Energy Release by Chemical Reaction [$W\ m^{-3}$]

Chapter 1: Introduction

1.1 Background and Motivation

Lithium ion batteries (LIBs) are the state-of-the-art energy storage devices that can provide the best combination of high energy density, high efficiency and long cycle life, and exhibit no memory effect [1]. LIBs have been employed in an increasing range of energy demanding applications [2]. Some of these systems only need a single LIB cell (e.g. cell phones.), but more and more systems are in need of multiple LIB cells (e.g. laptops, electric vehicles, etc.). With such a wide variety of LIB applications in people's daily life, fire safety of these devices becomes an important consideration.

LIBs typically consist of four primary components: two electrodes (anode and cathode), electrolyte and separator [2]. In most commercial LIB cells, the anode material is graphite. The most common cathode materials are metal oxides (for example: lithium cobalt oxide or lithium manganese oxide). The electrolyte is typically a mixture of organic carbonates. The separator is a thin (<30 μm) micro-porous polymer layer [3] located between the cathode and anode to prevent internal short circuit while allowing lithium ions to pass through. More specifically, the detailed structure of a cylindrical battery cell is illustrated in Figure 1. Two separator plates sandwich the anode and cathode plate and then they are jelly-rolled to be secured into the steel battery casing. Cathode plate is then connected to the positive terminal on the case while the anode plate is connected to the negative terminal on the battery case.

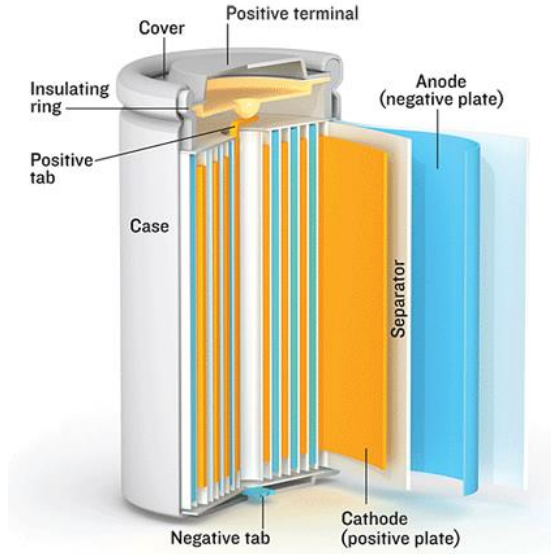


Figure 1. Detailed Structure of a Cylindrical Battery Cell.

When LIBs are subjected to environmental conditions outside their intended designed envelope, such as over charge, short circuit, mechanical or thermal abuse, they may fail irreversibly [4-6]. In particular, thermal abuse may trigger rapid exothermic reactions inside an LIB. More specifically, an LIB subjected to sufficient external heat may initially vent potentially combustible gases and aerosols. This phenomenon is referred to as safety venting [1]; it represents an engineered mechanism that prevents internal pressure build-up and explosive rupture of the cell casing. Subsequently, the LIB may self-heat rapidly. This phenomenon is referred to as thermal runaway [1, 2] because of its self-accelerating nature (e.g., increasing temperature increases the rate of chemical reactions which produce heat and further increase the temperature). The thermal runaway is frequently accompanied by ejection of a portion of electrolyte, separator and electrode materials. These two stages of thermally-induced failure can contribute to hazards associated with a potential fire occurrence. A number of fire and explosion incidents

associated with LIBs have been reported, ranging from ignition of consumer electronic devices to fires in electric vehicles [2].

Figure 2 shows the preliminary observations of thermally-induced failure conducted in our lab at the beginning of current study. A fully-charged (100% SOC) Panasonic CGR18650CG LIB cell (NMC) was secured on a metal mesh and directly exposed to a non-premixed methane flame. When the safety venting (Figure 2a) was triggered, combustible battery products were ejected out from the safety venting ports and caught fire immediately. Three laminar jet flame in the length of around 200 mm were observed. The external heating from the methane flame underneath continued until the thermal runaway (Figure 2b) was initiated. At the very beginning of thermal runaway, a large amount of smoke in white/grey color was released from the battery, then a significant amount of battery material was being vented out at a much higher speed than that observed in safety venting. The three jet flame turned out to be more turbulent followed by bright flame sparkling. The whole process of thermal runaway was over within 6 seconds. In some cases, the core of the battery can be ejected out like a bullet from the casing of the battery cell.



(a)



(b)

Figure 2. Observations of Thermally-Induced Failure of an LIB: Safety Venting (a) and Thermal Runaway (b).

According to Spotnitz and Franklin's summary [7], the general progression of the chain reactions that eventually lead to thermal runaway of an LIB includes: 1). The decomposition of solid-electrolyte interphase (SEI) layer at around 360 K to 390 K. The SEI plays as a protection layer to prevent direct reaction between active anode material and electrolyte solvent. 2). Without SEI's protection mechanism, the intercalated lithium in the anode material will begin to react with electrolyte solvent at temperature of higher than 390 K. 3). The heat produced in the previous two steps can heat the LIB to temperature of more than 440 K, where the cathode active materials can begin to decompose and/or react with the electrolyte solvent. 4). The remaining electrolyte will begin to react with both anode and cathode material at temperature of higher than 470 K, the heat generated in this step can easily elevate the LIB temperature to over 870 K. Thermal runaway will take place starting from step 3, where the increasing temperature

increases the rate of chemical reactions which produce heat and further increase the temperature.

The relative thermal stability of an LIB can vary with factors such as manufacturing method or battery material compositions [8-12]. An in depth understanding of the battery failure behaviors under abnormal conditions can provide insightful information to help improve the LIB safety [13, 14]. Battery safety problems can be addressed by minimizing the probability and severity of battery failure events, or lessening the outcome of battery failure so that such failure can potentially be predicted [15]. In particular, various safety features including safety vents, flame retardant additives, current interrupt device and positive thermal coefficient devices are dedicated towards the former [1, 16, 17]. On the other hand, current study as well as considerable previous research efforts listed below have focused on the latter.

1.2 Previous Experimental Study on Battery Failure

Experimentally, many previous studies were conducted for the measurement of onset temperatures and energetics of the thermally-induced failure of LIBs. Techniques such as differential scanning calorimetry (DSC) [12, 18-25], accelerating rate calorimetry (ARC) [12, 24-31], VSP2 adiabatic calorimetry [22, 32-34], C80 calorimetry [35-37] and oxygen consumption calorimetry [38] were utilized by various researchers to analyze the failure processes.

DSC is a thermoanalytical technique that measures the heat flow associated with physical and chemical transitions in a milligram-sized sample. The sample temperature is increased linearly with time at rates that are sufficiently low (typically, 3-30 K min⁻¹) to maintain spatial uniformity of temperature within the sample. DSC was used to study a

number of electrode and electrolyte materials as well as their combinations. Yang et al. [18] investigated graphite, the most common anode material, at various states of charge (SOC). Sharp exothermic peaks were detected at around 600 K in the samples containing more than 0.7 lithium ions per 6 carbons, and were attributed to the structural collapse of the graphitic matrix. Roth et al. [23] examined thermally-induced interactions between several binder materials (used to ensure adhesion between electrode and current collector), representative anode materials at different SOC and electrolyte. It was found that the amount of electrolyte, the surface area of the anode and its SOC have a strong impact on the exothermicity of the observed reactions. Maleki et al. [25] employed DSC to examine the thermal stability of the anode and cathode for a specific LIB chemistry, graphite/LiCoO₂. The total heats of decomposition were measured to be 697 and 407 J g⁻¹, for the anode and cathode, respectively (here, exo is positive). These heats decreased by about 60% with the removal of electrolyte. In the work reported in [21], DSC was utilized to examine a polymer-bonded lithiated carbon anode. It was found that the first reaction taking place at 390-410 K and both the specific surface area of the electrode and the degree of lithiation had strong impact on the reactions. In another experimental work [12], the MesoCarbon MicroBeads graphite was investigated by DSC and it was found to have increased thermal stability of the cell due to more effective solid electrolyte interface (SEI) formation.

ARC [39] measures temperature and pressure change in a sealed stainless steel or titanium container that accommodates a relatively large (about 100 cm³ in volume) sample of interest. The container is heated slowly (about 0.2 K min⁻¹). When an exothermic process inside the container is detected, the instrument increases container

housing temperature to minimize the heat transfer from/to the container. Von Sacken and co-authors [27] utilized ARC to study and compare the thermal stability of battery cells containing different anode materials. They showed that the carbon intercalation anode was superior to a lithium metal anode. Maleki et al. [25] applied this technique to measure the onset temperature of chemical reactions that force the cell into thermal runaway. This temperature was found to be close to the decomposition temperature of the unwashed cathode material. In another study by Maleki et al [26], ARC was utilized again to investigate two types of cells with different electrode chemistries. The thermal stability of the cell consisting of Sn-LiCoO₂ cathode and meso-carbon micro-fiber (MCMF) anode was found better than the cell consisting of LiCoO₂ cathode and graphite anode. In another work by Al Hallaj et al. [40], commercial lithium-ion cells at different open circuit potentials were tested inside an ARC to determine the onset-of-thermal-runaway (OTR) temperatures. Sony (US18650) cells at 4.06, 3.0, and 2.8 V open circuit voltage OCV were tested and their measured OTR temperatures were found to be 377, 382, and 417 K, respectively.

In another recent work conducted by Lyon and Walters [41, 42] at Federal Aviation Administration, battery failure of 4 different commercial cathode chemistries in the form factor of 18650 was studied by utilizing bomb calorimeter. The battery thermal failure was induced by electrical resistance heating in the nitrogen-filled bomb calorimeter to preclude combustion of the battery materials. The total energy by the battery failure, which were assumed to consist of both electric energy stored in the battery and the chemical energy produced by complex chemical reactions in between the battery materials, were carefully determined. This study indicated that: 1). The severity of

a battery failure is proportional to the electric energy stored in a battery; 2). The electric energy stored in a battery and the chemical energy produced by battery material chemical reactions have comparable contributions to energy produced in a battery failure. This important study also measured the total battery failure energy by T-Energy ICR18650 batteries (lithium cobalt oxide) at various states of charge, which provides a valuable reference data for the same LIB type measured and reported in this dissertation.

While DSC, ARC, bomb calorimeter and other aforementioned calorimetry techniques proved to be very useful in analysis of LIB failure, they possess notable limitations. For example, DSC can only be applied to the analysis of battery components. ARC has not been specifically designed for LIB failure experiments, where chemical processes inside and outside the battery casing may contribute to the energy generation and the rates of temperature rise may exceed 500 K min^{-1} . A quantitative interpretation of the ARC data on LIB failure can be difficult.

1.3 Previous Modeling Study on Battery Failure

Besides experimental studies, a lot of other previous research has been dedicated to the development of thermal model for LIB failure. Doughty et al [13] proposed two general approaches to build such models: 1). The calorimetry-based approach and 2). Chemical reaction approach. The former approach is based on a simplified model of battery construction and it requires the characterization of thermal properties of battery components including chemical reaction rates, battery material decomposition reactions, cycle/aging history, SOC of battery, heat capacity and thermal conductivity of battery components. The latter approach, on the other hand, requires the identifications of the chemical reactions associated with each of the dominant thermal related events. These

chemical reactions must be combined with details of the cell construction in order to simulate the behavior of overall battery cell.

More specifically, in Al Hallaj et al.'s report [40], a simplified one-dimensional thermal model was presented with lumped parameters to simulate the temperature profiles inside lithium ion cells during discharge. The simulation results showed good agreement with temperature measurements at discharge rate of $C/2$, $C/3$, and $C/6$ discharge rates, but some deviation was noticed for the $C/1$ discharge rate ($C/2$ discharge rates allows a battery to be fully discharged in 2 hrs, $C/3$ discharge rates allows a battery to be fully discharged in 3 hrs, etc. Depending on the capacity of a battery, the discharging current can be different.). The model was used to simulate temperature profiles under different operating conditions and cooling rates for scaled-up cylindrical lithium-ion cells of 10 and 100 A h capacity. Results showed a strong effect of the cooling rate on cell temperature for all discharge rates. In Pals and Newman's work [43, 44], two one-dimensional models were presented to predict the thermal behavior of the lithium/polymer battery: one for one-cell and the other one for a cell stack. The models were used to simulate a wide range of polymeric separator materials, lithium salts, and composite insertion electrodes. Christophe Forgez et al [45] developed a lumped-parameter thermal model of a cylindrical LiFePO_4 /graphite lithium-ion battery. In this model, the inputs of heat transfer coefficients and heat capacity were obtained experimentally. And the model allowed for simulating the internal temperature directly from the measured current and voltage of the battery. These one-dimensional models were only utilized during early stage of battery model development, more recent efforts have been moving to higher dimensional models.

Some two-dimensional models were proposed to predict the temperature distribution of LIBs under various state of charge, discharge and statics situation. Predicting temperature distribution in radius and azimuthal coordinates for the cylindrical cell, in width and length directions for the prismatic battery. For example, Chen, Wang and Wan [46] proposed a two-dimensional thermal model to establish a standard methodology for the simulation of spirally wound cells (cylindrical cells). Through this modeling work, it was found that under natural convection, the hottest temperatures were in a circular region near the liquid-filled hollow core but not at the exact center. The temperature at the angular direction (on the surfaces with the same radius from the cell's axis) was found to be fairly uniform and heat was mainly transferred along the radial direction. Radiation was found to contribute as much as 53.6% of the heat dissipation from the simulated battery to ambient air. In another work by Chen et al. [47], a detailed three-dimensional thermal model was developed to examine the thermal behavior of a lithium-ion battery. Location-dependent convection as well as radiation were adopted at boundaries to reflect different heat dissipation performances on different surfaces. These models successfully described the asymmetric temperature distribution inside a battery, as well as the anomaly of temperature distribution on the surface. It was found that radiation could contribute to 43–63% of the overall heat dissipation from the battery to ambient air.

Moreover, Chen and Evans [48, 49] developed three dimensional models to study the thermal behavior of lithium ion batteries. In particular, a thermal analysis of lithium-ion batteries during charge/discharge and thermal runaway was carried out by utilizing this model. The major assumption was that the heat generation rate is uniform throughout

the cell. Their model required precise construction of the cell structure. Continuous cycling under high-rate charge and discharge could cause significant amount of heat accumulation within a battery. The analysis of heat transport in the existence of highly localized heat sources due to battery abuse (e.g., short circuit) indicates that localized heating may raise battery temperature, within one minute, to the onset temperature of thermal runaway. This model precisely considered the layered-structure of the cell stacks, the case of a battery pack, and the gap between both elements to achieve a comprehensive analysis.

Kim et al. [50] extended the one-dimensional modelling approach formulated by Hatchard et.al [51] to three dimensional, utilizing finite volume method, to further understand the thermal abuse behavior of large format Li-ion batteries. Chemical reactions at elevated temperatures in Li-ion batteries were listed and formulated to be included in this model. This three-dimensional model can capture the shapes and dimensions of cell components and the spatial distributions of materials and temperatures, and it was used to simulate oven tests as well as to determine how a local hot spot can propagate through the cell. The model results showed that smaller cells dissipated heat faster than larger cells, which may prevent them from going into thermal runaway under identical abuse conditions. In simulations of local hot spots inside a large cylindrical cell, the three-dimensional model predicted that the reactions initially propagate in the azimuthal and longitudinal directions to form a hollow cylinder-shaped reaction zone. Guo et al. [52] developed a three-dimensional thermal model for analyzing the temperature distribution under abuse conditions. This model applied finite element method and it coupled electrochemical reaction and detailed temperature distribution

inside a battery cell. The effects of heat generation, internal conduction and convection, and external heat dissipation were taken into account. The heat generation included the chemical reactions; the heat effects of ohmic resistance and polarization; and the heat generated by “side reactions”. Examples of the side reactions were corrosion reaction, overcharge, and chemical shorts. The model predicted that the battery sample would undergo thermal runaway at 60 min in 428 K oven test, which agreed well with Kim’s results [50].

Santhanagopalan et al. [53, 54] developed an electrochemical thermal model to study the internal short-circuit behavior of a lithium ion cell. Several short-circuit scenarios possible in a lithium ion cell were simulated and the influence of parameters like the SOC and initial temperature of the cell was studied. The results were verified by the experimental results. Zhang [55] developed another electrochemical-thermal model with full consideration of electrolyte transport properties as functions of temperature and Li ion concentration. A conservative finite volume numerical method is employed for the spatial discretization of the model equations. Three types of heat generation sources including 1) the ohmic heat, 2) the active polarization heat and 3) the reaction heat are quantitatively analyzed for the battery discharge process. The ohmic heat was found to be the largest contribution with around 54% in the total heat generation. About 30% of the total heat generation on average was ascribed to the electrochemical reaction. The active polarization contributed the least comparing to the ohmic heat and reactions heat. The raised temperature in the battery discharge is positive related with the thickness of both separator and electrodes. In Jeon and Baek’s work [56], a simplified thermo-electric finite element analysis (FEA) model was developed to study the thermal behavior of Li-ion

battery during discharge cycle. The mathematical model can solve conservation of energy considering heat generations due to both joule heating and entropy change. It was found that the contribution of heat source due to joule heating was significant at a high discharge rate, whereas that due to entropy change was dominant at a low discharge rate. Fang et al. [57] developed another electrochemical-thermal coupled model to predict performance of a lithium-ion cell as well as its individual electrodes at various operating temperatures. The predictive ability of the individual electrode behavior was very useful to address important issues related to electrode degradation and subzero performance of automotive lithium ion batteries.

In addition, in Guo et al.'s study [58], the single-particle model presented by Santhanagopalan et al. [59] was extended to include an energy balance. The model took into consideration critical factors such as: the temperature dependence of the solid phase diffusion coefficient of the lithium in the intercalation particles, the electrochemical reaction rate constants and the open circuit potentials (OCPs) of the positive and negative electrodes. In Cai and White's work [60, 61], the existing lithium ion battery model in COMSOL was extended to study the thermal behavior of a lithium ion battery during the discharge process with and without a pulse. The proper orthogonal decomposition method was applied to develop an efficient, reduced order electrochemical-thermal model for a lithium-ion cell. The model can achieve 7 times more efficiency than the COMSOL model. The model predictions indicate that the discharge efficiency depends on the rate of the discharge and heat transfer rate away from the cell. Spotnitz et al. [62] proposed a simple approach for using accelerating rate calorimetry (ARC) data to simulate the thermal abuse resistance of battery packs. It was found that a small increase

in the heat released by the exothermic reaction of a single cell can cause the pack to go into thermal runaway. This phenomena indicated that thermal runaway of the pack is more likely to be induced by thermal runaway of a single cell when that cell is in good contact with other cells and is close to the pack wall. Lopez et al's work [63] aimed to characterize the effect of thermal runaway reactions by utilizing a thermal abuse model of cells subjected to elevated temperature. This model was derived from conventional oven test, where it was found that the probability and severity of thermal runaway increased with increased oven temperature and decreased convection coefficient for conventional oven tests. The abuse reaction sequence was found to be: first SEI decomposition, second negative-solvent, and lastly positive-solvent. The model was validated against experimental results. It was found that an electrolyte combustion reaction must be accounted for in the model if the electrolyte ignite during the test. The simulated thermal behavior under constant-power heating condition was found to be in agreement with experiments.

While these aforementioned model showed powerful capabilities of predicting thermal behaviors of lithium ion batteries, they possess notable limitations. For example, most of these model required detailed construction of battery structure and their accuracy relied largely on the determination of thermal properties of battery components. Extra work were required to determine the chemical reaction rates associated with failure event as well as the battery materials' decompositions. A lot of attentions were focused on battery failure caused by charging/discharging and/or internal short circuit, but study on the model for another important form of battery failure – thermally-induced failure – was limited. Last but not least, although a lot of work were focused on understanding failure

of single LIB cell, the potential hazards caused by cascading battery failure in multiple LIB cell systems (in large format of LIB application or during LIB transportations) was not sufficiently studied.

1.4 Scope of Current Study

Current study is focused on developing a framework consisting of both comprehensive experimental investigations [64] and modeling of the thermally-induced failure of LIBs. In particular, we have proposed a systematic experimental technique and methodology specifically to evaluate energetics of the thermally-induced failure of LIBs. This technique, which we refer to as Copper Slug Battery Calorimetry (CSBC), is the major experimental apparatus developed in this study. It measures the heat capacity of an LIB cell and the amount of energy released inside a casing of an LIB cell as it undergoes the failure process. The apparatus that was employed in this study was specific to the 18650 form factor of LIB cells (cylinders 18 mm in diameter and 65 mm in height). However, the technique can be readily adapted to a range of cell shapes and sizes. We also demonstrate how the CSBC can be combined with cone calorimetry [65] to enable measurement of the energy released as a result of a flaming combustion of the battery materials ejected from the cell. Comprehensive characterizations of three LIB chemistries, LCO (T-Energy ICR18650), NMC (Panasonic CGR18650CG) and LFP (K2 18650E), were carried out to demonstrate the capabilities of this technique. The dependence of failure energetics on the battery's SOC as well as battery sample's cathode components was analyzed and discussed.

As an extension of the experimental work, efforts have been taken toward the development of a new thermo-kinetic model to predict the thermally-induced failure of

LIBs. COMSOL Multiphysics [66] was selected in current study to be the numerical simulation software platform. COMSOL includes different physics-specified modules (e.g. heat transfer module, chemical reaction engineering module etc.) that can work individually or integrally. The COMSOL heat transfer module can perform detailed computations associated with the conservation of energy and mass while the COMSOL chemical reaction engineering module can perform precise computations to solve for heat release rate by chemical kinetics based on Arrhenius Law. More specifically, the first stage development of battery failure model only utilized the COMSOL heat transfer module. This model took into account the detailed transient thermal transport dynamics to simulate the standard CSBC experiments thus it was adopted to validate the experimental measurements. This validation exercise showed that the assumptions made for CSBC experimental analysis were reasonable, demonstrating that the CSBC technique had promising accuracy in terms of characterizing the battery failure. The second stage development of the battery failure model – thermo-kinetic model – utilized both COMSOL heat transfer module and chemical engineering module. The development of this model is specifically demonstrated on LCO (T-Energy ICR18650) LIB cells. The CSBC experimental data collected and reported previously were used in an iterative inverse modeling analysis to determine the key model parameters, and it was found that one chemical reaction was sufficient enough to effectively describe the battery failure of the LIB sample at each tested state of charge (SOC). The model didn't require inputs describing battery structure or detailed battery component properties. The fully-parameterized model was then validated against additional experiments conducted in CSBC: non-standard CSBC experiments on single battery cell which data was not

utilized in the model development process. Validations were provided through a comparison against the temperature measurements collected in these non-standard CSBC tests.

Finally, an important but not sufficiently studied yet type of battery failure – cascading battery failure was examined in this dissertation. Cascading battery failure tests were conducted where multiple LIB cells were assembled in a billiard pack to examine the cascading thermally-induced failure of LIBs. The developed and validated thermo-kinetic battery failure model was then utilized to simulate the onset time of thermal runaway for each LIB cell in this cascading failure test configuration. Experimental data and simulated data were compared to evaluate the extrapolation capability of this battery failure thermo-kinetic model.

This dissertation is focused on reporting: 1). The detailed descriptions of CSBC technique and all types of experiments conducted (Chapter 2); 2). The analysis procedure of CSBC technique and experimental results (Chapter 3 and Chapter 4); 3). Numerical modeling for the validation of CSBC experimental measurements (Chapter 5); 4). Thermo-kinetic model of thermally-induced failure of LIBs and its application in simulating cascading battery failure (Chapter 6). 5). Concluding remarks (Chapter 7); and 6). Future work as an extension of current study (Chapter 8).

Chapter 2: Experimental Methods

2.1 Battery Samples

One of the most commonly used form factor of LIB cells, 18650, were selected in this study. LIBs in this form factor are in the shape of cylinders with 18 mm in diameter and 65 mm in height. The three types of LIB cells analyzed in this study are: T-Energy ICR18650, Panasonic CGR18650CG and K2 18650E. These samples are shown in Figure 3 and their detailed specifications are given in Table 1. The main differences between these samples is the chemical structure of the cathode material, and because of this major difference, T-Energy ICR18650 cells are referred to as “LCO” LIB cells, Panasonic CGR18650CG cells are referred to as “NMC” LIB cells and K2 18650E cells are referred to as “LFP” LIB cells.



Figure 3. Tested LIB cells with (left) and without (right) plastic packaging.

Table 1. Specifications of tested LIB cells.

LIB Type	LCO	NMC	LFP
LIB Model	T-Energy ICR18650 [67]	Panasonic CGR18650CG [68]	K2 18650E [69]
Cathode	lithium cobalt oxide	lithium nickel manganese cobalt oxide	lithium iron phosphate
Anode	carbon	carbon	Carbon
Nominal Capacity (mA h)	2600	2250	1500
Nominal Voltage (V)	3.7	3.6	3.2
No. of Safety Vent Ports	4	3	5
Mass without packaging (g)	44.00±0.07	42.30±0.04	38.60±0.11

Prior to each experiment, the cell's plastic packaging was stripped off and it was charged to a specific SOC with an iCharger 208B using the constant current/constant voltage method. More specifically, each battery was first fully discharged to a minimum voltage of 2.5 V using a constant current of 1.0 A. Subsequently, the battery was charged to 4.2 V using the constant current (1.0 A)/constant voltage method until the charge current fell below 0.1 A. The capacity of each cell was measured during this charging process and was found to be within 3% of the nominal capacity for all the tested LIB cells. Finally, the battery was discharged using a constant current of 1.0 A until the desired SOC was reached, as calculated by current integration.

The investigated SOCs were 0, 25, 50 and 100%. The open circuit voltages of the cells and the electrical energy stored in them, which was directly measured by the charger, are listed in Table 2. Due to the differences in the cathode chemistry and cell design choices, different cell types had significantly different electric capacities. Therefore, to provide adequate comparisons, the key quantities describing the failure

process are presented in this manuscript as a function of the stored electrical energy (kJ), rather than SOC.

Table 2. Open circuit voltage and electrical energy stored in LIB samples at different SOCs.

SOC	LCO		MNC		LFP	
	Cell Voltage (V)	Electric Energy (kJ/W h)	Cell Voltage (V)	Electric Energy (kJ/W h)	Cell Voltage (V)	Electric Energy (kJ/W h)
0%	3.2	0/0	3.0	0/0	3.2	0/0
25%	3.7	7.6/2.1	3.6	6.1/1.7	3.2	4.0/1.1
50%	3.7	15.5/4.3	3.7	13.0/3.6	3.3	7.9/2.2
100%	4.2	32.8/9.1	4.2	27.0/7.5	3.5	15.8/4.4

It should be noted that, while the main difference between the cells was the cathode chemistry, other differences in structure and composition were likely to be present but unavailable due to the commercial nature of the tested specimens. These difference may also have contributed to the observed differences in the cell's thermal performance and failure dynamics.

2.2 Copper Slug Battery Calorimetry

A new experimental technique, Copper slug battery calorimetry (CSBC), was developed in this study to enable time resolved monitoring of the energy release during the thermally-induced failure of an 18650 LIB cell. The thermally-induced failure of the tested LIB was initiated through controlled heating. A schematic of the copper slug battery calorimetry (CSBC) is shown in Figure 4. The primary component of this apparatus is a hollow cylinder composed of 166 g of pure (99.5%) copper (26 mm in outer diameter and 65 mm in height). This cylinder (or slug) has a wall thickness of 4 mm. It houses a battery specimen and is equipped with an embedded, stainless-steel-sheathed, type K thermocouple (at the center thickness of this cylinder's wall and to the

depth of 20 mm), which temperature is recorded at a frequency of 1 Hz by a computer. An LIB is inserted into the cylinder in such a way that its top surface is level with the cylinder's edge and its safety vent ports are open to the atmosphere. The internal dimensions of the cylinder are selected to ensure a tight fit and a good thermal contact with the inserted battery.

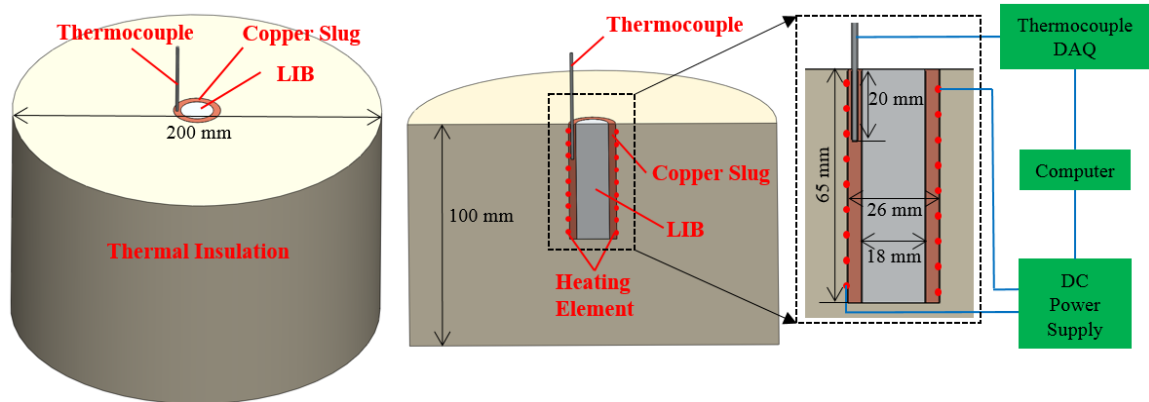


Figure 4. Schematic of the CSBC apparatus.

The controlled heat is delivered by supplying DC power to a resistive heating wire (OMEGA NI80-010-200) electrically insulated with 3M Ruban Isolant tape and tightly wrapped around the cylinder. A BK Precision 1685B power supply is used to provide constant, well-defined electrical power, with settings controlled by a computer. Gemcolite FG23-112HD ceramic fiber insulation material is machined to a cylindrical shape (200 mm in diameter and 100 mm in height), with a cylindrical opening (26 mm in diameter and 65 mm in depth) from the insulation's top surface at the cylinder's axis. The insulation houses the heated slug tightly in the center of insulation with good thermal contact. This design is to minimize heat losses from the system to the environment.

2.3 Power Loss Calibration

An analysis of the processes inside an LIB using the CSBC apparatus requires that the rate with which thermal energy is transferred from the copper slug and battery specimen to the insulation and ambient air (here referred to as power loss) is accurately quantified. This quantification is based on calibration experiments in which a battery is replaced with a solid copper cylinder of the LIB dimensions (the dummy battery). This dummy battery, which weighed 147 g, was heated up to 800 K using constant electric power inputs ranging from 20 to 100 W in 20 W increments. The temperature of the slug and dummy battery were recorded as a function of time at 1 Hz.

To measure the dummy battery's temperature, it was also equipped with a stainless-steel-sheathed, type K thermocouple, which was positioned at the cylinder's axis. The slug and dummy battery temperature histories, combined with the well-known thermal properties of copper, were used to determine an empirical expression for power loss as function of the temperature of the slug. The analysis of power loss calibrations experiments to obtain this expression is described in Chapter 3. The calibration experiments have been conducted regularly in current study, to make sure that any potential impact of apparatus changes associated with multiple heating/cooling cycles on the heat loss is taken into account.

2.4 CSBC Tests to Measure Internal Heat Generation

The tests of LIBs were first conducted in a stand-alone version of the CSBC apparatus. This apparatus was placed under an exhaust hood as shown in Figure 5 to remove volatiles and aerosols generated during the failure process. The LIBs were heated with a constant power of 20 W, supplied continuously for the duration of the experiment.

In addition to the slug temperature, which was recorded as a function of time, the time of the onset of safety venting, onset of thermal runaway and thermal runaway termination were also carefully recorded.

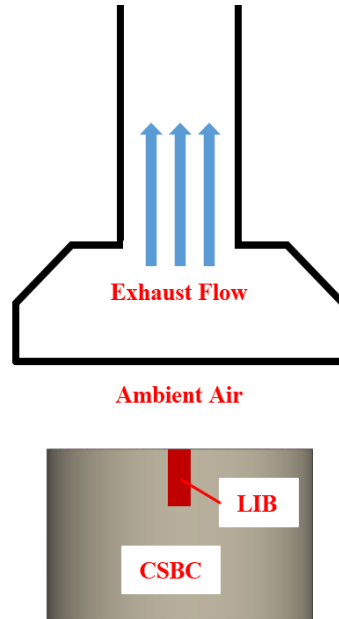


Figure 5. Setup of the battery experiments in open atmosphere.

The onset of safety venting was defined by a clearly audible sound, immediately followed by an appearance of aerosol jets emanating from the safety vent ports. The onset of thermal runaway was detected by observing a sharp increase in the rate of the slug temperature rise, which was accompanied by a sudden boost in the intensity of the jets. The end of thermal runaway was assumed to correspond to the point in time when all venting ceased and the slug temperature approached a plateau. The experiment was stopped 200 s after this point.

For each battery type, 10 open atmosphere tests were conducted for each studied SOC to accumulate statistics (40 tests in total). Each LIB specimen was weighed before and after each test to determine the total mass lost. In addition, 3 open atmosphere tests were performed for each battery type at each SOC where the electric heating was stopped

immediately prior the onset of thermal runaway. These tests were carried out to determine the amount of mass that the LIBs lost during the safety venting phase only. Finally, 3 open atmosphere tests were performed for each battery type at each SOC on the LIB specimens that already underwent thermal runaway to determine potential changes in the battery's heat capacity. This information was required to compute the energetics of the failure process as presented in Chapter 3 and Chapter 4.

2.5 CSBC Tests to Measure Radial Thermal Conductivity of LIBs

In these experiments, the temperature at the slug and that at the battery's axis were measured simultaneously when the tested LIB cell was heated up using a constant electric power input of 20 W. This measurement showed a temperature gradient in the battery's radius direction, which can be utilized in numerical modeling to quantify the LIB's radial thermal conductivity.

More specifically, an opening in the diameter of 1.6 mm was machined at the center of the battery's negative end. This opening revealed a channel structure in the diameter of about 1.6 mm located at the axis inside the battery. A stainless-steel-sheathed, type K thermocouple was inserted into this channel to the depth of 20 mm from the battery's negative end. The measured temperature profiles at both locations were then simulated by numerical modeling utilizing COMSOL heat transfer module. With the knowledge of all material's thermal properties (except for the radial thermal conductivity of battery) and that of thermal boundary conditions defined in the model, the value of radial thermal conductivity of battery was being modified to the point where the simulated temperatures and the experimental measurements of the temperatures reach

excellent agreements. The analysis and result of battery's thermal conductivity are reported in Chapter 5.

For safety concerns, this practice was only conducted for LIB cells at 0% SOC (fully-discharged). The heating was stopped when the temperature at LIB's axis reached 400 K, where no significant thermally-induced failure was initiated yet. It was assumed that the radial thermal conductivity of battery was independent of the batteries' SOC, and it was not impacted by the battery failure events.

2.6 CSBC Tests to Measure External Flaming Heat

In this set of experiments, the CSBC apparatus was mounted under the hood of a standard cone calorimeter [65], a Govmark CC-1, as illustrated in Figure 6. The cone heater was removed from the calorimeter. The cone calorimeter's spark igniter was replaced by a hot wire igniter, which consisted of a coiled OMEGA NI80-010-200 resistance heating wire formed into a 22 mm diameter loop. This loop was suspended 5 mm above the top of an LIB specimen inserted into the CSBC apparatus. The igniter was powered by 56 W of AC electrical power, which produced a bright red glowing wire. The standard cone calorimeter igniter was not utilized in these experiments because it was found to be too small to provide simultaneous ignition of species ejected from all three battery safety vent ports. The LIBs were heated with a constant power of 20 W (the same power as was utilized in the open atmosphere CSBC experiments), supplied continuously for the duration of the experiment to initiate the battery failure. The combustible battery products coming out of the safety vent ports were ignited and the flaming combustion were held by the hot wire igniter.

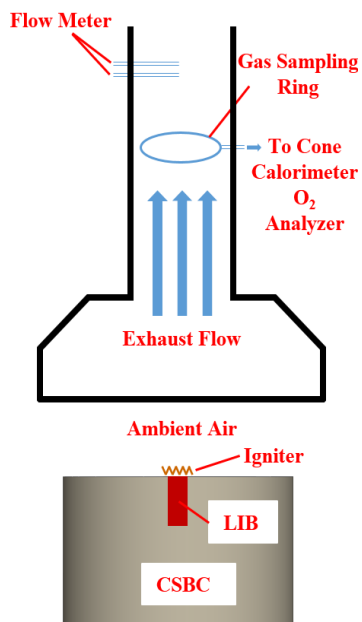


Figure 6. Setup of the battery experiments in cone calorimeter.

The rate of energy release associated with flaming combustion of the species ejected from the LIB during its failure was measured as a function of time by quantifying the rate of consumption of oxygen in this well ventilated, non-premixed combustion process and relating this consumption to the energy release through an empirical constant as defined by the standard [65]. Standard oxygen consumption calibration procedures were followed. 5 cone calorimeter experiments were conducted for each battery type at each SOC to accumulate statistics.

2.7 CSBC Tests in Nitrogen Atmosphere

In this set of experiments, the CSBC apparatus was placed inside of a 53 cm tall and 25 cm diameter air-tight stainless steel chamber as shown in Figure 7. This chamber was purged with high purity nitrogen at a rate of 3 L min⁻¹. 5 experiments were conducted in this chamber using the NMC LIB cells (Panasonic CGR18650CG) at 100% SOC, which were subjected to the same heating conditions (20 W) as those realized in the

open atmosphere experiments. The slug temperature and oxygen concentration in the chamber were recorded. The latter parameter was measured by directing a fraction of the chamber exhaust stream through the cone calorimeter's oxygen analyzer.

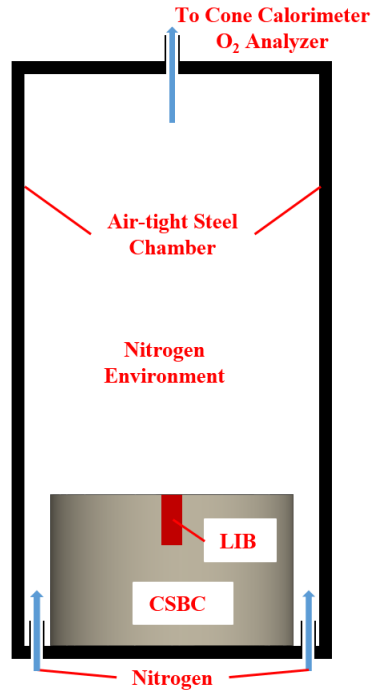


Figure 7. Setup of the battery experiments in nitrogen atmosphere.

These tests were conducted to verify that the heat feedback from the flame, which was observed during the thermal runaway phase of 100% SOC open atmosphere experiments (due to auto ignition of ejected battery materials), was negligible and did not impact the slug temperature readings. Performing these experiments in nitrogen ensured that all flaming combustion was suppressed. The oxygen monitoring was carried out to ensure that the chamber was completely purged of oxygen at the beginning of the experiment, and that no significant amount of oxygen was produced during the battery failure process. It should be noted that a significant oxygen production by the LIBs would make the cone calorimetry measurements described in the Chapter 2.6 unreliable. These tests were only conducted for NMC LIB cells.

2.8 CSBC Tests for Battery Failure Model Validation

This set of experiments were conducted for the purpose of validating the accuracy of the constructed battery failure model, and it included the following non-standard CSBC tests: tests where LCO LIB cells at 100% SOC were heated by heating power ranging from 40 W to 100 W in the segment of 20 W (3 tests were conducted for each heating power); and tests where the LCO LIB cells were charged to 75% SOC and heated by 20 W. The copper slug temperature measurements in all of these tests, recorded as a function of time, were compared to the model data to validate the accuracy of the fully parameterized thermo-kinetic battery failure model. The detailed validation procedure is described in Chapter 5.

2.9 Cascading Battery Failure Tests

In addition to CSBC tests on single cell, experiments were also designed in this study to examine the cascading failure behavior of LIBs at 100% SOC. The experimental setup is illustrated in Figure 8.

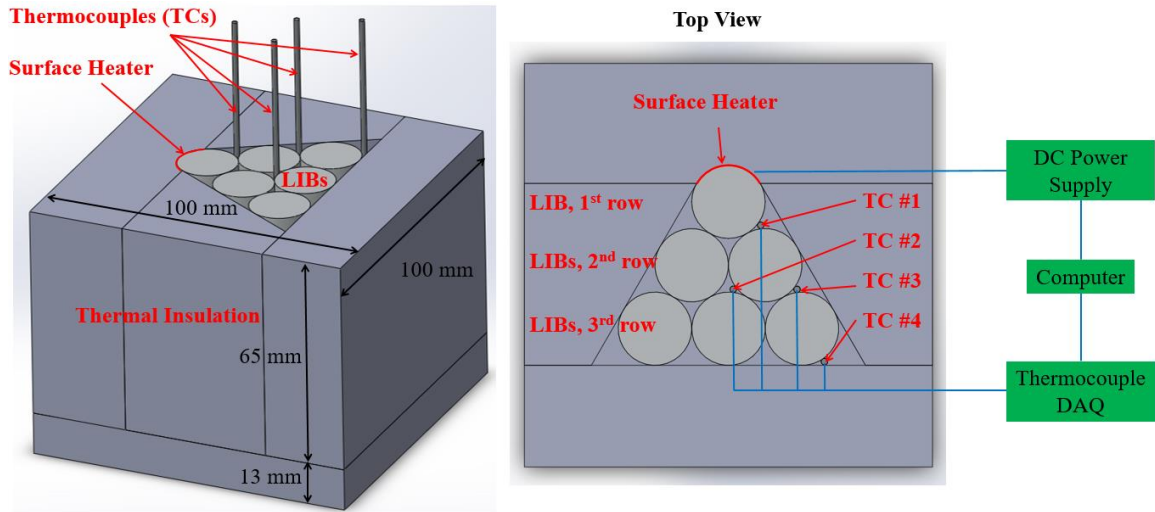


Figure 8. Experiment setup for cascading battery failure tests.

6 LIB cells were fully charged and closely attached in a billiard configuration. These 6 LIB cells were housed in thermal insulation materials made by Kaowool PM [70-73], which was used to minimize heat losses from the system to the environment. A surface heater (65 mm in length and in the width that equals to 1/3 of the perimeter of the LIB cell) was made by a resistive heating wire (OMEGA NI80-010-200) coiled and insulated with 3M Ruban Isolant tape. The surface heater was then wrapped on 1/3 of the side wall of the first LIB cell (away from the propagation direction) and tightly sandwiched in between the LIB at the 1st row and the insulation material. This heater was powered by a DC power supply (BK Precision 1685B) to initiate the cascading thermally-induced LIB failure. This external heat was set at 40 W and was continuously supplied throughout each test. The temperatures of the system were being monitored at 4 different critical locations by type K thermocouples (TCs) as indicated in Figure 8: the interface between the 1st and 2nd rows of LIBs (TC#1); the interface between the 2nd and 3rd rows of LIBs (TC#2 and TC#3), and the interface between the 3rd row of LIBs and the insulation material (TC#4). The height of the measuring points were at half of the LIB's height. A data acquisition module (DAQ) was utilized to measure the temperature at a frequency of 1 Hz and record the data as a function of time. An HD video was taken for each experiment.

10 experiments were conducted in ambient air where the spacing in between all the LIBs was 0 mm (0 mm spacing test in air); 10 experiments were conducted in ambient air where the spacing in between all the LIBs were increased to 3 mm (3 mm spacing test in air); and the last 10 experiments were conducted in nitrogen environment

with 0 mm spacing (0 mm spacing test in nitrogen) to eliminate the heat feedback from the flaming to LIB cells during the cascading failure (Figure 9).

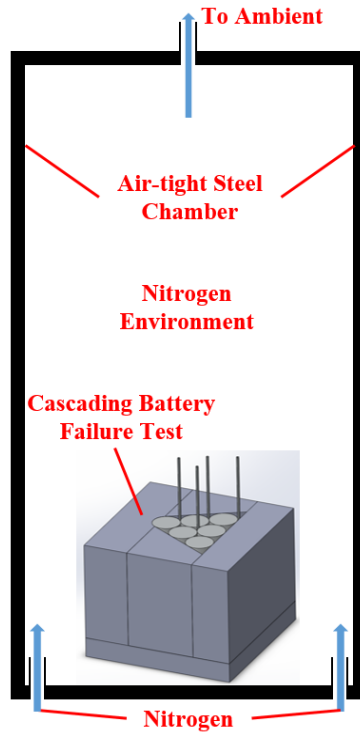


Figure 9. Cascading battery failure test in nitrogen environment.

Each test was stopped when all of the 6 LIBs in the pack went through thermal runaway. After the experiments, the time to thermal runaway of each row of LIBs were determined by analyzing the HD videos. The onset of thermal runaway was detected by observing a sudden boost of venting of battery materials from the venting ports, which is the same criteria as adopted in CSBC tests on single LIB cell.

These test results will be analyzed and presented in Chapter 4. Moreover, the thermo-kinetic model of an LIB's thermal failure, once developed and validated, will be utilized to predict the time to thermal runaway in this cascading battery failure test. The extrapolation capability of the thermo-kinetic battery failure model can be evaluated in

such way by comparing the simulated results and the experimental observations. This exercise is reported in Chapter 6.

Chapter 3: Experimental Data Analysis

3.1 CSBC Governing Equation

The major assumption invoked in the analysis of the CSBC experiments was that the temperature inside the battery was spatially uniform and equal to the temperature at the copper slug, T_{slug} . The Biot number [74] estimated for this experiment by approximating an LIB as an aluminum cylinder is approximately 0.002, which supports this assumption. Provided that this assumption is valid, the CSBC apparatus' energy conservation statement can be formulated as follows:

$$P_{in} + P_{IHG} = c_{slug} m_{slug} \frac{dT_{slug}}{dt} + c_{LIB} m_{LIB} \frac{dT_{slug}}{dt} + P_{loss} \quad (1)$$

The left hand side of Equation (1) contains energy production terms. P_{in} is the electric power supplied to CSBC to heat up the tested LIB (this power is kept constant for the duration of the experiment). P_{IHG} is the power of internal heat generation by an LIB during its thermal failure processes, which is the sought after quantity and is a function of time, t .

The right hand side of Equation (1) contains energy sink terms. The first term is the sensible heat of the slug expressed in terms of its heat capacity (c_{slug}) and mass (m_{slug}). The heat capacity of the slug is equal to that of copper and can be defined by the following function of temperature:

$$c_{slug} = 2.79 \times 10^{-1} + 4.42 \times 10^{-4} T_{slug} - 4.92 \times 10^{-7} T_{slug}^2 + 2.20 \times 10^{-10} T_{slug}^3 + 1.08 \times 10^3 T_{slug}^{-2} \quad (\text{J g}^{-1} \text{K}^{-1}) \quad [75].$$

The mass of the slug can be directly measured. The second term is the sensible heat

associated with an LIB expressed in terms of the battery's heat capacity (c_{LIB}) and mass (m_{LIB}). The last term, P_{loss} , represents the rate of thermal energy transfer from the slug and battery specimen to the insulation and ambient air. In particular, P_{loss} includes the energy that's transferred to the insulation material, the convection and radiation heat loss from all apparatus surfaces to the ambient air. Quantification of the last two terms is the subject of the following subsections.

3.2 CSBC Power Loss Calibration

P_{loss} was evaluated using the data collected in the calibration experiments as described in Chapter 2.3. An example of the data is shown in Figure 10. The dummy battery temperature, T_{dummy} , was close to the slug temperature for all heating conditions.

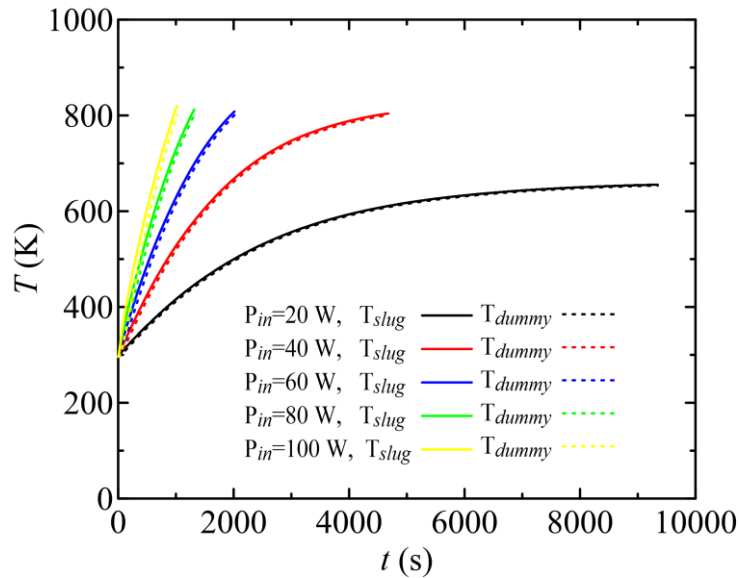


Figure 10. An example of data collected in power loss calibration experiments.

For these experiments, $P_{IHG} = 0$; c_{LIB} is the heat capacity of copper; and m_{LIB} is the directly measured mass of the dummy battery. Therefore, the value of P_{loss} can be

computed from the measured temperatures using Equation (1). In these calculations, $\frac{dT_{slug}}{dt}$ in the battery term was replaced with $\frac{1}{2} \frac{d(T_{slug} + T_{dummy})}{dt}$ to take into account minor temperature non-uniformities observed in the system. The results of these calculations are presented in Figure 11. These results indicate that P_{loss} increases with increasing slug temperature and heating power. The noise in P_{loss} is produced by a numerical differentiation of the temperature data.

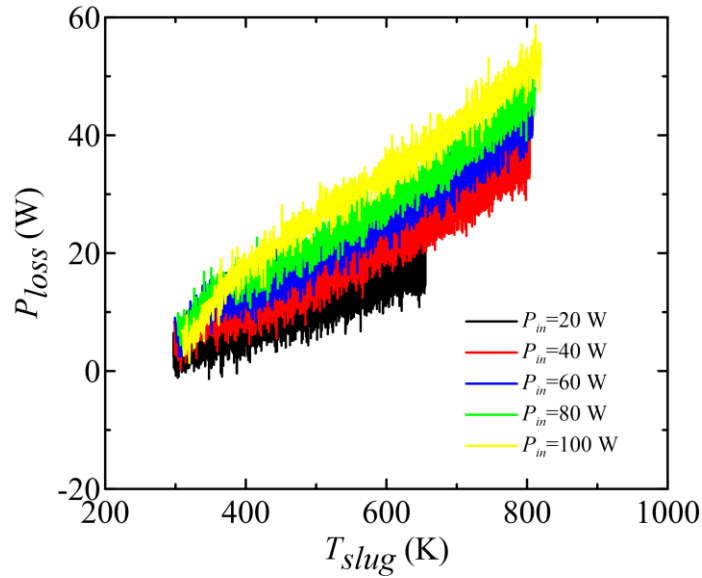


Figure 11. Energy loss rates computed from the temperature data collected in the power loss calibration experiments.

Here it was hypothesized that the rate of energy loss can be represented by an empirical dependence of the form:

$$P_{loss} = A_0 + A_1 T_{slug} + A_4 T_{slug}^4 + B \frac{dT_{slug}}{dt} \quad (2)$$

where A_0 , A_1 and A_4 are constants and B is a function of the slug temperature,

$$B = b_0 + b_1 T_{slug} + b_2 T_{slug}^2 + b_3 T_{slug}^3 + b_4 T_{slug}^4 \quad (3)$$

This expression for P_{loss} was parameterized as follows. The values of the polynomial coefficients, b_i , were selected to minimize the difference in $\left[P_{loss} - B \frac{dT_{slug}}{dt} \right]$ calculated from the results of the calibration tests conducted at different P_{in} . A representative example of the results of this exercise is shown in Figure 12. Subsequently, all overlapping, heating-rate-corrected power loss curves were fitted with the sum of the first three right-hand-side terms in Equation (2). The results of this fitting procedure are also shown in Figure 12 as a black dashed line.

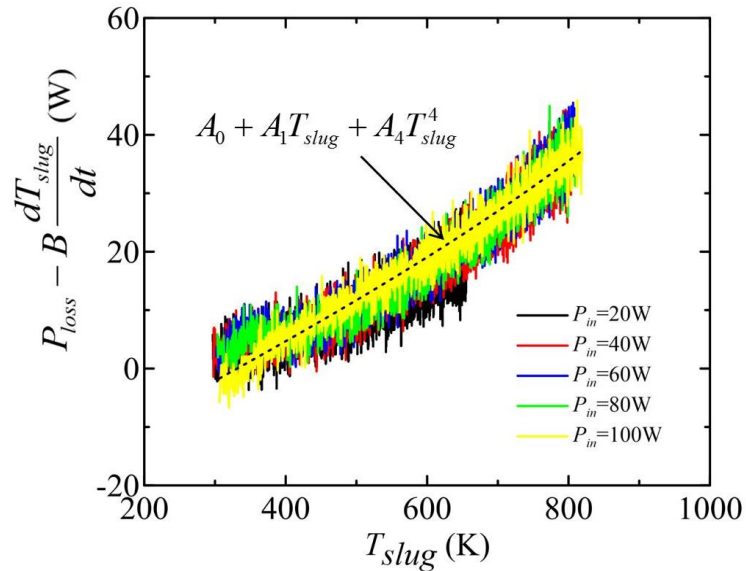


Figure 12. Power loss corrected for heating rate dependence.

This analysis produced an expression for P_{loss} that accurately represented a given series of the calibration experiments. Typical values of the coefficients obtained with this analysis are given in Table 3. To make sure that any potential impact of apparatus changes associated with multiple heating/cooling cycles on the heat loss is taken into account, the power loss calibration tests and the analysis were conducted regularly.

However, because of the structural stability of the thermal insulation material adopted in CSBC, the change in power loss was found fairly minor, thus negligible.

Table 3. Typical coefficients obtained for the energy loss rate expression (Equations (2) and (3)).

Coefficient	Value	Units
A_0	-1.14×10^1	W
A_1	4.00×10^{-2}	W K
A_4	4.90×10^{-11}	W K ⁻⁴
b_0	-1.15×10^2	J K ⁻¹
b_1	7.00×10^{-1}	J K ⁻²
b_2	-1.20×10^{-3}	J K ⁻³
b_3	8.30×10^{-7}	J K ⁻⁴
b_4	-1.20×10^{-10}	J K ⁻⁵

3.3 LIB Heat Capacity and Mass

The LIB's heat capacity (C_{LIB}), the value of which is necessary to quantify the second right-hand-side term in Equation (1), was computed from the results of the open atmosphere experiments. Representative T_{slug} histories obtained in these experiments at various SOCs are shown in Figure 13 (LCO), Figure 14 (NMC) and Figure 15 (LFP). The times and temperatures of the onset of safety venting and onset of thermal runaway are indicated in these figures. Detailed time and temperature of onset of those failure are reported and compared in Chapter 4.

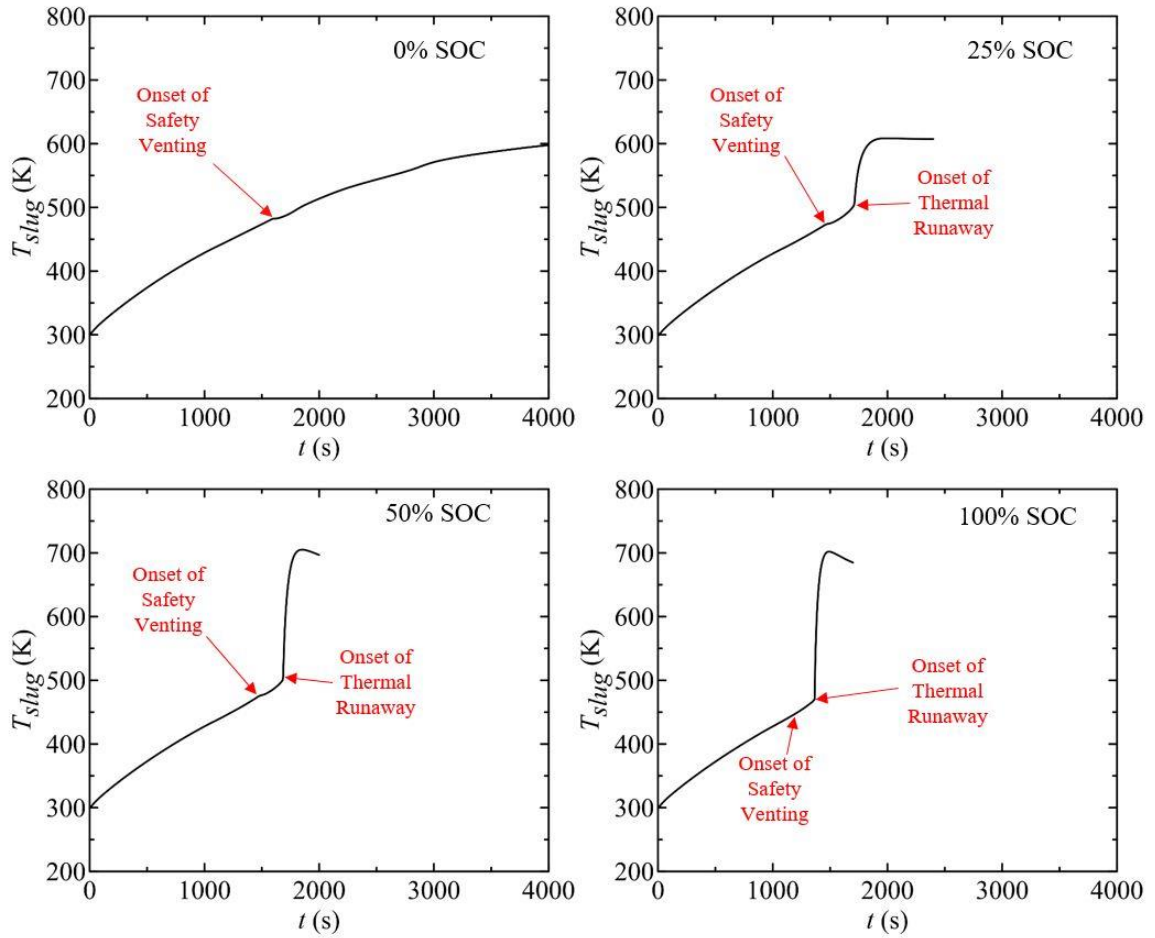


Figure 13. Representative temperature histories for LCO LIBs measured in the CSBC experiments conducted in open atmosphere ($P_{in}=20$ W).

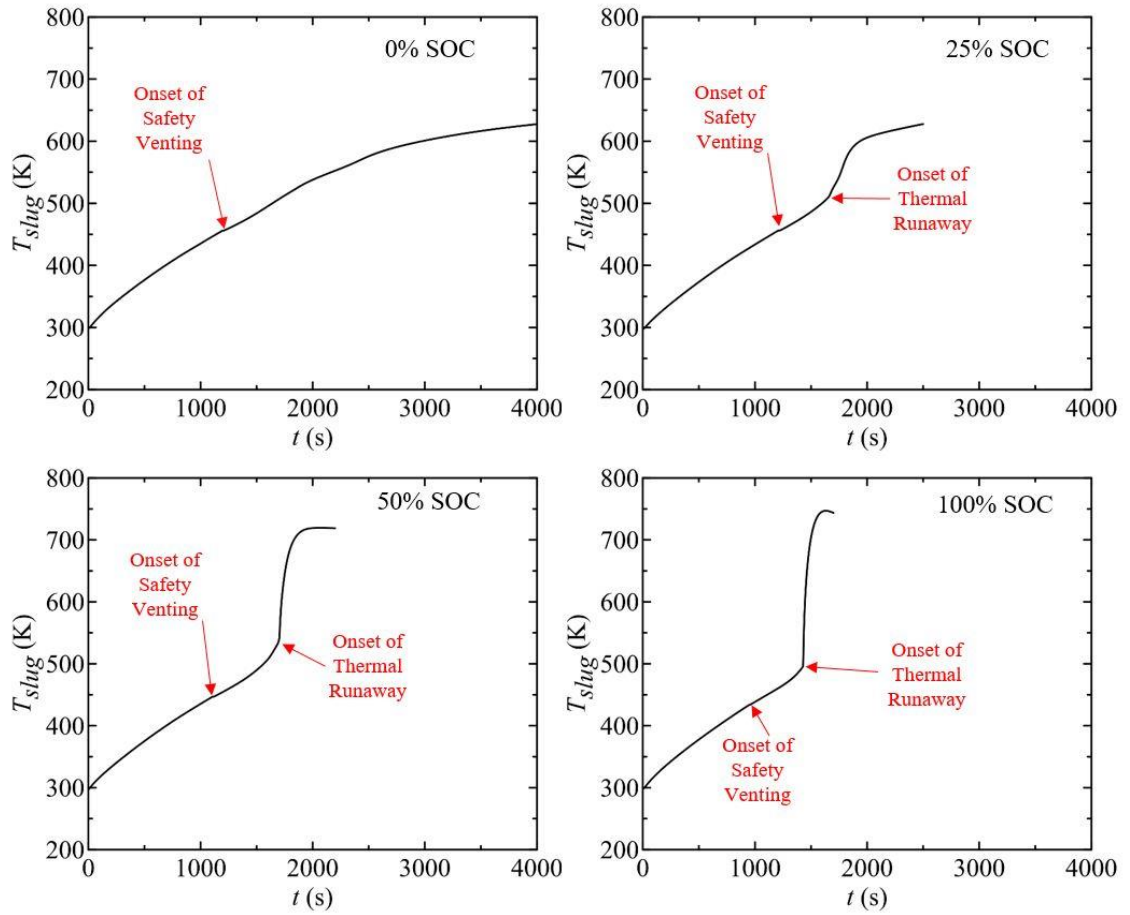


Figure 14. Representative temperature histories for NMC LIBs measured in the CSBC experiments conducted in open atmosphere ($P_{in}=20$ W).

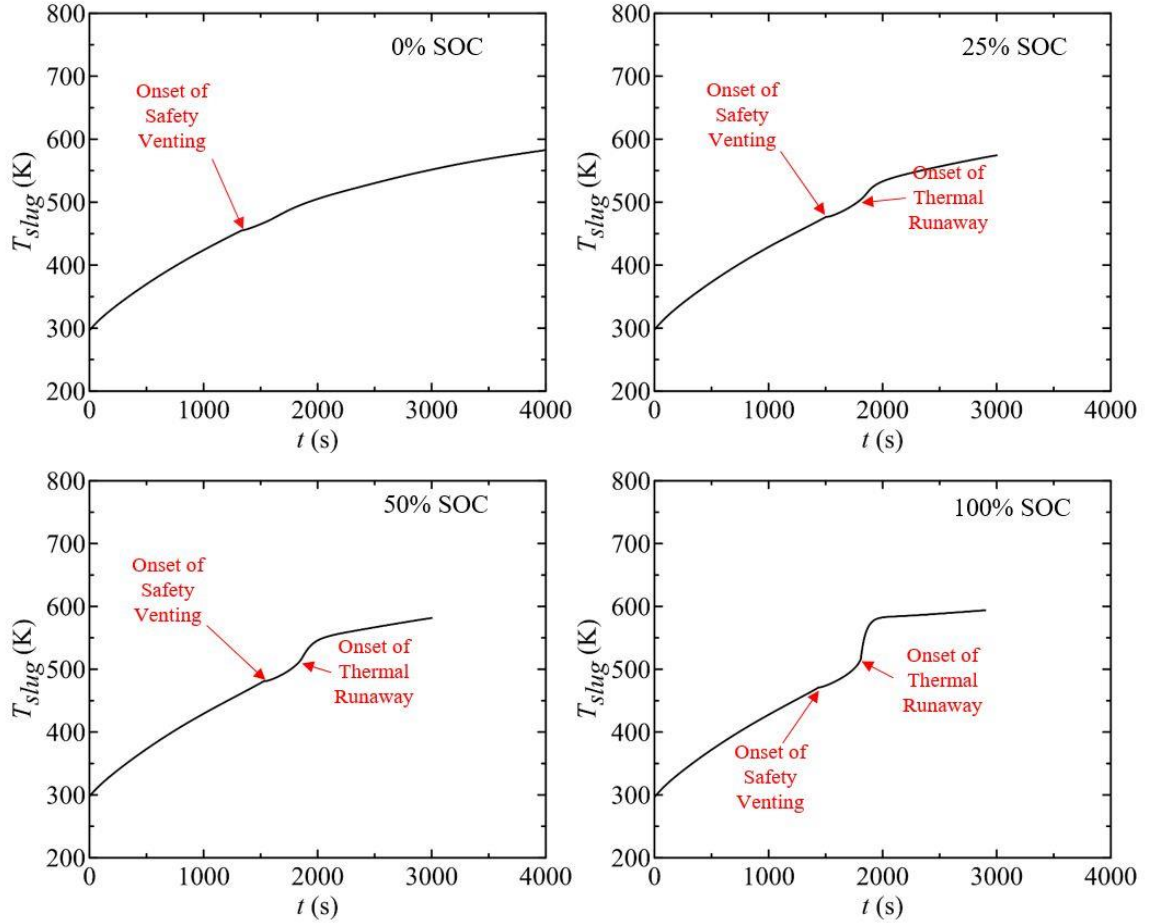


Figure 15. Representative temperature histories for LFP LIBs measured in the CSBC experiments conducted in open atmosphere ($P_{in}=20$ W).

Assuming that before the onset of safety venting there is no significant chemical or physical transformations inside the battery (i.e., $P_{IHG}=0$), and that the mass of the battery remains equal to its initial mass, this segment of T_{slug} dependence on time can be used to compute C_{LIB} (using Equation (1) and provided that P_{loss} has been quantified). The results of representative calculations of C_{LIB} are shown as a function of temperature in Figure 16 (LCO), Figure 17 (NMC) and Figure 18 (LFP). Ignoring the initial rises in the heat capacity, which are hypothesized to be associated with initial spatial non-

uniformity of the heating rate, c_{LIB} is essentially independent of temperature or SOC. The mean values of c_{LIB} , obtained from the results of 40 CSBC tests for each battery type, were all found to be $1.1 \pm 0.1 \text{ J g}^{-1} \text{ K}^{-1}$. The uncertainties of all results of this study are reported as two standard deviations of the mean. Using the same methodology, the heat capacity of the batteries that underwent thermal runaway was measured and found to be indistinguishable from that of the operational LIBs. This value of c_{LIB} was found to be comparable to what was evaluated previously by Maleki et al. [76] and Kawaji et al. [77].

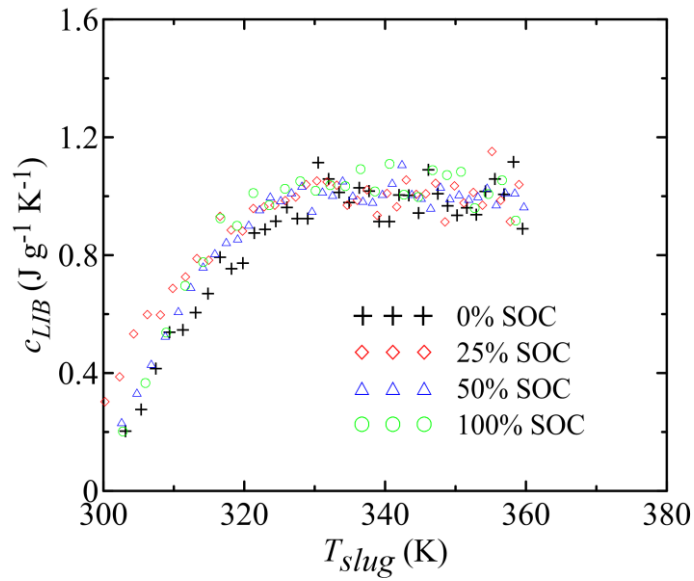


Figure 16. Heat capacity of LCO LIBs calculated from the results of the CSBC experiments conducted in open atmosphere.

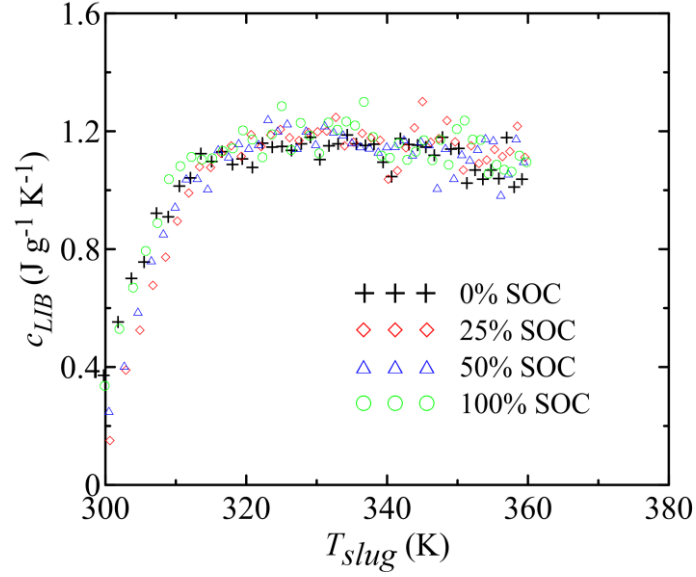


Figure 17. Heat capacity of NMC LIBs calculated from the results of the CSBC experiments conducted in open atmosphere.

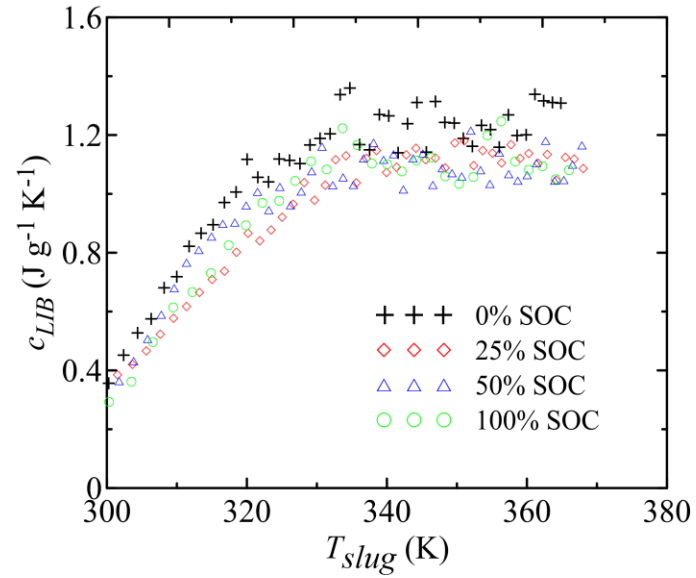


Figure 18. Heat capacity of LFP LIBs calculated from the results of the CSBC experiments conducted in open atmosphere.

In addition to the knowledge of the battery's heat capacity, changes in its mass (m_{LIB}) during the CSBC experiments have to be accounted for to correctly compute the second right-hand-side term in Equation (1). The measurements performed in this study are summarized in Table 4.

Table 4. Averaged mass lost during each failure event for each types of tested LIB.

SOC	LCO		
	Mass Lost During Safety Venting (g)	Mass Lost During Thermal Runaway (g)	Total Mass Lost during Battery Failure (g)
0%	4.5±0.2	0	4.5±0.2
25%	3.0±0.2	1.7±0.1	4.7±0.1
50%	3.0±0.4	3.7±0.2	6.7±0.3
100%	2.5±0.3	13.5±1.5	16.0±1.3
SOC	NMC		
	Mass Lost During Safety Venting (g)	Mass Lost During Thermal Runaway (g)	Total Mass Lost during Battery Failure (g)
0%	5.5±0.1	0	5.5±0.1
25%	3.5±0.4	1.6±0.4	5.1±0.4
50%	4.4±0.2	1.9±0.2	6.3±0.3
100%	5.0±0.5	11.1±0.5	16.1±0.5
SOC	LFP		
	Mass Lost During Safety Venting (g)	Mass Lost During Thermal Runaway (g)	Total Mass Lost during Battery Failure (g)
0%	5.6±0.1	0	5.6±0.1
25%	4.1±0.1	1.3±0.1	5.4±0.1
50%	4.2±0.2	0.9±0.1	5.1±0.2
100%	4.1±0.2	1.2±0.1	5.3±0.2

The results of these measurements, together with the assumption that the venting and thermal runaway ejections occur at a constant rate, were used to construct m_{LIB} evolution profiles. Examples of LCO LIBs are shown in Figure 19, examples of NMC LIBs are shown in Figure 20 and examples for LFP LIBs are shown in Figure 21. An individual profile was constructed for each CSBC open atmosphere experiment to take into account variation in timing of the safety venting and venting associated with the thermal runaway.

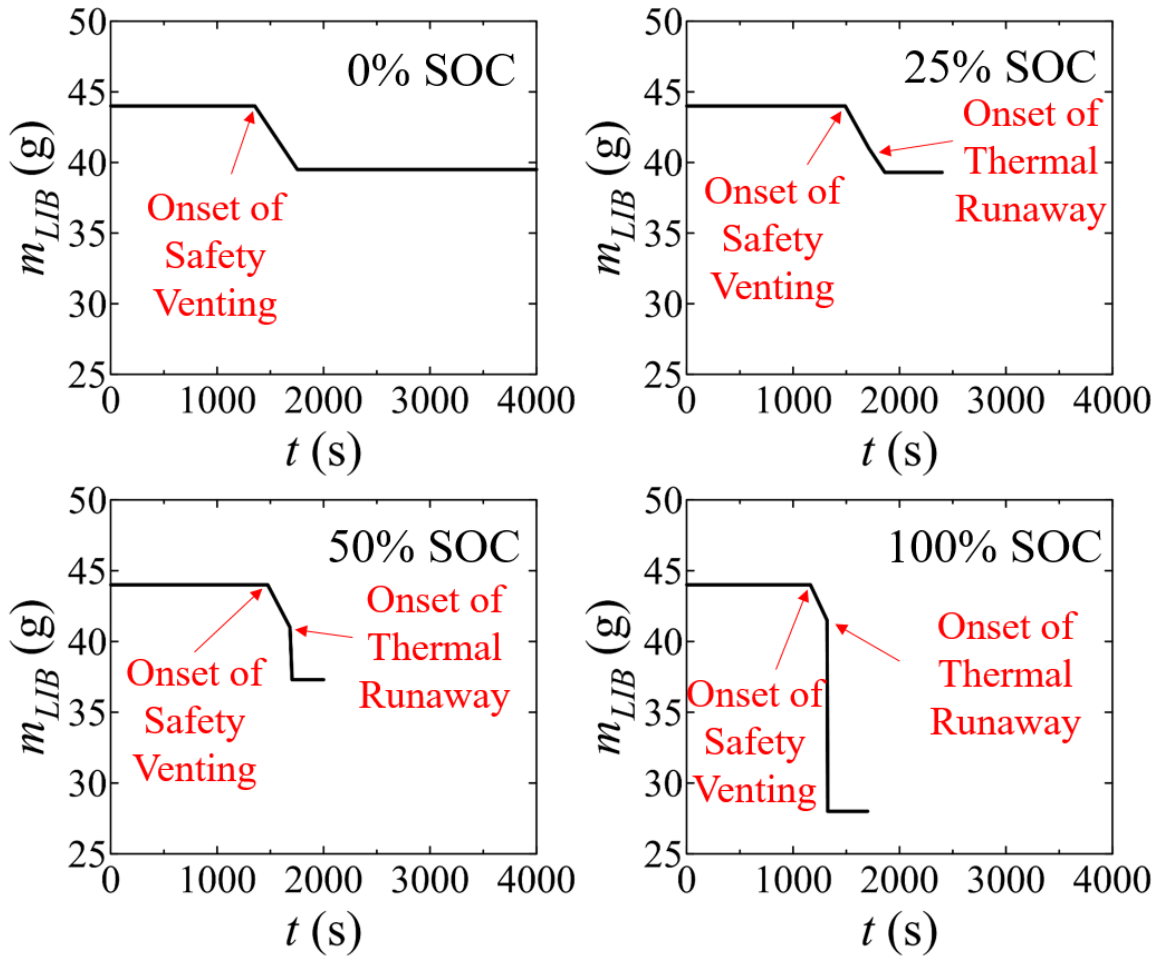


Figure 19. Representative LCO LIBs mass histories ($P_{in}=20$ W) used in the calculation of failure energetics.

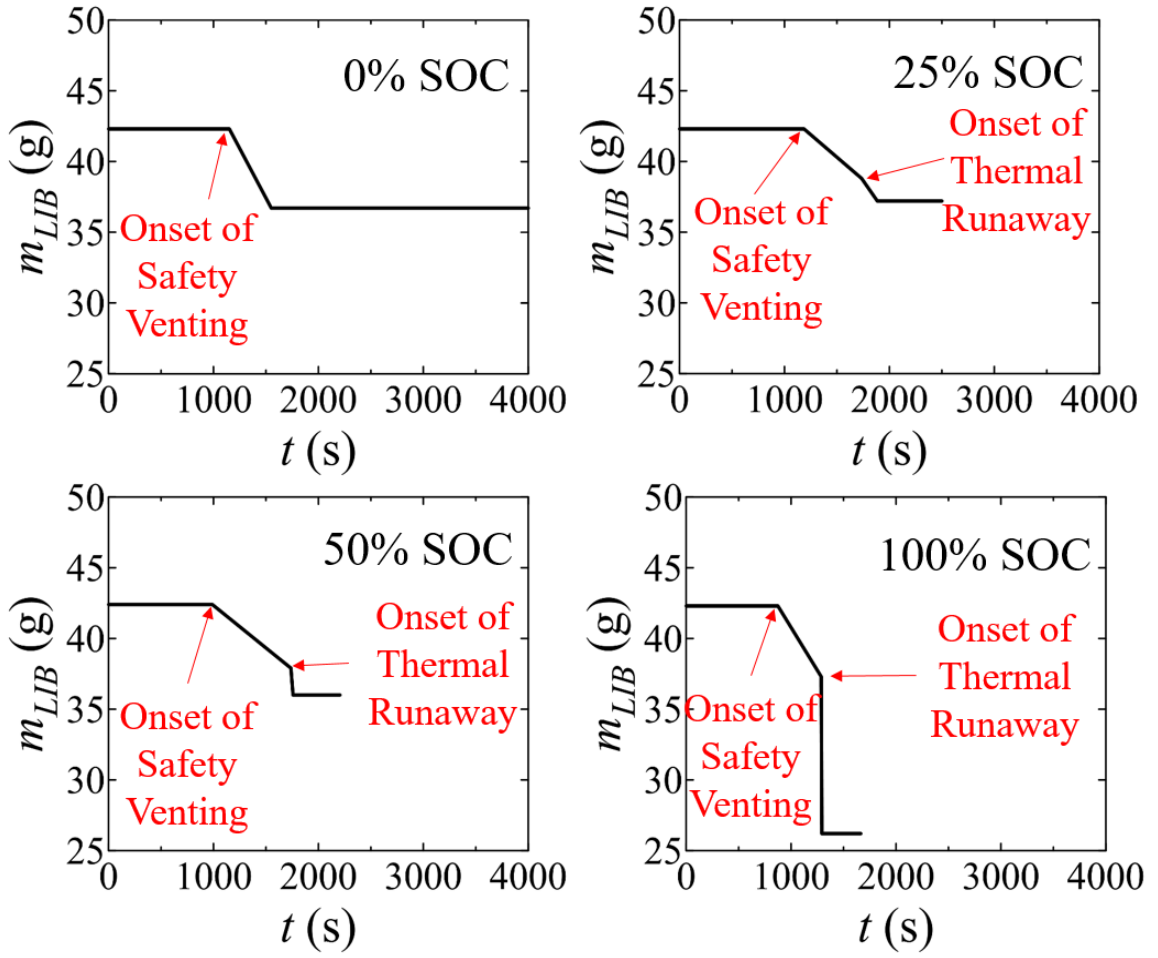


Figure 20. Representative NMC LIBs mass histories ($P_{in}=20$ W) used in the calculation of failure energetics.

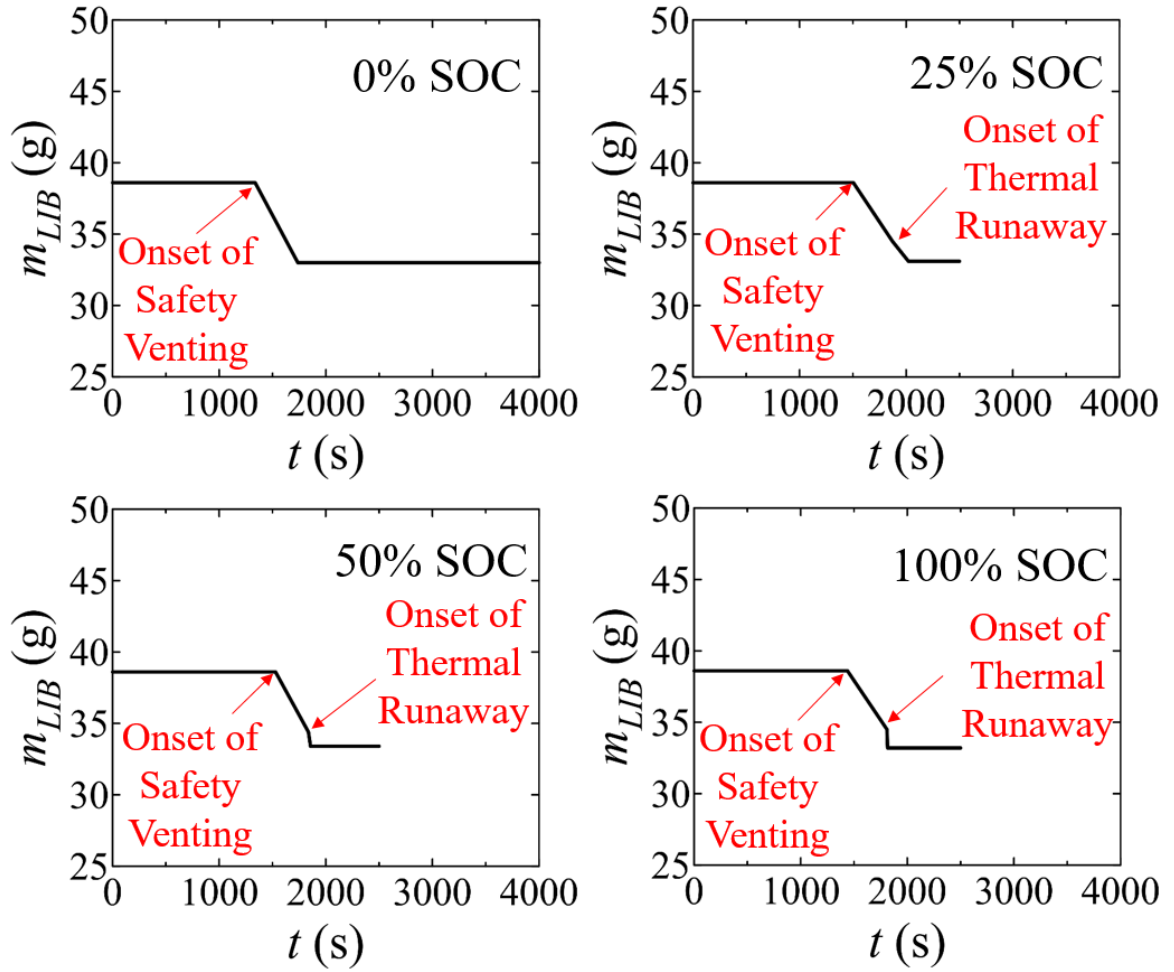


Figure 21. Representative LFP mass histories ($P_m=20$ W) used in the calculation of failure energetics.

Chapter 4: Experimental Results

4.1 Timing and Temperature of LIBs' Thermally-induced Failure

10 stand-alone CSBC experiments were conducted for each type of LIBs at each studies SOC where thermally-induced failure behaviors were carefully observed. Representative copper slug temperature histories measured these experiments for all LIB types and SOC settings are compared in Figure 22. The onset of thermal runaway was detected by observing a sudden boost in the intensity of aerosol jets emanating from safety vent ports and concurrent sharp increase in T_{slug} . The time and temperatures corresponding to the onset of safety venting and thermal runaway are summarized in Table 5 to Table 7 for LCO, NMC and LFP LIB cells, respectively. All uncertainties reported in these tables and in the rest of the manuscript were computed as two standard deviations of the mean. The end of thermal runaway temperatures, also specified in Table 5 to Table 7 were defined to correspond to the final T_{slug} plateau. None of the LIBs at 0% SOC demonstrated an apparent thermal runaway. Therefore, their end of safety venting temperature was defined similarly to that of the end of thermal runaway.

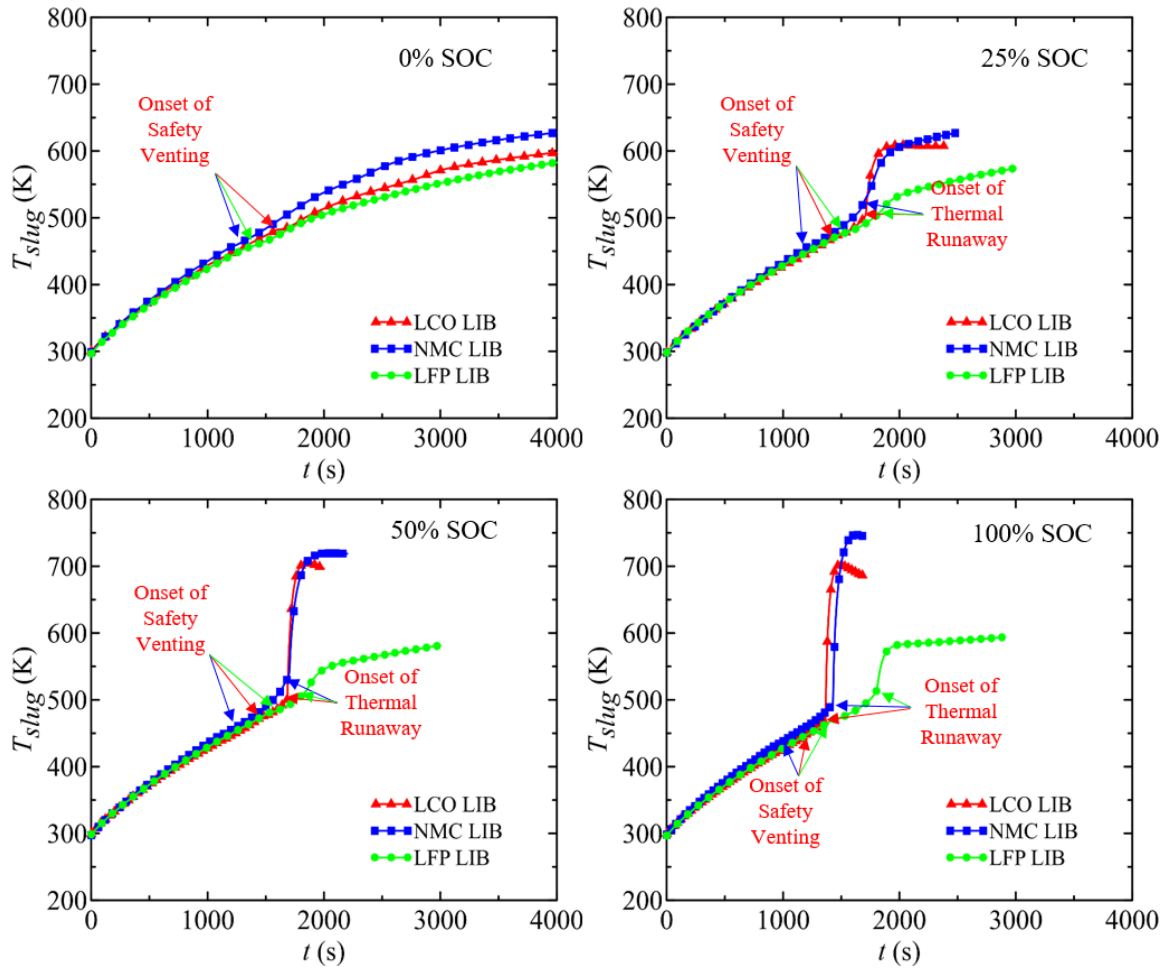


Figure 22. Representative slug temperature histories recorded in the CSBC experiments ($P_{in}=20$ W).

Table 5. Timing and temperature of safety venting and thermal runaway observed in the open atmosphere experiments on LCO LIBs ($P_{in}=20$ W).

SOC	Safety Venting			
	Onset Time (s)	Onset Temperature (K)	End Time (s)	End Temperature (K)
0%	1461±49	470±4	3295±39	581±2
25%	1418±66	468±6	1704±39	505±2
50%	1414±62	470±4	1655±2	500±2
100%	1235±37	451±5	1362±27	470±4
SOC	Thermal Runaway			
	Onset Time (s)	Onset Temperature (K)	End Time (s)	End Temperature (K)
0%	N/A	N/A	N/A	N/A
25%	1704±39	505±2	1987±37	611±5
50%	1655±2	500±2	1891±44	698±6
100%	1362±27	470±4	1547±22	701±20

Table 6. Timing and temperature of safety venting and thermal runaway observed in the open atmosphere experiments on NMC LIBs ($P_{in}=20$ W).

SOC	Safety Venting			
	Onset Time (s)	Onset Temperature (K)	End Time (s)	End Temperature (K)
0%	1160±27	451±4	3103±58	599±5
25%	1166±36	450±3	1685±16	511±1
50%	1105±39	447±4	1697±31	540±3
100%	899±39	428±5	1366±35	494±2
SOC	Thermal Runaway			
	Onset Time (s)	Onset Temperature (K)	End Time (s)	End Temperature (K)
0%	N/A	N/A	N/A	N/A
25%	1685±16	511±1	2221±27	614±2
50%	1697±31	540±3	2019±36	717±5
100%	1366±35	494±2	1556±46	727±13

Table 7. Timing and temperature of safety venting and thermal runaway observed in the open atmosphere experiments on LFP LIBs ($P_{in}=20$ W).

SOC	Safety Venting			
	Onset Time (s)	Onset Temperature (K)	End Time (s)	End Temperature (K)
0%	1284±35	454±3	2201±36	516±3
25%	1456±52	471±5	1871±26	513±2
50%	1439±72	469±6	1846±33	510±1
100%	1442±39	471±3	1816±27	516±2
SOC	Thermal Runaway			
	Onset Time (s)	Onset Temperature (K)	End Time (s)	End Temperature (K)
0%	N/A	N/A	N/A	N/A
25%	1871±26	513±2	2111±30	536±3
50%	1846±33	510±1	2156±33	555±3
100%	1816±27	516±2	2046±19	584±2

In general, for different battery chemistries at the same SOC, the temperature profiles followed similar behaviors. For example, all three types of tested LIBs at 0% SOC didn't show obvious thermal runaway. After onset of safety venting, the temperature profiles showed some minor fluctuations. For all higher SOC (25%, 50% and 100%), LCO and NMC LIBs will produce comparable plateau temperature, both are higher than LFP LIBs. This indicates lower magnitude of energy was generated by LFP LIBs compared to LCO and NMC, and LCO and NMC LIBs produced comparable amount of energy if at the same SOC. The temperature change after the onset of thermal runaway was generally the fastest for LCO LIBs.

With the exception of NMC cells at 100% SOC, the onset of safety venting temperatures were found to be in the range between about 450 and 470 K. The fully charged NMC cells started venting at temperatures 20 K below this range. The onset of thermal runaway occurred between 490 and 540 K in all batteries with the exception of fully charged LCO cells, for which the thermal runaway initiated 20 K below this range.

Neither the safety venting nor thermal runaway temperatures demonstrated a clear trend with respect to SOC or battery chemistry.

4.2 Internal Heat Generation

Based on Equation (1), representative internal heat generation rates (P_{IHG}) computed from the T_{slug} and m_{LIB} data are shown in Figure 23, Figure 24 and Figure 25 for LCO, NMC and LFP LIBs, respectively.

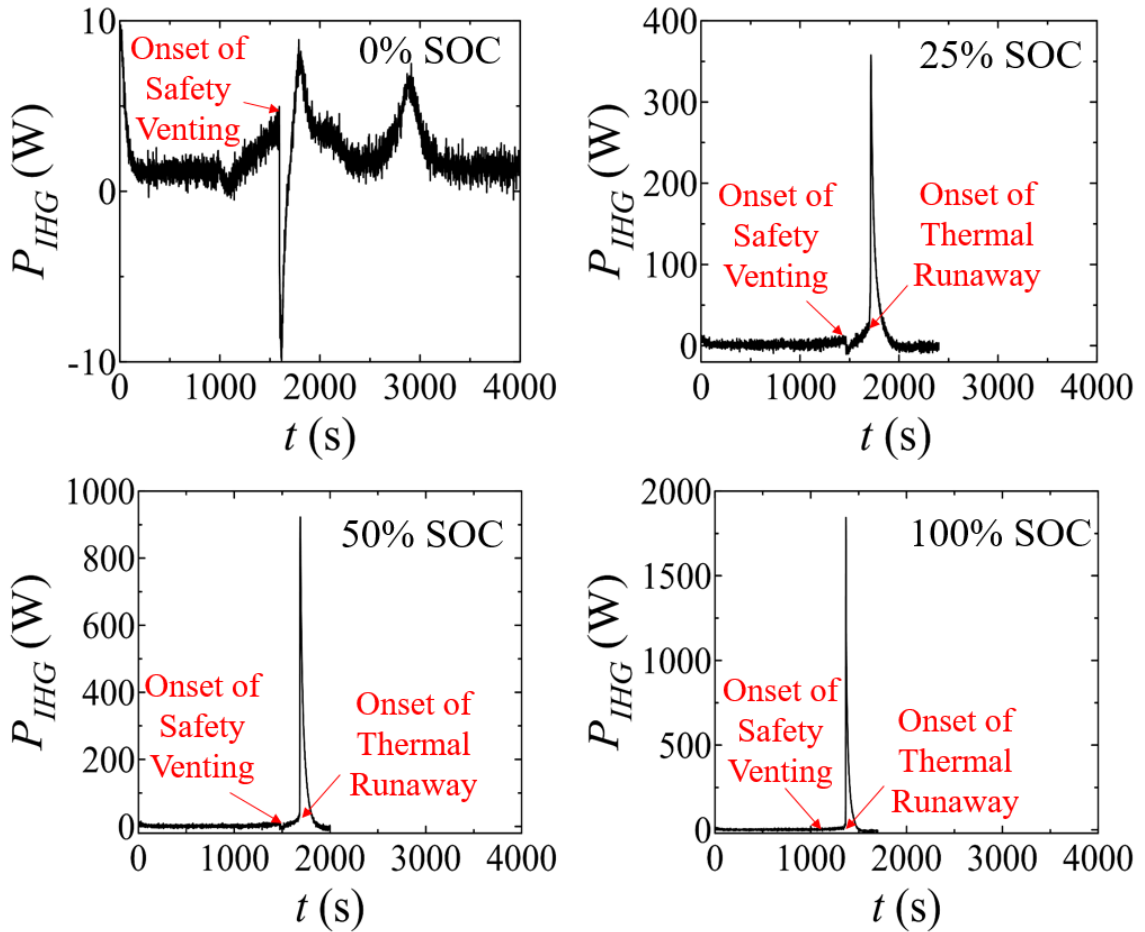


Figure 23. Internal heat generation by the processes inside LCO LIBs during their thermal failure ($P_{in} = 20$ W).

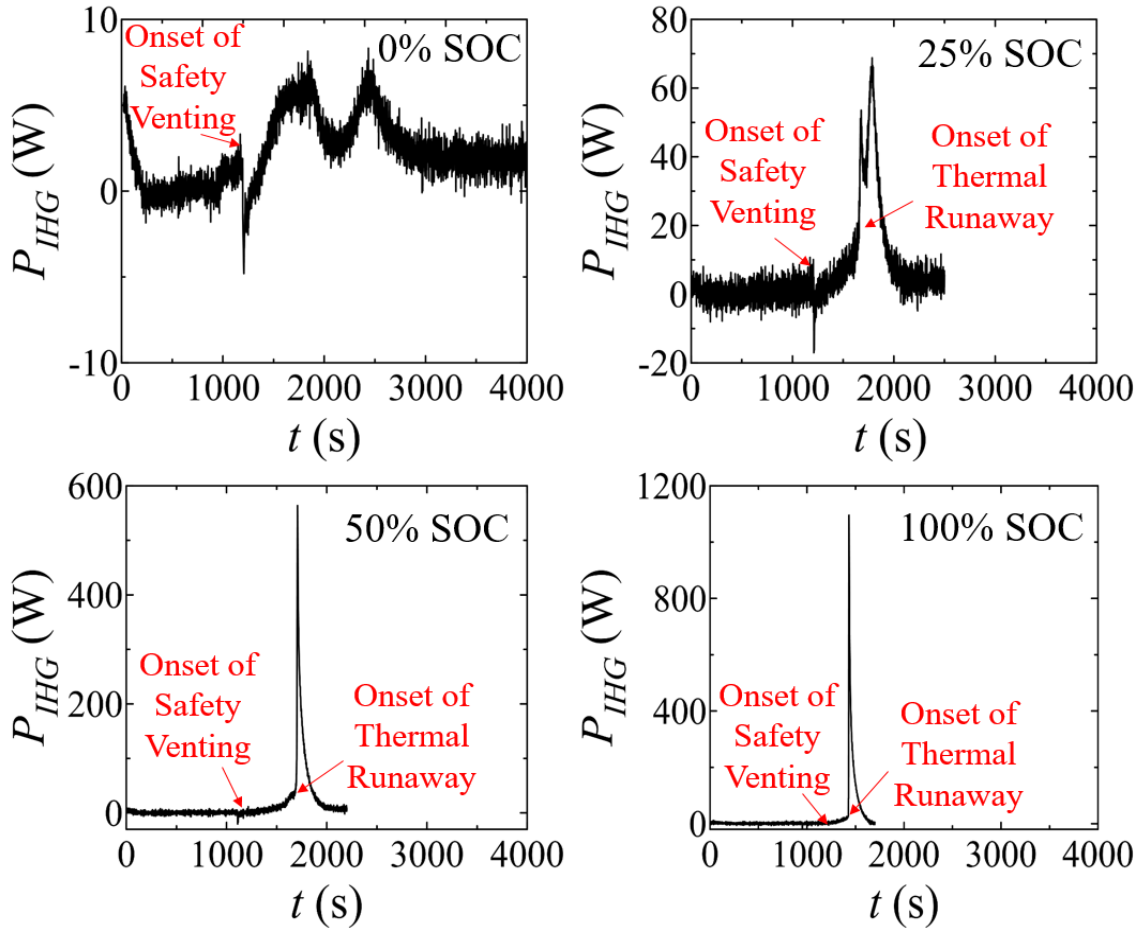


Figure 24. Internal heat generation by the processes inside NMC LIBs during their thermal failure ($P_{in} = 20$ W).

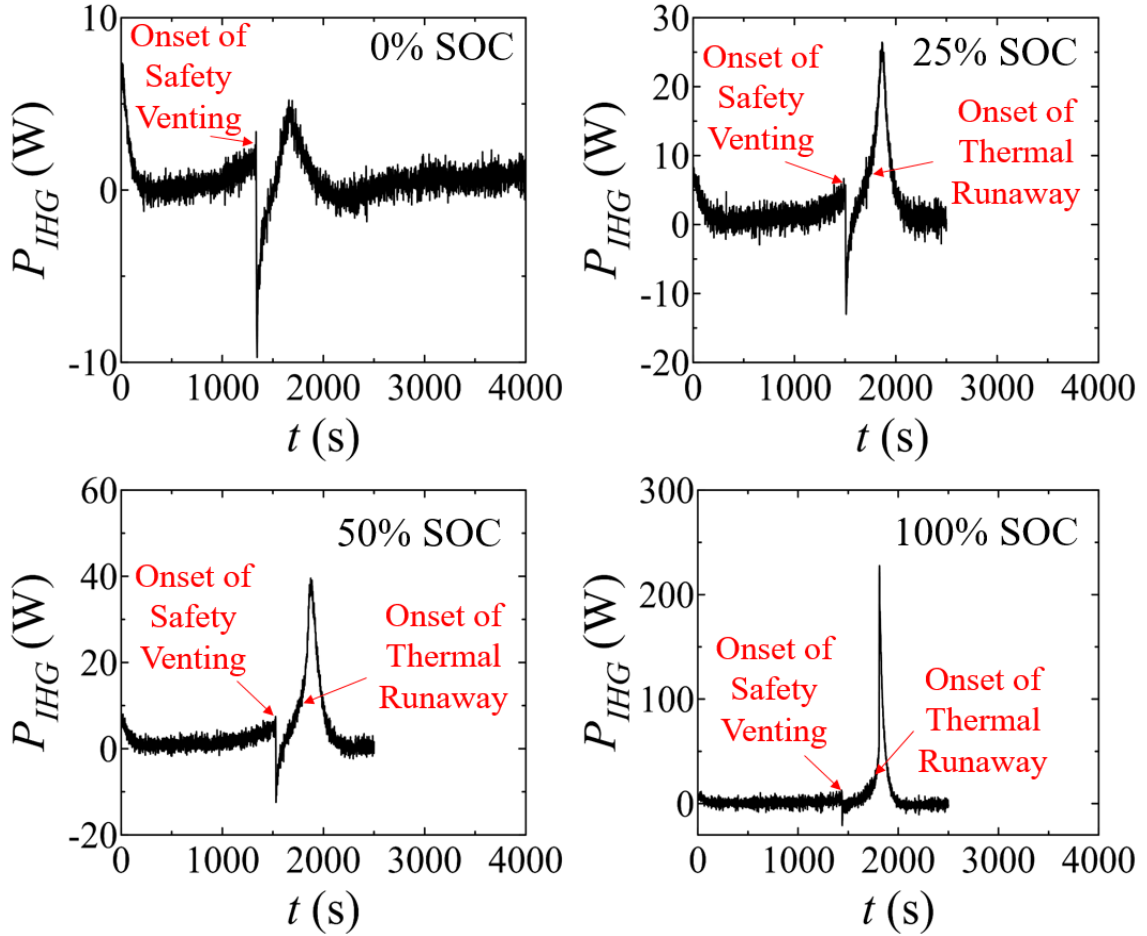


Figure 25. Internal heat generation by the processes inside LFP LIBs during their thermal failure ($P_{in} = 20$ W).

In general, each P_{IHG} profile contains a small but persistent endothermic peak detected at all SOC and for all battery types, which is speculated to be associated with the vaporization of electrolyte. The timing of this peak corresponds to the onset of safety venting. The temperature of this peak is at around 460 K for LCO, 450 K for NMC and 440 K for LFP LIBs, respectively. The intensity of this endothermic peak observed for NMC LIBs is about half as those for LCO and LFP LIBs. These differences are speculated to be associated with difference in electrolyte chemistries equipped in these three battery types.

Two subsequent exothermic peaks are detected for LCO LIBs at 0% SOC as well as NMC LIBs at both 0% and 25% SOCs. These two peaks are possible to correspond to decomposition of the anode and cathode and/or their reactions with organic matter (from remaining electrolyte and separator materials). This pattern, however, is not present anymore for LCO LIBs at 25% SOC or all the LFP LIBs. Instead, a large single peak occupied the period of time associated with the thermal runaway in the P_{IHG} data obtained. It is believed that the two peaks are distinguishable as long as the exothermic chemical reaction corresponding to thermal runaway is not intense enough. In particular, the 0% SOC LIBs doesn't undergo thermal runaway for all three types of LIBs and the NMC LIBs at 25% SOC has fairly small heat release rate during thermal runaway, which results in those observable adjacent peaks. For LCO LIBs at 25% SOC, a single and much higher exothermic peak is observed instead, indicating a much higher exothermic reaction rate related to the thermal runaway. For all three types of batteries at 25%, 50% and 100% SOCs, LCO LIBs tend to have the highest peaks, while LFP tend to have the lowest peaks. It should also be noted that, even at 0% SOC, exothermic processes are still detected for all the tested LIBs.

A numerical integration of the P_{IHG} curves was carried out and its results are reported in Table 8. These integrals represent the total heat produced inside the battery between the onset of safety venting (including the endothermic peak) and the end of thermal runaway (or, in the case of 0% SOC, safety venting). The value of P_{IHG} integral for 100%SOC LCO LIB reported here is consistent with what was reported in a recent FAA report by J. Q. Quintiere et al. [78] for a similar type of LIB sample – 40 kJ/cell. The table also contains the average internal heat generation rates computed by dividing

the P_{IHG} integrals by the duration of time over which these integrals were taken. A graphical representation of both of these quantities is shown in Figure 26. The total heats and average rates are plotted with respect to the electrical energy stored in the battery. It is important to note that, unlike P_{IHG} integrals, the average P_{IHG} values (or any other computed measures of heat generation rate) are specific to the thermal environment of the CSBC experiments and may differ significantly from the internal heat generation rates measured in other scenarios. These values are used here for comparative purposes.

Table 8. Summary of the internal heat generation measurements.

SOC	P_{IHG} Integral (kJ)			Average P_{IHG} (W)		
	LCO	NMC	LFP	LCO	NMC	LFP
0%	8.4±0.6	4.5±0.5	0.7±0.2	3.5±0.2	2.3±0.3	0.5±0.1
25%	21.2±0.6	14.1±0.3	6.6±0.7	35.2±1.0	13.0±0.7	9.5±0.9
50%	37.4±1.1	32.5±1.1	9.7±0.8	62.3±1.8	31.3±3.7	16.2±1.3
100%	37.3±3.3	34.0±1.8	13.7±0.4	62.5±5.5	49.4±3.2	22.8±0.7

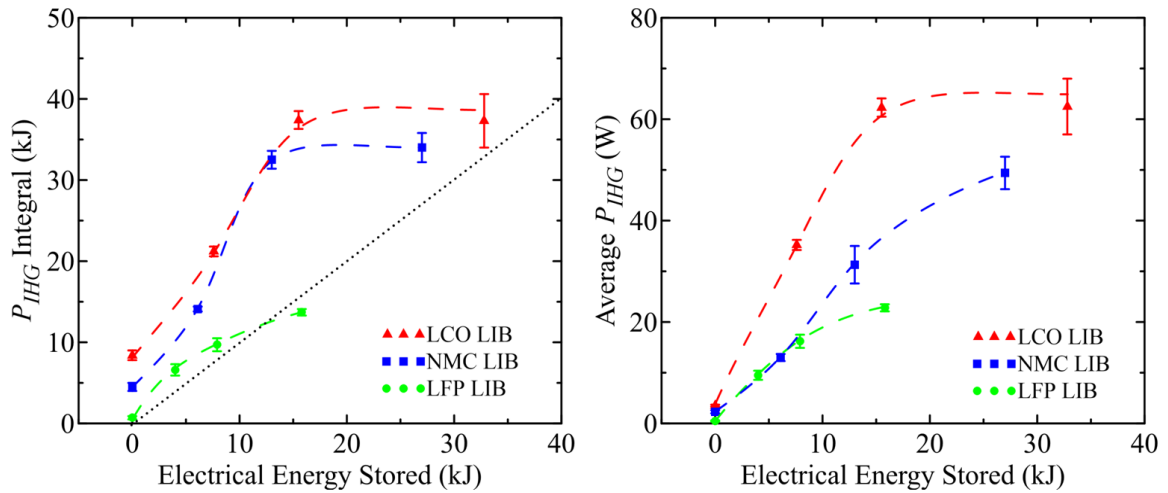


Figure 26. Dependence of the total internal heat produced (left) and average internal heat generation rate (right) on stored electrical energy. The dashed lines are spline interpolations of the displayed experimental data points. The dotted line (in the left graph) is a hypothetical curve for an LIB if it produced heat equal to the stored electrical energy.

For all LIB types, both the total internal heat and the average rate of its production increase with increasing stored electrical energy. However, the rates of these increases become small or negligible as the battery SOC approaches 100%. The LCO released the most internal heat at the highest average rate followed by NMC and LFP cells. This order is consistent with the cell's electric capacities (listed in Table 2). The LFP is the only battery for which the total internal heat falls below the stored electrical energy at 100% SOC (the dotted line in the left graph of Figure 26 represents a hypothetical battery for which the electrical energy and internal heat released are equal). The rest of the LIBs produce significantly more internal heat than the electrical energy that they contain.

It should be noted that the computed P_{IHG} integrals may not represent all heat released in the chemical reactions of LIB materials. As indicated from Figure 19 to Figure 21, a significant fraction of these materials is ejected from the cells during the failure process. Provided that these materials are not immediately consumed in flaming

combustion, the ejected materials may continue to react with themselves and produce heat. This external heat generation is likely to be most significant for the LCO and NMC cells at 100% SOC, which lose over 25% of their mass during the safety venting and thermal runaway.

The external heat generation is not measured directly in the CSBC experiments. However, an estimate of its contribution can be obtained by plotting the P_{IHG} integral with respect to the total mass lost by the cells at 100% SOC. The results of this exercise are shown in Figure 27. For the fully charged LCO and NMC cells, there is a considerable variability in the lost mass; and, as this figure indicates, the mass loss and heat release correlate. It is possible to capture this correlation with a straight line fitted to the data using the assumption that the cell that loses all of its mass generates no heat inside its casing. This provides an extrapolation with an intercept of this line with the ordinate that represents an estimate of the maximum heat that can be produced by the battery materials, assuming that all of the mass is retained inside the battery during the failure process.

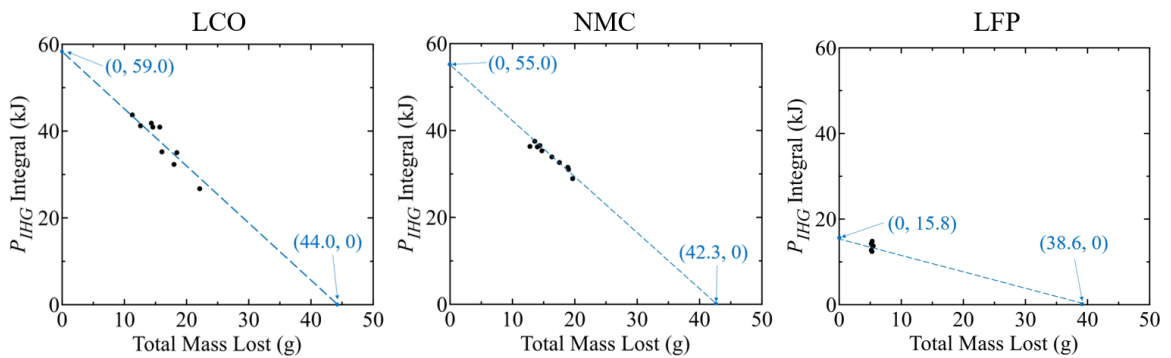


Figure 27. Relations between the total mass lost and heat produced inside LIBs at 100% SOC. The points are experimental data. The dashed lines are extrapolations of the experimental data to zero mass loss conditions.

For LCO and NMC cells, the maximum heat estimates are 59 and 55 kJ/cell, respectively. The former value is within a few percent of that measured directly by Lyon and Walters in the aforementioned reports [41, 42] for the same LIB type and state of charge using inert atmosphere bomb calorimetry. The LFP LIB data, also presented in Figure 27, do not show a correlation between the P_{IHG} integral and mass lost due to absence of any significant variability in the lost mass. Nevertheless, the same extrapolation technique is applied to yield a 15.8 kJ/cell maximum heat estimate, which turns out to be exactly equal to the total electrical energy stored in this battery (see Table 2).

4.3 Temperature Measurements for Radial Thermal Conductivity of LIBs

Figure 28 shows the representative temperature profiles obtained in CSBC tests to determine radial thermal conductivity of all three types of tested LIB samples (Chapter 2.5). The temperatures at copper slug (T_{slug}) are presented in solid lines while those at LIB's axis ($T_{LIB-axis}$) are presented in dashed lines.

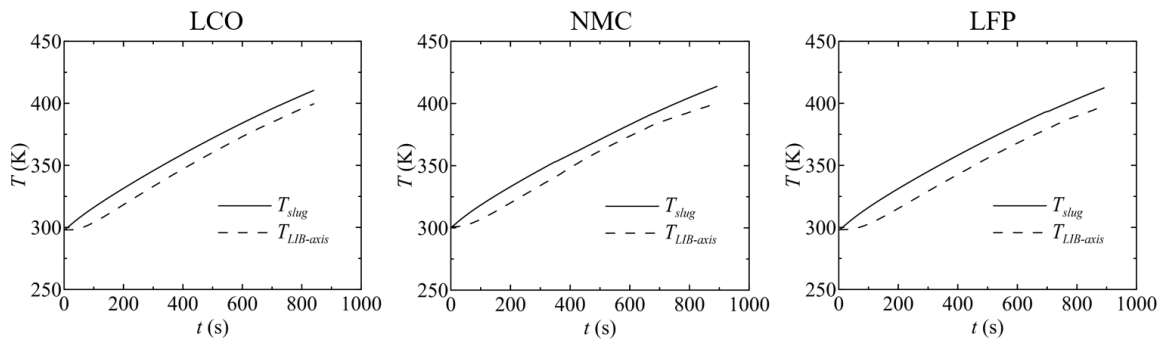


Figure 28. Temperature measurements for radial thermal conductivity of LIBs ($P_{in}=20$ W).

As expected, due the radial thermal conductivity of an LIB cell, a radial temperature gradient was revealed in Figure 28 for all tested LIB samples. These

measurements will be later utilized in numerical modeling to determine the radial thermal conductivity of LIBs via reverse modeling methodology.

4.4 External Flaming Combustion Heat

Representative flaming combustion heat release rate ($P_{Flaming}$) histories obtained for all LIB types and SOC settings are shown from Figure 29 to Figure 31 for LCO, NMC and LFP LIBs, respectively. The curves are separated into 2 segments. One segment is associated with the safety venting, the other – with the thermal runaway. With the exception of 0% SOC cells (which do not experience thermal runaway), the combustion energies released during these stages of failure appear to be similar in magnitude.

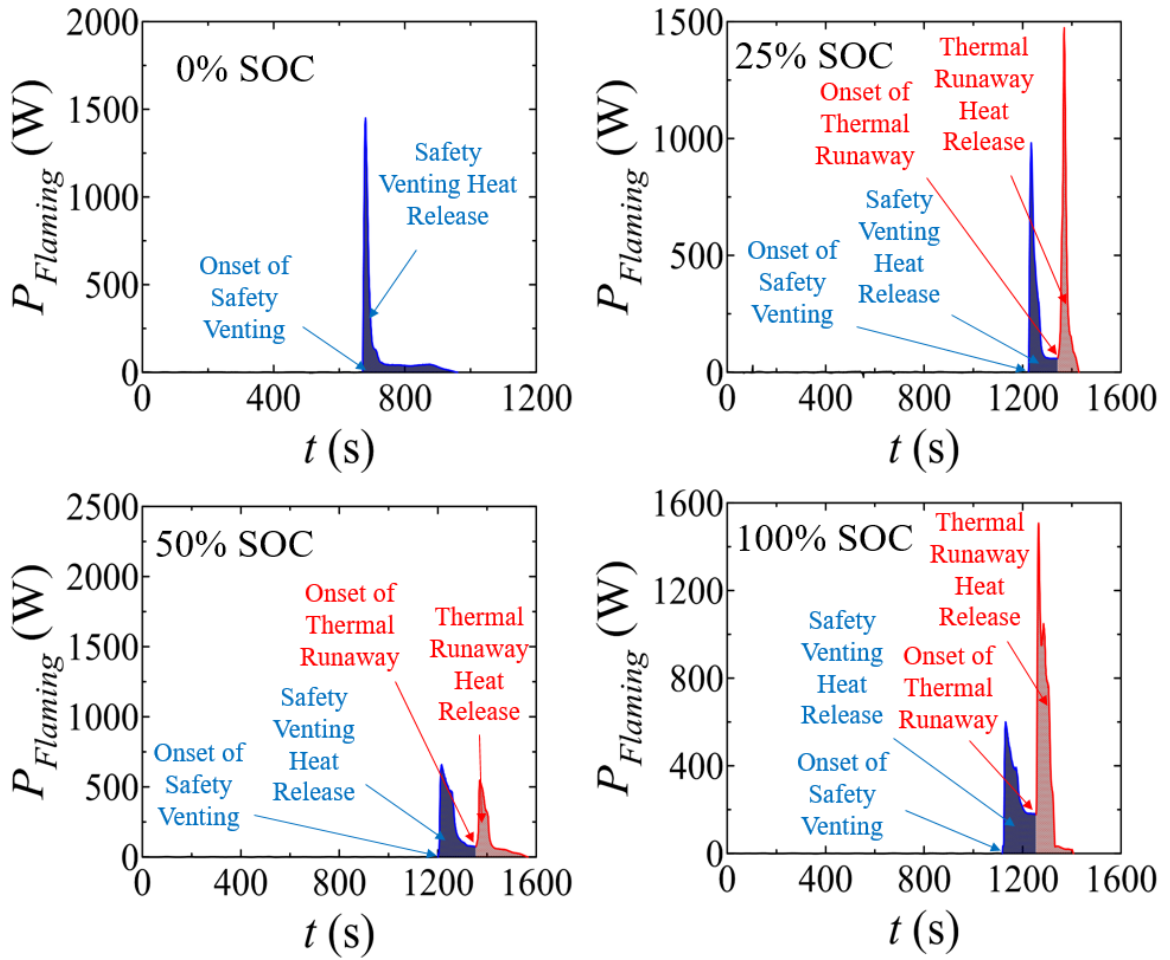


Figure 29. Heat release rate of flaming non-premixed combustion of ejected LCO LIB materials.

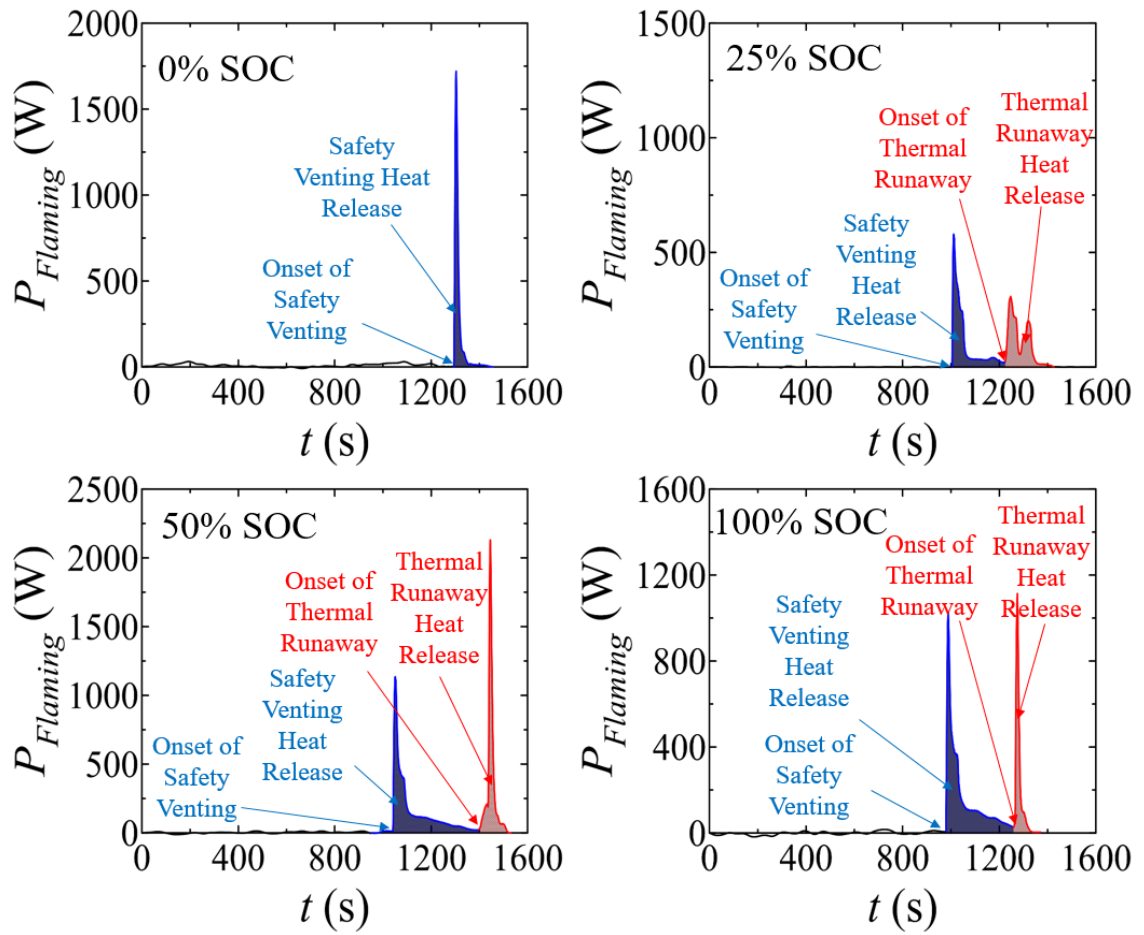


Figure 30. Heat release rate of flaming non-premixed combustion of ejected NMC LIB materials.

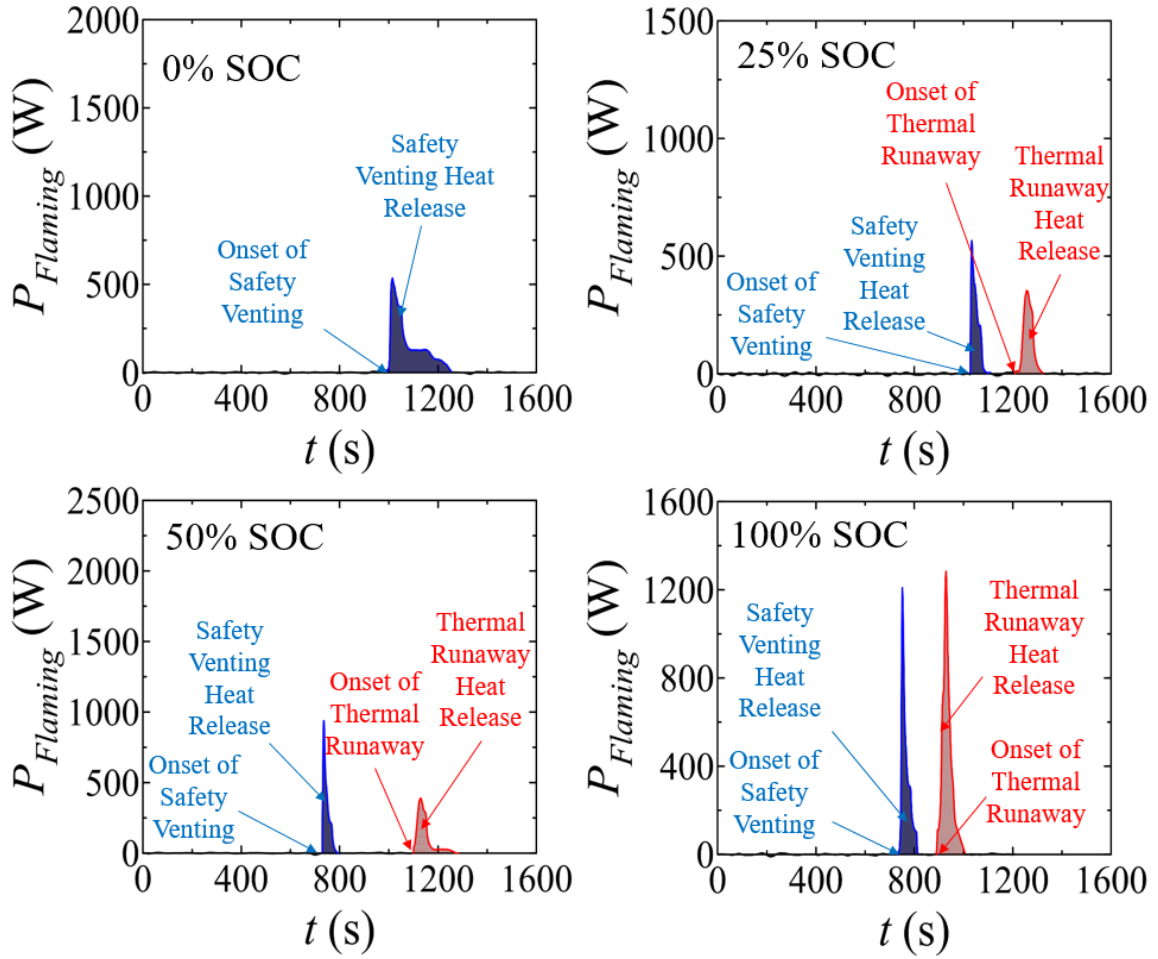


Figure 31. Heat release rate of flaming non-premixed combustion of ejected LFP LIB materials.

A numerical integration of the $P_{Flaming}$ curves (including both safety venting and thermal runaway stages of failure) yields the total heat of flaming combustion. This integration was performed from the point in time when $P_{Flaming}$ rises 30 W above the baseline for the first time to the point when $P_{Flaming}$ returns to the baseline. The $P_{Flaming}$ integrals are reported in Table 9 together with the average rates of heat generation, which were calculated by dividing the $P_{Flaming}$ integrals by the corresponding time periods used in the integration. A graphical representation of both of these quantities is shown in

Figure 32. As in the case of the internal heat generation, the total combustion heats and average rates are plotted with respect to the stored electrical energy.

Table 9. Summary of the cone calorimetry measurements.

SOC	$P_{Flaming}$ Integral (kJ)			Average $P_{Flaming}$ (W)		
	LCO	NMC	LFP	LCO	NMC	LFP
0%	34.8±8.0	26.8±3.7	49.5±5.0	150±27	104±21	177±36
25%	60.8±6.1	45.4±4.6	35.5±3.6	186±36	100±10	95±10
50%	63.0±6.3	80.5±14.5	44.5±11.5	180±18	154±26	114±30
100%	48.7±7.4	64.2±6.4	50.0±5.2	202±36	166±18	122±22

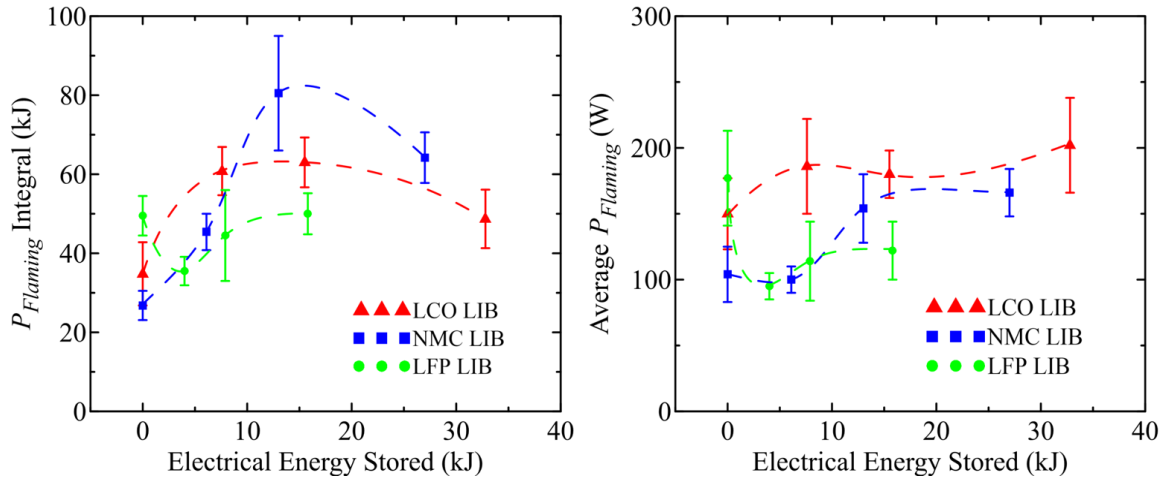


Figure 32. Dependence of the total heat of flaming combustion (left) and average rate of production of this heat (right) on stored electrical energy. The dashed lines are spline interpolations of the displayed experimental data points.

The total combustion heats are between 0.3 and 70 times higher than the corresponding P_{IHG} integrals. The rates of these distinct heat generation processes are even further apart, with flaming combustion being at least 3 times higher. Unlike P_{IHG}

integrals, $P_{Flaming}$ integrals do not demonstrate a systematic dependence on the cathode chemistry or SOC.

One phenomenon that may contribute to the absence of these dependencies was revealed through analysis of the video recordings of these experiments. It is apparent from the videos that the flame supported by the ejected battery materials was intermittent (several moments of flaming combustion during the thermal runaway of a 100% SOC LIB are shown in Figure 33), even though the ejection process was continuous. This intermittency was thought to arise from high hydrodynamic strain rates associated with a high velocity of the ejected matter at the early phases of safety venting and thermal runaway. This intermittency exists despite a continuously operating hot wire igniter located on the path of the ejected gases and aerosols. Same phenomena was also reported in the aforementioned FAA report [78].

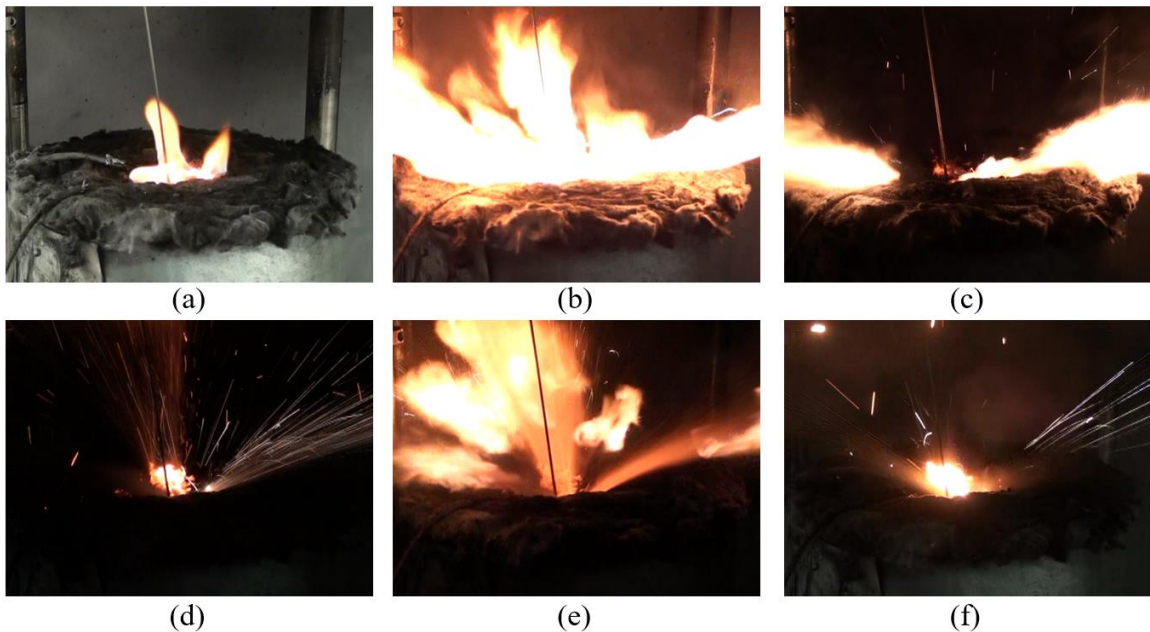


Figure 33. Experimental observation of intermittent combustion after the onset of thermal runaway of a 100% SOC LIB.

To provide a rough estimate of the fraction of ejected battery materials that escape without combustion (and therefore do not contribute to the measured $P_{Flaming}$), the videos were analyzed to compute the fraction of time that the flame was absent while the venting persisted. This fraction of time was found to be between 10% and 30% for all battery types and SOC settings; it did not show a clear dependence on SOC or battery chemistry.

4.5 CSBC Test in Nitrogen Atmosphere

As shown in Figure 34, T_{slug} histories obtained from the nitrogen atmosphere experiments on 100% SOC NMC LIBs are comparable to those measured in the open atmosphere experiments. This observation indicates that the heat feedback from a flame, which was observed during the thermal runaway phase of the open atmosphere experiments, had no significant impact on the computed P_{IHG} profiles. The oxygen concentration histories measured in the nitrogen atmosphere experiments show a slight, ≈ 0.05 vol.%, and brief, ≈ 50 s, increase at the onset of the thermal runaway. It is not clear whether this increase is due to the oxygen production by the battery or is a result of reaction of the gas analyzer to a pressure pulse produced by the battery materials ejected into an air-tight container. Even if the former explanation is correct (i.e., the battery does generate oxygen during its thermal runaway), the amount of oxygen produced is too small to impact the cone calorimetry measurement of $P_{Flaming}$.

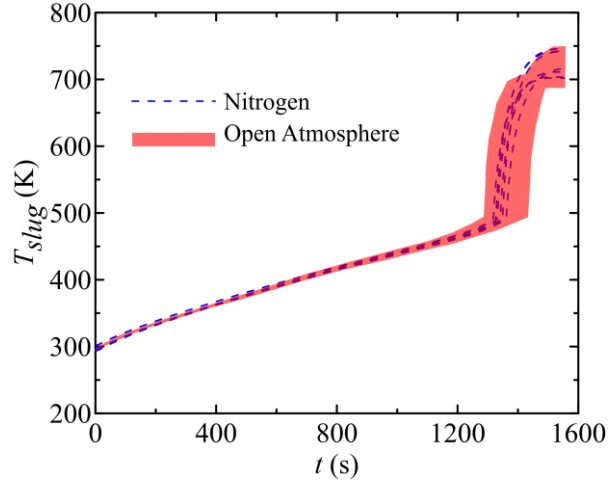


Figure 34. Comparison of the results of nitrogen atmosphere and open atmosphere CSBC experiments performed on 100% SOC NMC LIBs ($P_{in}=20$ W).

4.6 CSBC Tests for Model Validations

4.6.1 LCO LIBs at 100% SOC Heated by a Range of Heating Rates

Additional non-standard CSBC tests were conducted for LCO LIBs, where sample cells were charged to 100% SOC but heated by P_{in} ranging from 40 W to 100 W with an increment of 20 W. Figure 35 shows the averaged T_{slug} histories measured in these experiments, where the uncertainties are reported as two standard deviations of the mean. It is found that the temperature level reached after the onset of thermal runaway shown in these profiles were comparable since all the tested samples were at the same SOC. As P_{in} went higher than 60 W, no plateau temperature was reached since this high heating rate would continue to heat up the whole system.

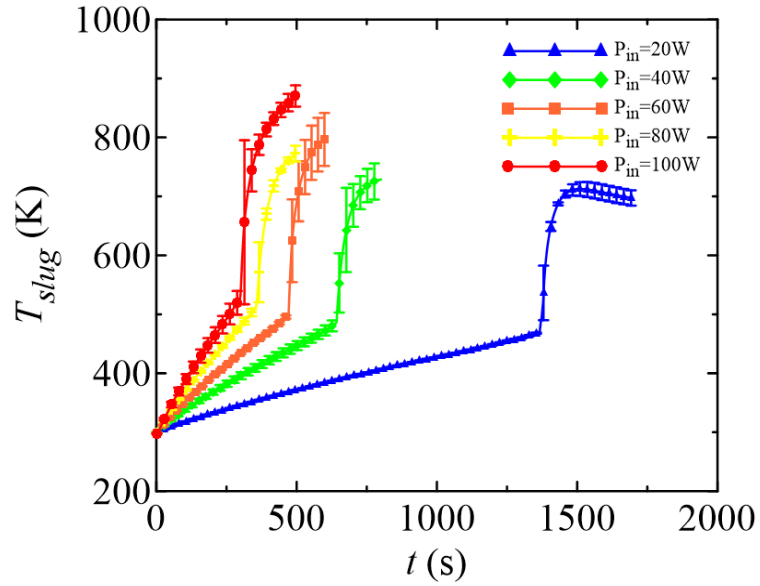


Figure 35. Representative slug temperature histories recorded in CSBC experiments with P_{in} ranging from 40 W to 100 W.

Same as the standard CSBC tests, the onset of thermal runaway in these tests was also detected by observing a sudden boost of venting intensity and it was always with a sharp increase in T_{slug} profiles. As P_{in} went up, the onset time of thermal runaway tended to be shorter. Figure 36 shows the onset time of thermal runaway decreased with increasing heating rates.

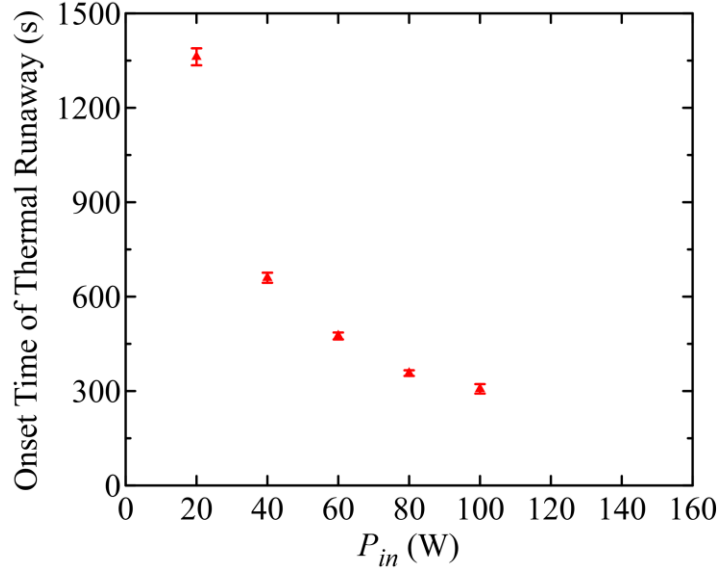


Figure 36. Relations between the heating rate P_{in} and the onset time of thermal runaway for tested LIBs at 100% SOC.

4.6.2 CSBC Tests on LCO LIBs at 75% SOC

One last type of CSBC tests were conducted for the purpose of validation of the thermo-kinetic battery failure model – LCO LIB cells were charged to 75% SOC and heated by P_{in} of 20 W in CSBC. 3 such experiments were conducted. The averaged measurement of T_{slug} is shown and compared with other standard CSBC T_{slug} profiles in Figure 37, where the uncertainties are calculated as two standard deviations of the mean.

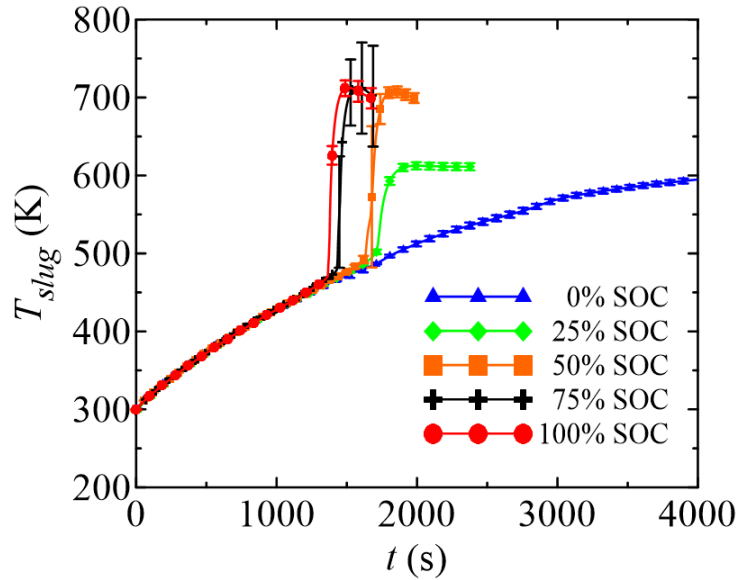


Figure 37. Representative slug temperature histories recorded in CSBC experiments with LCO LIB's SOC's ranging from 0% to 100%.

The onset of thermal runaway, again, was defined as the point of observing a sudden boost of venting intensity along with a sharp increase in T_{slug} measurement. The onset time and temperature of thermal runaway for 75% SOC LCO cells was found to be relatively higher than those for 100% LCO LIB cells. The plateau level of T_{slug} for 75% SOC LCO cells were found to be similar to both 50% SOC and 100% SOC cells, which indicated that 75% SOC LCO cells can produce around 37 kJ (Table 8) of energy by the reacting material inside the cell during thermal failure. This observation, is consistent with the estimate that can be obtained from Figure 26. It also shows that, once a LCO LIB cell is above 50% SOC and goes to thermal failure, the amount of energy released can be maximized to its capacity.

4.7 Cascading Battery Failure Tests

After each cascading battery failure test, the HD video was analyzed carefully to determine the onset time of thermal runaway of each LIB cell. The definition of thermal

runaway, same as what was adopted in CSBC test analysis, is the point where a sudden boost of venting materials from the LIB cell is observed. Figure 38 shows a representative cascading battery failure test behavior. In this figure, (a) – (c) show the thermal runaway of the 1st row LIB, (d) – (f) show the thermal runaway of the 2nd row LIBs, and the (g) – (i) show the thermal runaway of the 3rd row LIBs.

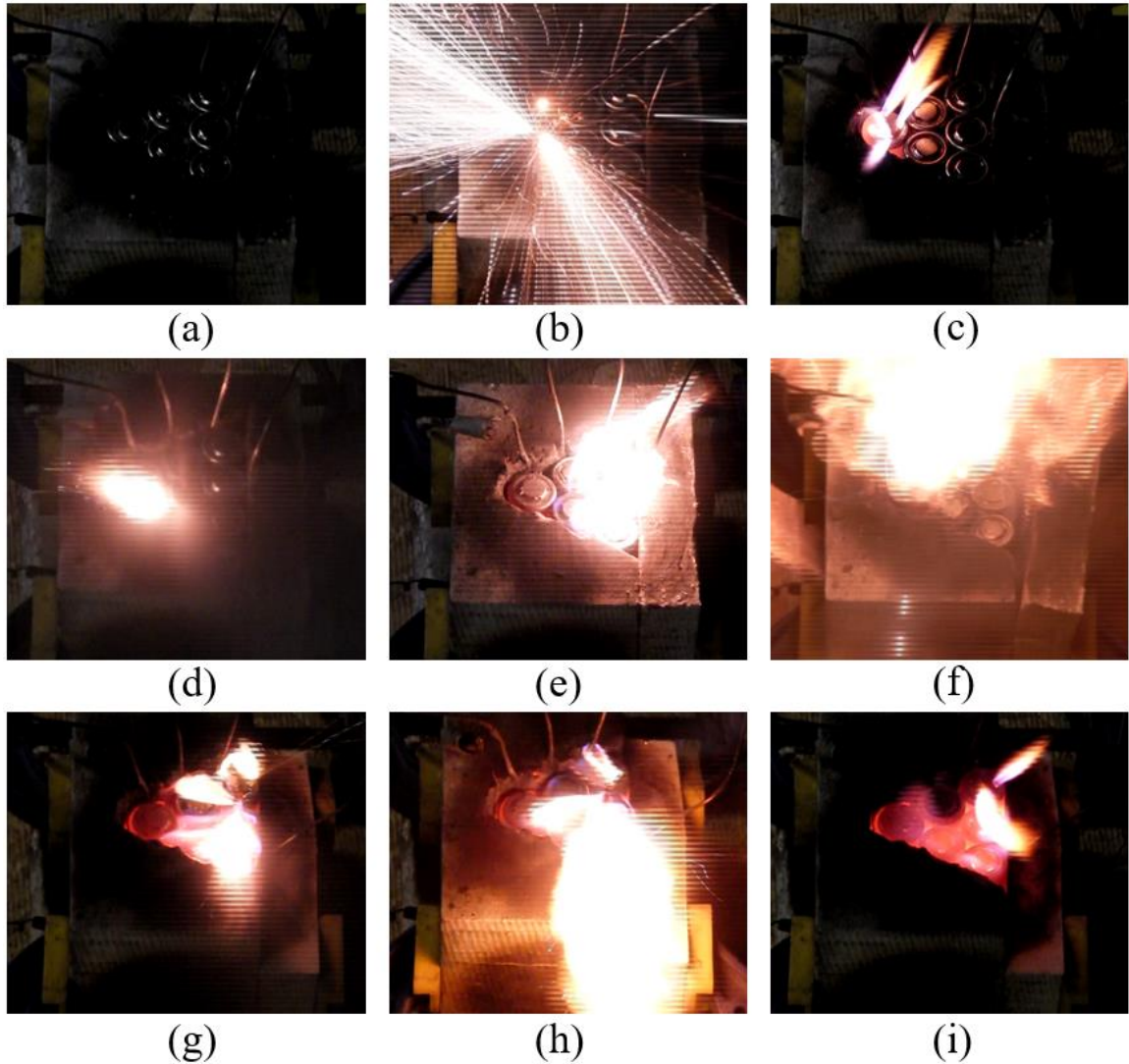


Figure 38. Representative cascading battery failure behaviors, 0 mm spacing test in air. (a) – (c) show thermal runaway of the 1st row LIB, (d) – (f) show thermal runaway of the 2nd row LIBs, (g) – (i) show thermal runaway of the 3rd row LIBs.

The mean values of time to thermal runaway for LIB on each row in the battery pack were obtained from the results of 10 cascading failure tests in each of the three configurations (0 mm spacing test in air, 3 mm spacing test in air, and 0 mm spacing test in nitrogen). These results are presented and compared to each other in Figure 39. The uncertainties of these results are reported as two standard deviations of the mean.

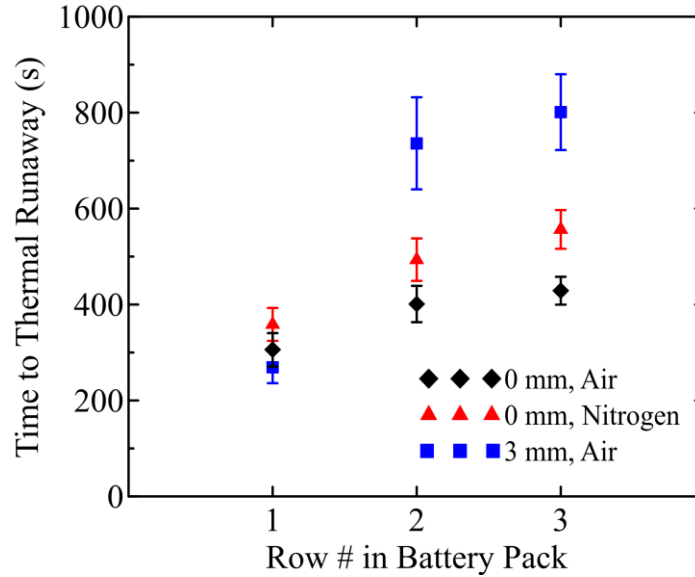


Figure 39. Average onset time of thermal runaway at different rows and the comparisons between different experimental setups in LCO LIB cascading failure tests.

The results for 0 mm spacing test in air are presented by black diamonds, those for 3 mm spacing test in air are presented by blue squares, and those for 0 mm spacing test in nitrogen are presented by red triangles. The onset time of thermal runaway for the 1st row of LIBs was found to be the shortest in 3 mm spacing tests in air, and the other two configurations revealed similar values. On the 2nd row, the onset time of thermal runaway for 3 mm spacing tests in air is about 50% and 85% longer than that for 0 mm spacing tests in nitrogen and 0 mm spacing tests in air, respectively. On the 3rd row, these values are 45% and 85%, respectively. This is because that air is much less thermally conductive compared to LIBs (consisting of steel casing, etc.), air next to the 1st row of

LIB will prevent fast transfer of heat in the battery pack. The influence of low thermal conductivity of air is even more obvious in 2nd and 3rd rows of LIBs. Additionally, in 3 mm spacing test, heat is also transferred largely via the surface to surface radiations in between different LIBs. Compared to heat transfer via conduction (in 0 mm spacing tests), radiation is less efficient and slower, thus causing delayed thermal runaway for LIBs in 2nd and 3rd rows.

On the other hand, the onset time of thermal runaway for 0 mm spacing tests in nitrogen tests is generally longer than that for 0 mm spacing tests in air tests. This is because that, the flaming combustion of vented battery material in nitrogen environment is completely eliminated. The subtraction of this portion of heat, which still exists in tests in air, will delay the battery failure propagation along this battery pack in nitrogen. It should be noted that, in the cascading failure model work presented in Chapter 6, since there is no simulation of external flaming heat onto LIB cells, the simulated results will be compared to 0 mm spacing tests in nitrogen to ensure the consistency of thermal boundary conditions between simulation and experimental results.

Another important observation from all three types of these cascading battery failure tests is that, the battery failure propagation from 2nd row to 3rd row was noticeably faster than that from 1st row to the 2nd row. It was because that, before the 2nd row of LIBs reached runaway point, the 3rd row of LIBs were already pre-heated. This heat accumulated on the 3rd row, with the large amount of additional energy caused by the thermal runaway of 2nd row LIBs, would cause the 3rd row LIBs to reach onset temperature of thermal runaway much faster. It can be expected that, if there were

additional rows of LIBs in the pack, the propagation of battery failure would eventually be out of control at an exponentially growing speed.

Chapter 5: Numerical Modeling for CSBC Validation.

5.1 Model Construction

Beyond the experimental work to understand the thermally-induced failure of LIBs, a numerical model of the CSBC experiments was constructed using the COMSOL Multiphysics software [8], in order to validate the CSBC methodology. The CSBC apparatus was represented by an axisymmetric object as shown in Figure 40. The dimensions of the key object elements were defined to match those of the actual apparatus (Figure 4).

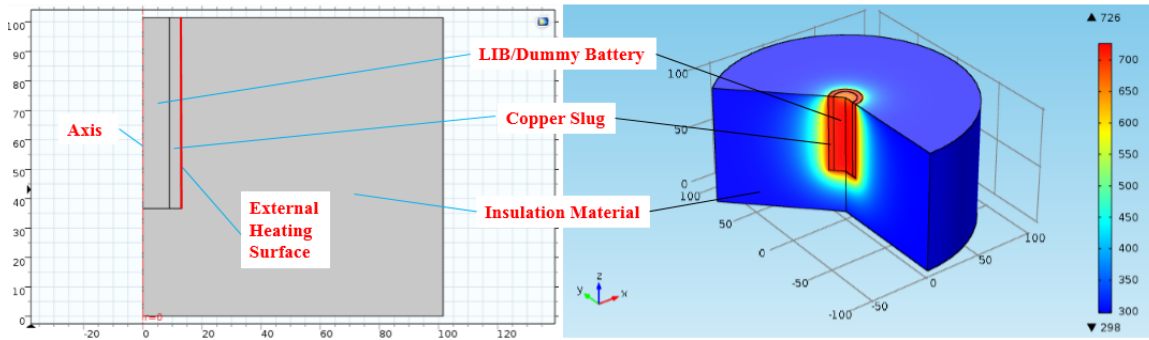


Figure 40. A snapshot of simulated temperature distribution in the CSBC apparatus. The geometric dimensions are in mm; the temperature is in K.

The key equations for heat transfer utilized in COMSOL are:

$$Q = \rho C_p \frac{\partial T}{\partial t} + \nabla \cdot q \quad (4)$$

$$q = -k \nabla T \quad (5)$$

Where ρ is the density (kg m^{-3}), C_p is the heat capacity [$\text{J kg}^{-1} \text{K}^{-1}$], k is the thermal conductivity [$\text{W m}^{-1} \text{K}^{-1}$] and Q is the heat source [W m^{-3}].

To simulate the CSBC experiments by this model, the key parameters are defined as followed: The density, heat capacity and thermal conductivity of all copper elements

were defined using available literature data [13, 15]. The density of the insulation was measured and defined to be 350 kg m^{-3} . The insulation's heat capacity was computed from its known composition, 55 wt.% SiO_2 and 45 wt.% Al_2O_3 , and literature data [13]. The first part of heat source (Q) was the electrical heater of 20 W simulated by distributing the supplied electrical power in a form of heat at the outer surface of the copper slug. In order to validate the P_{IHG} measurements by CSBC, the other part of the heat source in the simulation was prescribed by following the experimentally measured P_{IHG} profiles. Details will be presented in Chapter 5.6. The numerical simulations were conducted using “extremely fine” mesh option (characteristic element size of $\approx 0.6 \text{ mm}$). The default time step was set at 0.2 s. Decreasing or increasing this time step by a factor of 2 did not change the results of the simulations, indicating convergence. It's important to note that, this time step can be automatically reduced in COMSOL to benefit the simulation convergence and accuracy at the points where energy generation rate is high (e.g. the onset of LIB thermal runaway).

The construction of this battery failure model consists of several major steps: 1). The determination of the thermal boundary conditions including radiative and convective heat loss from CSBC to ambient air; 2). The calculation of the thermal conductivity of the insulation material (Gemcolite FG23-112HD ceramic fiber) utilized in CSBC by simulating P_{loss} calibration tests; 3). The evaluation of radial thermal conductivities of the tested LIBs by using test results reported in Chapter 4.3. Details of these steps are described in the following subsections.

5.2 Radiative Heat Loss from CSBC to Ambient Air

The radiative heat loss from CSBC to ambient air in COMSOL is controlled by:

$$q_{rad} = \varepsilon\sigma(T^4 - T_{\infty}^4) \quad (6)$$

where σ is the Stefan-Boltzmann constant and it equals to $5.67 \times 10^{-8} \text{ W m}^{-2} \text{ K}^{-4}$. T_{∞} is the temperature of ambient air. T is the temperature of radiating surface. The emissivity of all the radiating surfaces, ε , needs to be reasonably defined and input into the model in order to simulate accurate radiative heat loss. These surfaces include: the top surface of the copper slug (a ring shape with inner diameter of 18 mm and outer diameter of 26 mm); the circular top surface (in diameter of 18 mm) of copper dummy battery (adopted in power loss calibration tests) or an LIB cell (tested in a standard CSBC test); the top surface, side surface and bottom surface of the thermal insulation material.

The top surface of the copper slug and the top surface of the copper dummy battery/ the top surface of an LIB cell are the surfaces where the temperature were typically brought to a much higher level than the surfaces of thermal insulation material. Due to multiple heating/cooling cycles in CSBC tests, a layer of copper oxide formed on the top surfaces of copper slug and copper dummy battery (used in P_{loss} calibration tests). The emissivity of copper oxide, 0.78 [79], was applied to represent the emissivity of these copper surfaces in CSBC. The emissivity of the insulation was set to be equal to that of ceramic, 0.80 [79] (due to similarity in composition). The LIB surface emissivity was set to be equal to that of partially oxidized steel, 0.50 [79].

5.3 Convective Heat Loss from CSBC to Ambient Air

With the exhaust hood for CSBC on, the air velocity close to the apparatus was measured 0.15-0.20 m s⁻¹, the forced convection was regarded to be minor during the CSBC experiments. It was natural convection that dominated the convective heat loss from CSBC to ambient air, which can be defined in COMSOL by:

$$q_{conv} = h(T - T_{\infty}) \quad (7)$$

where T_{∞} is the temperature of ambient air. T is the temperature of heated surface. A is the area of this surface.

Evaluation of the natural convection coefficient, h , is commonly based on:

$$h = \frac{k}{L} Nu \quad (8)$$

$$Ra = \frac{g(T - T_{\infty})L^3}{T_f \alpha \nu} \quad (9)$$

In equations (8) and (9), Nu is the Nusselt number that can be evaluated empirically for different ranges of Rayleigh numbers, Ra . g is the standard gravity value that equals to 9.8 m s⁻². T_{∞} is the temperature of ambient air. T is the temperature of heated surface. T_f is the film temperature which equals to the average of T_{∞} and T . α is the diffusivity of air, ν is the kinematic viscosity of air and k is the thermal conductivity of air, all of these three properties are evaluated at T_f . L is the characteristic length of the circular surface.

Based on a well-established empirical correlation [80], for an upper surface of a heated plate, $L = 0.9 \times D$ (D is the diameter of the convective circular surface). And Nu can be calculated by the following equations:

$$\begin{cases} Nu = 0.54Ra^{1/4} & 2.0 \times 10^4 < Ra < 8.0 \times 10^6 \\ Nu = 0.15Ra^{1/3} & 8.0 \times 10^6 < Ra < 10^{11} \end{cases} \quad (10)$$

The value of this temperature dependent coefficient, h , was calculated according to Equations (8) to (10) and found to increase from 7.5 to 14.4 $\text{W m}^{-2} \text{K}$ with temperature increasing from 298 to 800 K. Detailed temperature dependent coefficient profile is shown in Figure 41. In the model, the ambient temperature was always maintained at 298 K.

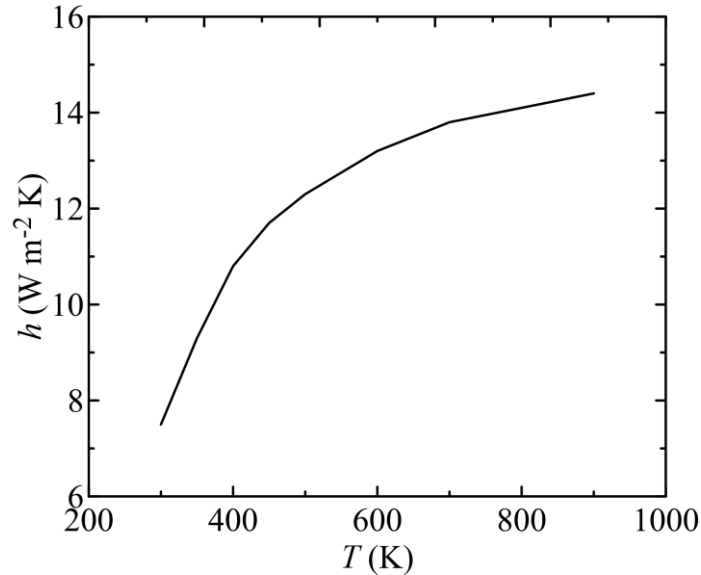


Figure 41. Temperature dependent natural convection coefficient utilized in COMSOL simulation.

This convective coefficient was applied to all side surfaces of insulation material in the battery failure model and it was found to have minor impact in the temperature predictions, because of relatively low temperature on these surfaces throughout the simulation. Thus the same temperature dependent convective heat loss coefficient as indicated in Figure 41 was applied to all surfaces of CSBC for simplicity of the model construction.

5.4 Thermal Conductivity of the Insulation Material

With the boundary conditions defined, the numerical model, at this point, can be utilized to determine the thermal conductivity of the insulation material. The insulation

material, Gemcolite FG23-112HD ceramic fiber, was adopted in CSBC to minimize heat losses from the system to the environment. It consists of 55% of SiO₂ and 45% of Al₂O₃ by mass, the thermal conductivity of which was not clearly defined. Its evaluation was based on the simulations of the P_{loss} calibration tests (Chapter 2.3 and 3.2). In these simulations, the electrical heater was simulated by distributing the supplied electrical power (20 W, 40 W, 60 W, 80 W and 100 W for P_{loss} calibration tests) in a form of heat at the outer surface of the copper slug. Thermal boundary conditions and thermal properties of material in the model are all defined, except for the thermal conductivity of insulation material. Initial temperature-dependent thermal conductivity profile for insulation material was guessed and the slug temperature was simulated and compared to experimental measurements at all five heating rates. The thermal conductivity of insulation material should be adjusted to a higher value when the slug temperature was over-predicted, and vice versa. This profile was being modified till the point where the simulated slug temperature histories and the experimental measurements of temperatures had relative differences of within $\pm 5\%$ for power loss calibration tests conducted at all five heating rates.

It was found that the thermal conductivity that increases from 0.065 to 0.143 W m⁻¹ K⁻¹ with temperature increasing from 298 to 800 K provided a good agreement (within 5% in K) between all simulated and experimental data. This temperature dependent thermal conductivity of the insulation material profile is shown in Figure 42, with the copper slug temperature fittings. The thermal conductivity of the insulation material increased noticeably faster at lower temperature range, this phenomena was likely to be caused by the thermal expansion of insulation at this temperature range

quickly reducing thermal contact resistance between the insulation and the slug. This thermal conductivity profile of insulation material was regarded to be representative and it continued to be utilized in the next steps of simulation work. This exercise was conducted regularly for each single specific set of power loss calibration tests to take into account the potential change of thermal conductivity of insulation material with time, but it was found that this change was minor.

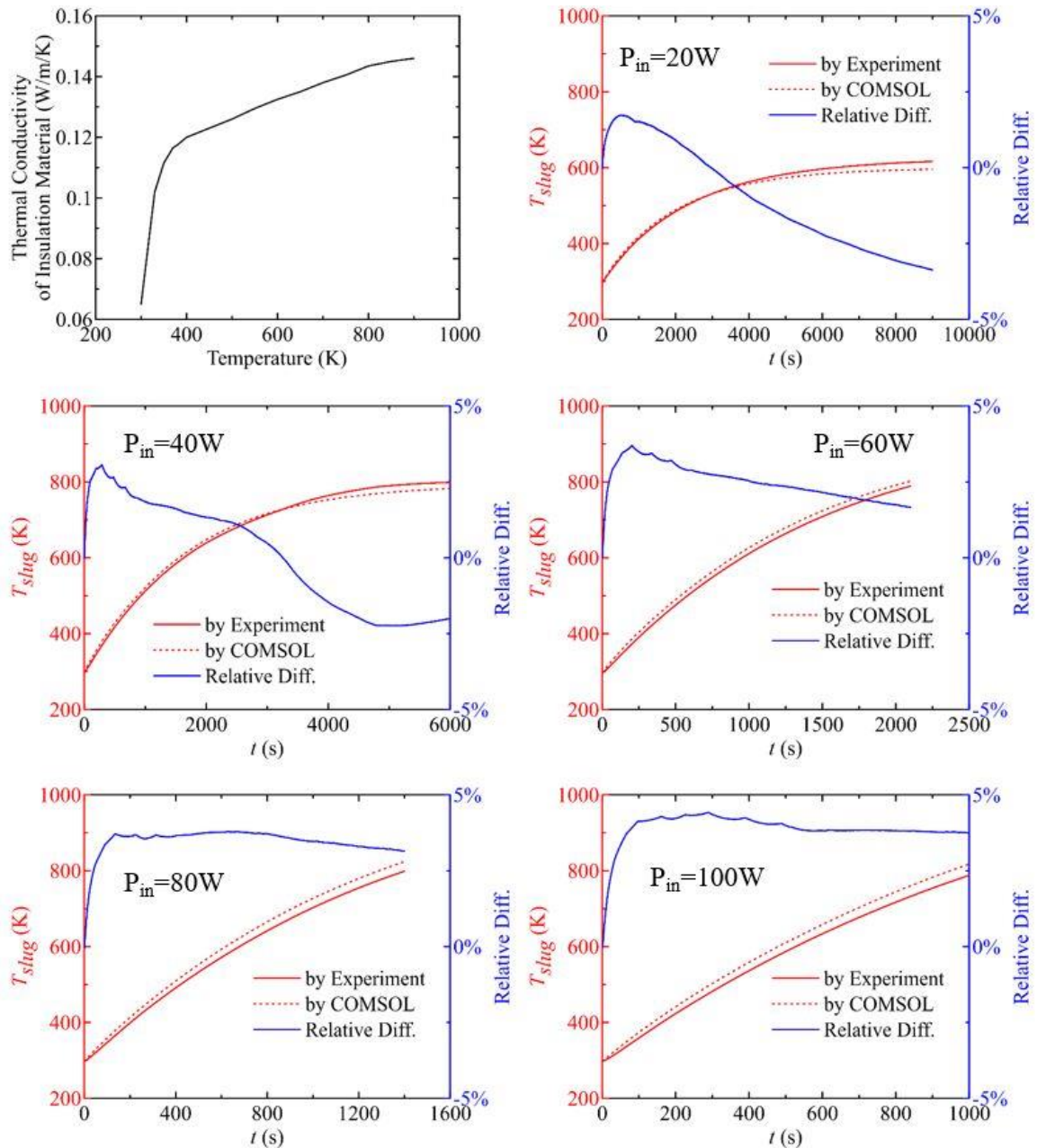


Figure 42. COMSOL simulations of power loss calibration tests for determination of thermal conductivity of insulation material.

5.5 Radial Thermal Conductivity of LIB Cells.

The radial thermal conductivity of the LIB cells were determined using the inverse modeling approach that is similar to what was utilized for the determination of thermal conductivity of insulation material, and based on the experimental data obtained from tests described in Chapter 2.5 (test results reported in Chapter 4.3). To simulate

these tests, P_{in} of 20 W was input in the model and the temperature histories at both copper slug and battery's axis were computed. This simulation required the model to be configured with all the previously determined thermal boundary conditions and thermal properties of materials, the only undefined property in the model, at this point, was the radial thermal conductivity of the battery.

The value of thermal conductivity of an LIB cell was initially guessed then the temperatures at both locations were simulated and compared to experimental measurements. This value needed to be dialed down when the simulated temperature at battery's axis was over-predicted, and vice versa. Once the simulated temperature histories reached good agreements (within $\pm 3\%$) with the temperatures collected experimentally, the corresponding thermal conductivity of the battery was regarded as representative. Figure 43 shows the results when thermal conductivity of battery was adjusted to 1.0 ± 0.1 , 0.4 ± 0.1 and 0.4 ± 0.1 W m⁻¹ K⁻¹ for LCO, NMC and LFP cells, respectively. These values will continue to be utilized in the following numerical modeling of CSBC tests.

While these cells were represented in the model as isotropic objects, the experimental design emphasizes radial thermal conduction. Therefore, these conductivity values should be associated with radial direction. A cylindrical battery cell typically has a “jelly-roll-like” layered structure as illustrated in Figure 1. With the conduction heat transfer principle in cylindrical structure [74] and the detailed thermal conductivity information for each layer of component in a typical battery [81], the thermal conductivity can be calculated 0.7 W m⁻¹ K⁻¹, which indicates that the results determined in this study are reasonable.

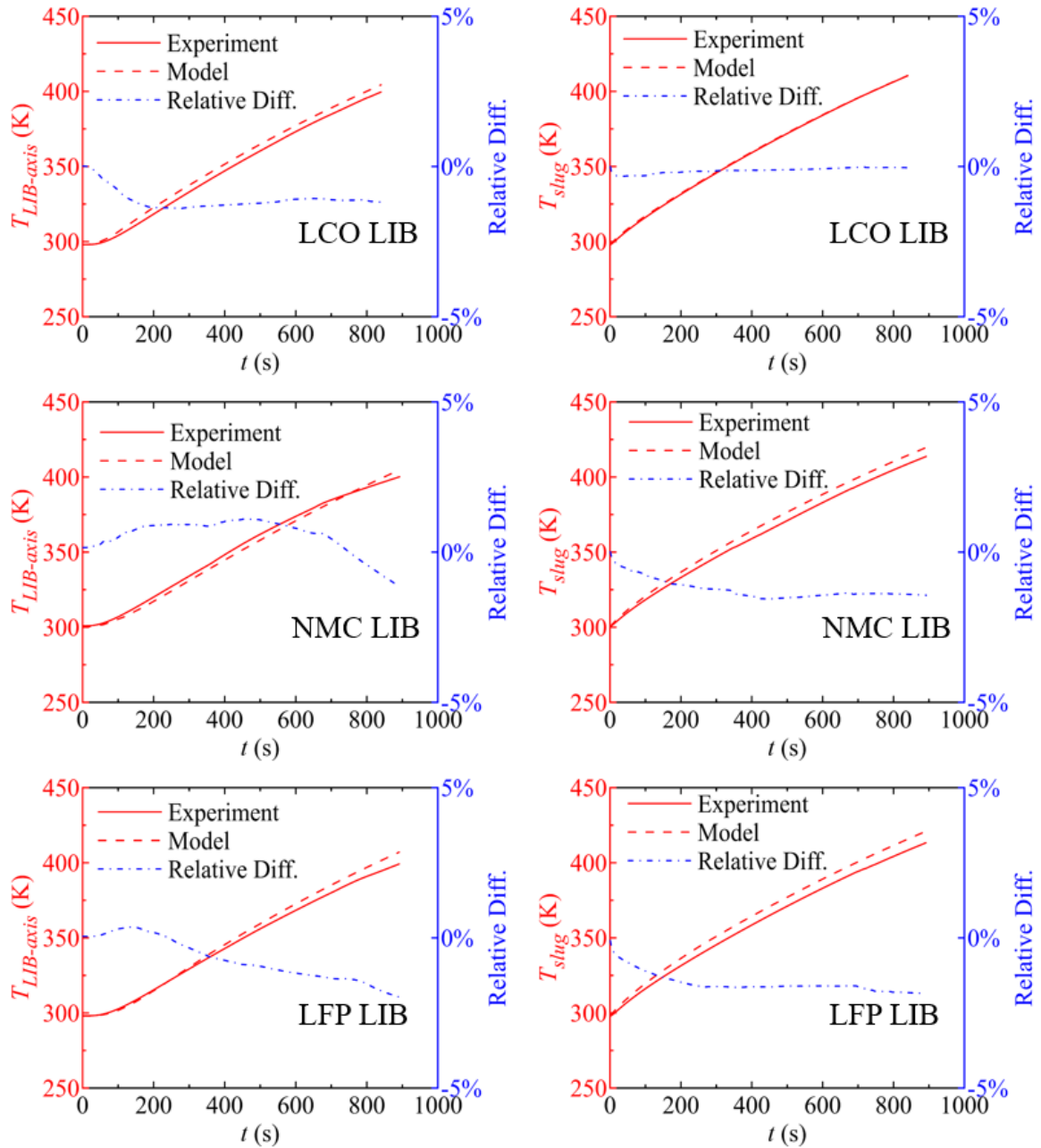


Figure 43. COMSOL simulation results to determine radial thermal conductivity of LIBs.

5.6 Validation of Internal Heat Generation Measurements by CSBC

It is important to note that the CSBC experimental measurements of the internal heat generation by LIBs rely on two key assumptions: 1). The lumped heat capacity assumption [74] for an LIB cell, meaning that the temperature inside the battery was

assumed to be spatially uniform and it was equal to the copper slug temperature; and 2). The power loss can be accurately determined via empirical calibration tests (Chapter 2.3 and 3.2). This evaluation would be inaccurate if either of these assumptions is not reasonable. Thus it is critical to validate the experimental results against the numerical model for battery failure, where the detailed heat transfer dynamics is taken into consideration.

Using the well-defined thermal boundary conditions and all material's thermal transport properties in CSBC, a validation of the experimentally determined P_{IHG} profiles was carried out by performing simulations where these profiles were prescribed as a piecewise-linear volumetric heat generation function and applied to the LIB volume as a part of Q in Equation (4). To be more specific, 12 critical points were determined along the experimental measurements of P_{IHG} profiles to represent important transitions such as: the beginning of heat release before the onset of safety venting, the onset of safety venting, the onset of thermal runaway, the peak(s) in heat release rates, etc. These points were lined up with linear interpolations to simulate the internal generation rates in the model. It's important to note that the areas under the prescribed internal heat generation rates and those under the experimental measurements were identical for all the simulated cases, this will ensure that the total amount of energy produced by an LIB in simulation and that measured experimentally were the same.

The simulated slug temperatures were compared to the experimental data. In these simulations, the LIB density was defined as a function of time, which was calculated from the corresponding linearly interpolated experimental m_{LIB} data. One representative battery test from each battery type at each SOC was selected for this validation practice.

Each representative battery test had the peak internal heat generation as well as the integral heat generation to be closest to the average value (over ten tests for each battery type at each SOC).

The results of the experimentally derived P_{IHG} profile verification exercises are shown from Figure 44 to Figure 46. The P_{IHG} profiles implemented in the simulations are shown next to the experimental data in the graphs on the left. A comparison of the T_{slug} computed using the P_{IHG} profiles as an input to the corresponding experimental data is shown in the graphs on the right. The simulated temperatures are within 5% of the experimental data for all LIB types and SOC levels, which indicates that the lumped heat capacity assumption invoked in the analysis of the CSBC experiments is reasonable.

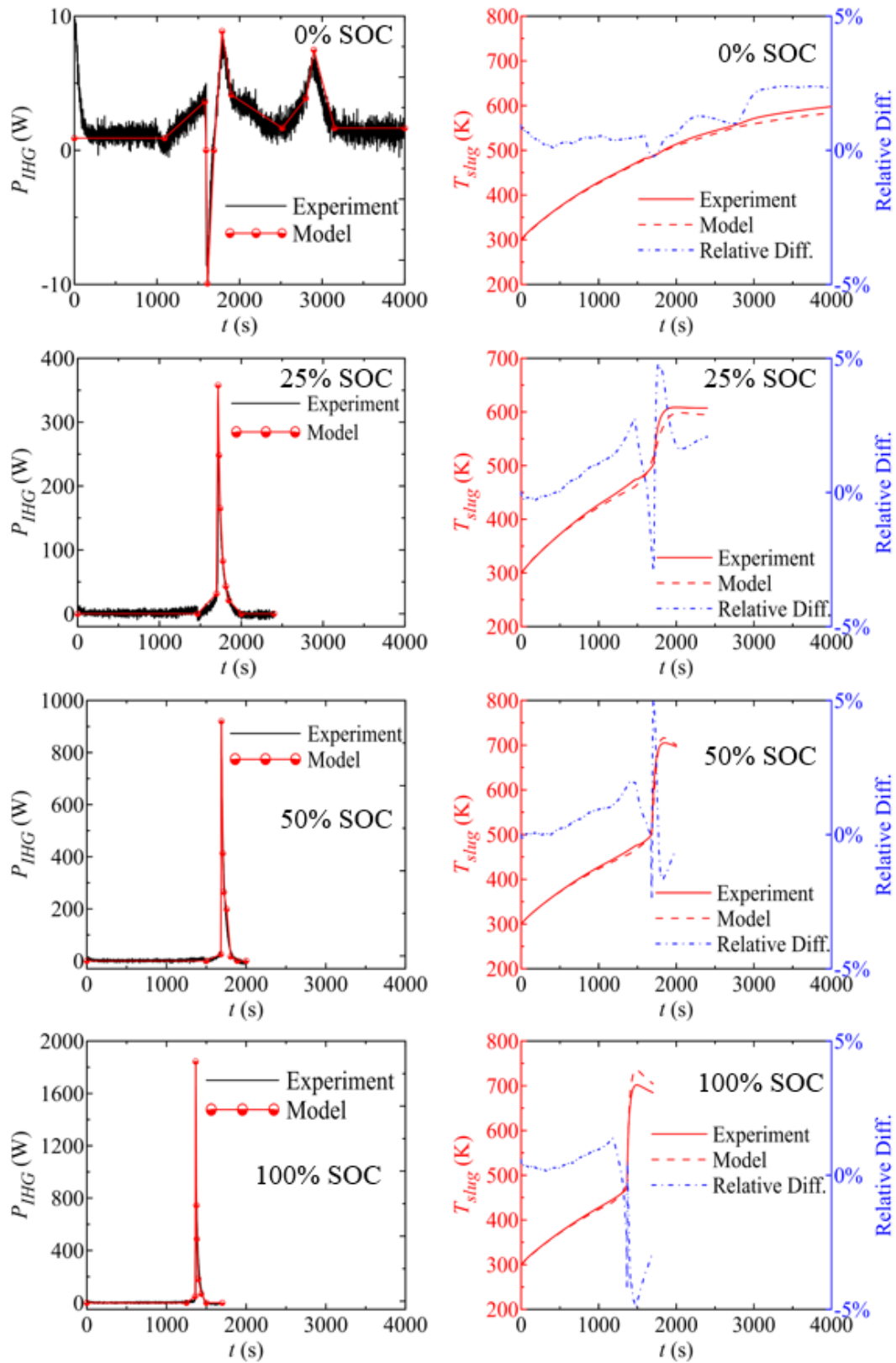


Figure 44. Results of numerical modeling of the CSBC experiments performed for LCO LIB cells. P_{IHG} is prescribed; T_{slug} is simulated and compared with the experimental data.

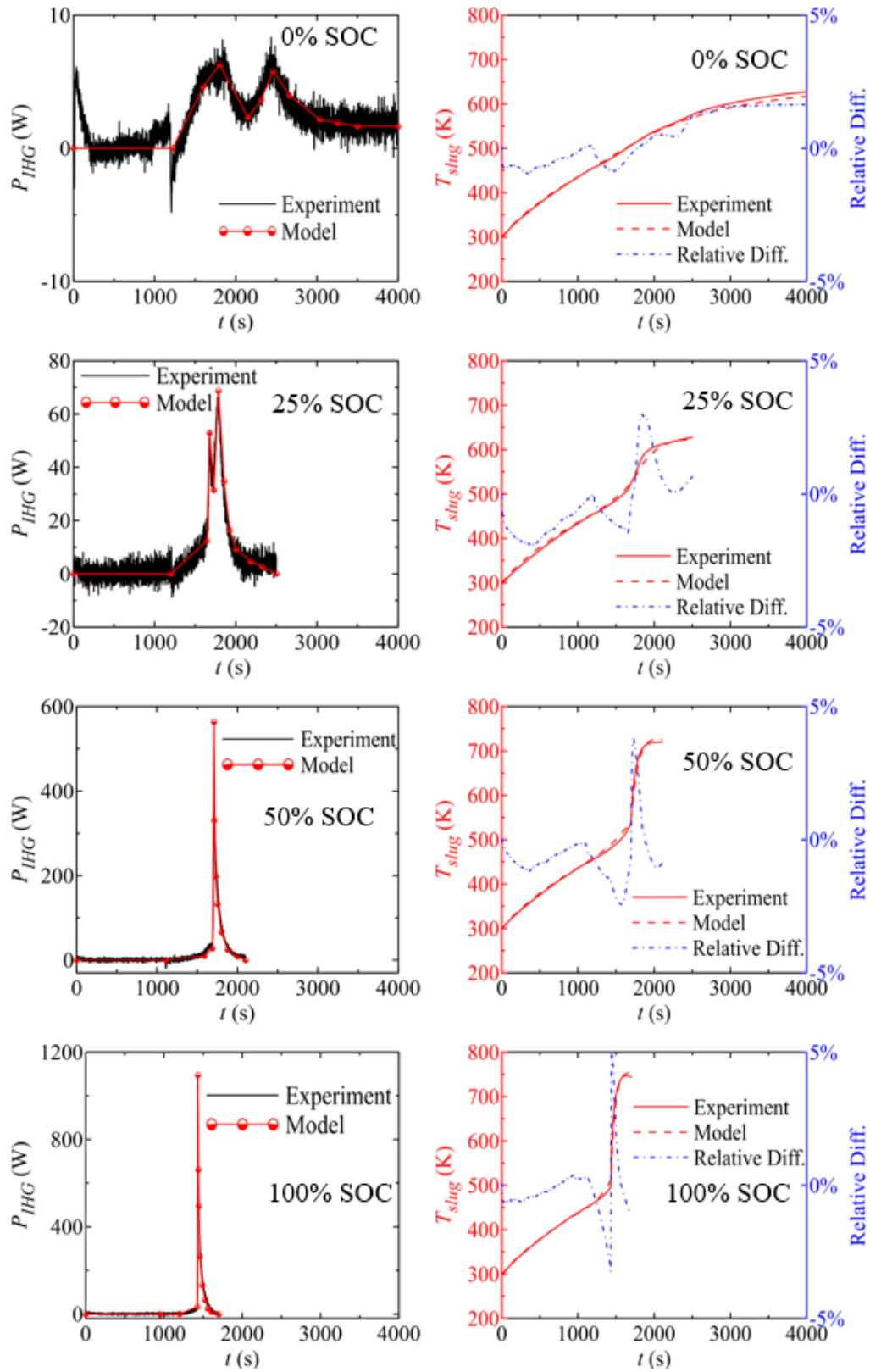


Figure 45. Results of numerical modeling of the CSBC experiments performed for NMC LIB cells. P_{IHG} is prescribed; T_{slug} is simulated and compared with the experimental data.

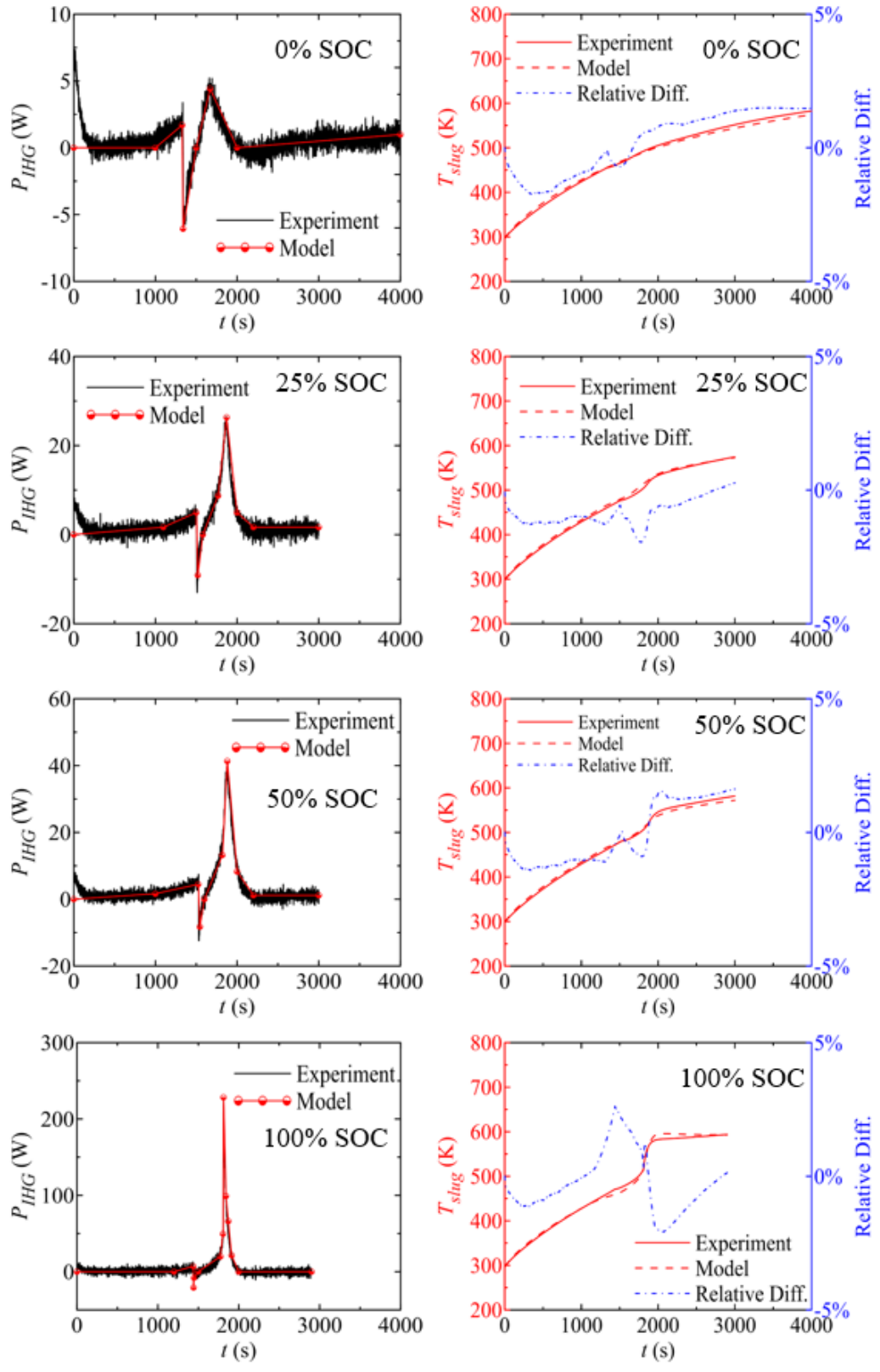


Figure 46. Results of numerical modeling of the CSBC experiments performed for LFP LIB cells. P_{IHG} is prescribed; T_{slug} is simulated and compared with the experimental data.

Chapter 6: Thermo-Kinetic Modeling of Battery Thermal Failure.

6.1 Modeling Methodology

The numerical modeling described in Chapter 5 has showed good validation capabilities for standard CSBC experiments, demonstrating that CSBC technique had given adequately accurate quantitative evaluations of thermally-induced failure of LIBs. However, this model was largely relied on inputs, such as the mass loss rates and prescribed P_{IHG} profiles, which were dependent on time and specific to experimental data from a standard CSBC test. This model is unlikely to be extended to a more general thermally inducing scenarios since it is reasonable to regard the energy release by a failing battery as a consequence of tens of or even hundreds of chemical reactions taking place in the battery casing. These chemical reactions are typically dependent on both time and temperature. Efforts were then taken in current study towards the development of a thermo-kinetic model of battery thermal failure. In this model, the heat release rates during battery failure were hypothesized to be able to be presented by an effective exothermic chemical reaction. The configurations of this model was relied on the data provided by standard CSBC experiments. Once developed, this model can be utilized in more complex scenarios beyond the standard CSBC tests.

Initially, this model was constructed and parameterized utilizing a well-established methodology – reverse modeling based on Arrhenius' Law [82], and the standard CSBC test results. Simulations of the standard CSBC tests were carried out. These simulations were used to determine a set of parameters to effectively describe the exothermic chemical reactions for each tested SOC (0%, 25%, 50% and 100%), that was

intended to mathematically mimic the experimental T_{slug} histories. No attempt was made to identify the actual chemical species involved in the heat generation during the battery thermal failure. Efforts were also taken to keep the dependencies of all of these parameters on the SOC of LIB cell to be no more complex than third-order polynomial. This construction and parameterization procedure is specifically demonstrated on LCO LIB cells (T-Energy ICR18650).

Subsequently, to validate the formulated reaction mechanism and reaction parameters, this developed model was utilized to simulate non-standard CSBC tests including 1). LCO LIB cells at 100% SOC heated by 20 W, 40 W, 60 W, 80 W and 100 W in CSBC, respectively; and 2). LCO LIB cells at 75% SOC heated by 20 W in CSBC. It's important to note that these particular experiments were not utilized in the model parameterization process. This validation exercise was to test whether the thermo-kinetic battery failure model was reasonably parameterized.

Finally, after the model is validated, it's applied to predict battery thermal failure behaviors in a more complex scenarios – cascading battery failure, which experimental results were presented in Chapter 4.7. The simulated time to thermal runaway of each LIB in the pack will be compared to the experimental data.

6.2 Thermo-Kinetic Battery Failure Model Construction and Parameterization

Similar to the model described in Chapter 5, the CSBC apparatus was represented by an axisymmetric object (Figure 40) with the dimensions of the key object elements defined to match those of the actual apparatus (Figure 4). Following material properties were set to be the same as the previous model: the density, heat capacity and thermal conductivity of all copper elements; the density, heat capacity and temperature dependent

thermal conductivity (Figure 42) of thermal insulation material; the heat capacity and radial thermal conductivity (Figure 43) of simulated LIB cell. The thermal boundary conditions – radiative heat loss (Chapter 5.2) and the temperature dependent natural convection coefficient (Figure 41) – were also set to be identical to the previous model. The electrical heater was also simulated by distributing the supplied electrical power in a form of heat flux at the outer surface of the copper slug. The meshing was also set to “extremely fine” option with characteristic element size of about 0.6 mm.

The key changes in this model are: the energy release and the density change (mass change) of a failing LIB cell.

Instead of using experimentally determined P_{IHG} profiles, the energy release by a failing LIB in this model is represented by an exothermic chemical reaction in COMSOL:



In this reaction, LIB_r represents the “reactant” and LIB_p represents the “product” of this reaction. This reaction is governed by Arrhenius’ Law in COMSOL:

$$r = \frac{m_r}{V} \times A \left(\frac{T}{T_{ref}} \right)^n e^{-E_a/(RT)} \quad (12)$$

More specifically, in Equation (12), the reaction rate of reaction (11) is given as r [$\text{g m}^{-3} \text{s}^{-1}$], T_{ref} is equal to 1 K, R is the ideal gas constant ($8.314 \text{ J mol}^{-1} \text{ K}^{-1}$). The activation energy (E_a [J mol^{-1}]), pre-exponential factor ($A \left(\frac{T}{T_{ref}} \right)^n$ [s^{-1}]) must be defined for each reaction. The reaction rate, r , is therefore a function of temperature (T) and the concentration of LIB_r : $\frac{m_r}{V}$ [g m^{-3}].

In addition, the dynamic density of LIB in the model, ρ_{LIB} , was taken into consideration by associating it with the dynamic concentration of LIB_r : $\frac{m_r}{V}$, with the following correlation:

$$\rho_{LIB} = \frac{m_r}{V} + \rho_{LIB_final} \quad (13)$$

In Equation (13), ρ_{LIB} is the dynamic density utilized in this model. ρ_{LIB_final} is the final density of a simulated LIB cell after the failure, which value was measured in the experiments and was approximately constant for each tested SOC. $\frac{m_r}{V}$ is the dynamic concentration of LIB_r , with an initial value of $(\frac{m_r}{V})_{initial}$. The value of $(\frac{m_r}{V})_{initial}$ is set to be equal to the density changes of a simulated LIB before and after its failure.

For LCO LIB samples that are demonstrated in this model construction, the initial ρ_{LIB} before the battery failure is 2661.5 g m^{-3} . The values of ρ_{LIB_final} and $(\frac{m_r}{V})_{initial}$, and the specific expressions of ρ_{LIB} are summarized in Table 10 for all tested SOCs.

Table 10. Settings of dynamic LCO LIB density utilized in thermo-kinetic battery failure model.

SOC (%)	ρ_{LIB} initial [kg m ⁻³]	ρ_{LIB_final} [kg m ⁻³]	$(\frac{m_r}{V})_{initial}$ [kg m ⁻³]	ρ_{LIB} in model per Equation (13) [kg m ⁻³]
0	2661.5	2389.3	272.2	$\frac{m_r}{V} + 2389.3$
25	2661.5	2377.2	284.3	$\frac{m_r}{V} + 2377.2$
50	2661.5	2256.2	405.3	$\frac{m_r}{V} + 2256.2$
100	2661.5	1693.7	967.8	$\frac{m_r}{V} + 1693.7$

This setting of simulated LIB's density in this model can ensure that: with the consumption (decrease in concentration, $\frac{m_r}{V}$) of LIB_r , the ρ_{LIB} will also decrease eventually to value of ρ_{LIB_final} . The impact of density change of LIB on the heat transfer mechanism in the model thus can be taken into account. In addition, the decreasing rate of the LIB density will be directly proportional to the reaction rate at a certain point (higher reaction rate results in faster LIB density change during failure). This correlation is considered to better represent the experimental observations.

The heat source term (Q) in equation (4) consist of two parts in this model: the 20 W external heating at the copper slug surface P_{in} and the rate of energy produced by reaction (11) - $P_{reaction}$ [W m⁻³]. $P_{reaction}$ in COMSOL was defined by:

$$P_{reaction} = -r * h_r \quad (14)$$

The value of h_r (heat of reaction, [J kg⁻¹]) was initially calculated by:

$$h_r = -\frac{P_{IHG} \text{ integral}}{(m_r)_{initial}} \quad (15)$$

Where P_{IHG} integrals are reported in Table 8, which represents the total heat production by an LIB cell during failure. $(m_r)_{initial}$ represents the total mass of LIB_r , which can be calculated by multiplying the initial concentration reactant ($(\frac{m_r}{V})_{initial}$) with the volume of the LIB cells ($1.65 \times 10^{-5} \text{ m}^3$).

At this point, this model is ready to be further parameterized utilizing a widely adopted methodology – reverse modeling based on Arrhenius' Law, which has been demonstrated in many previous studies to be a powerful methodology to represent the temperature-dependent chemical kinetics empirically [72, 83]. In particular, Arrhenius parameters describing the battery failure reaction (A , n and E_a) for each SOC were obtained through refinement exercises performed using COMSOL: these parameters for each SOC were changed in small increments; the simulated T_{slug} were compared with the experimental T_{slug} curves. The modifications of heat of reaction h_r were needed for better fitting results, but were managed to be controlled within $\pm 15\%$ of the initial h_r value calculated by Equation (15). This ensured that the total energy defined in the model was comparable to the value measured experimentally. Efforts were also taken to keep the dependencies of all of these Arrhenius parameters on the SOC of LIB cell to be no more complex than third-order polynomial.

In the first round of model parameterization, for simplicity, n was kept to be equal to 1 for all SOC. A and E_a were kept being modified to the point where the best agreement can be achieved as shown in Figure 47.

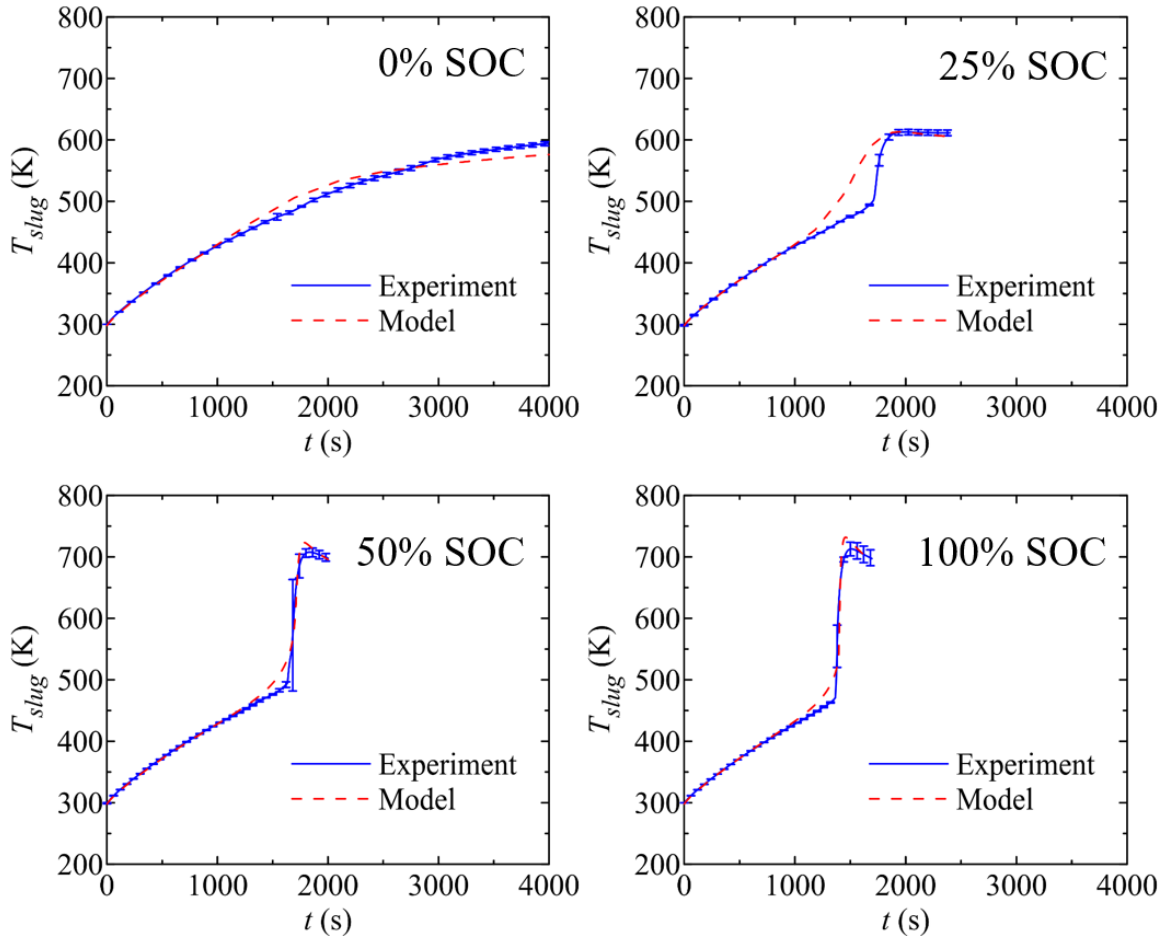


Figure 47. Results of thermo-kinetic model ($n=1$) of the tested LIB cell's thermal failure observed in CSBC tests ($P_{in}=20$ W), T_{slug} is simulated and compared with the experimental data.

Although agreements for 0%, 50% and 100% SOC were found satisfactory, the one for 25% SOC case didn't produce good agreement (despite the good prediction of plateau temperature). For example, at the onset of the thermal runaway for 25% SOC, the sharp rise in T_{slug} curve was not well simulated.

To improve the overall quality of this model, second round of model parameterization was conducted with n as a parameter changing with SOCs. All three parameters (A , n and E_a) were refined in the fitting process until the relative differences between the experimental and simulated T_{slug} profiles are within 2% on average for all the SOCs. With the finalized parameters listed in Table 11, the second round of model parameterization was finished. The quality of the agreements between the experimental and predicted curves are shown in Figure 48.

Table 11. Finalized Arrhenius parameter for the thermo-kinetic model of battery failure

SOC	Initial h_r per Equation (15) (J kg ⁻¹)	Finalized h_r (J kg ⁻¹)	A (s ⁻¹)	E_a (J mol ⁻¹)	n
0%	-1.89×10^6	-1.89×10^6	0.1	6.10×10^4	1.6
25%	-5.02×10^6	-4.45×10^6	0.2	6.08×10^4	1.5
50%	-5.58×10^6	-4.70×10^6	0.3	5.85×10^4	1.3
100%	-2.33×10^6	-2.20×10^6	0.5	5.30×10^4	1.1

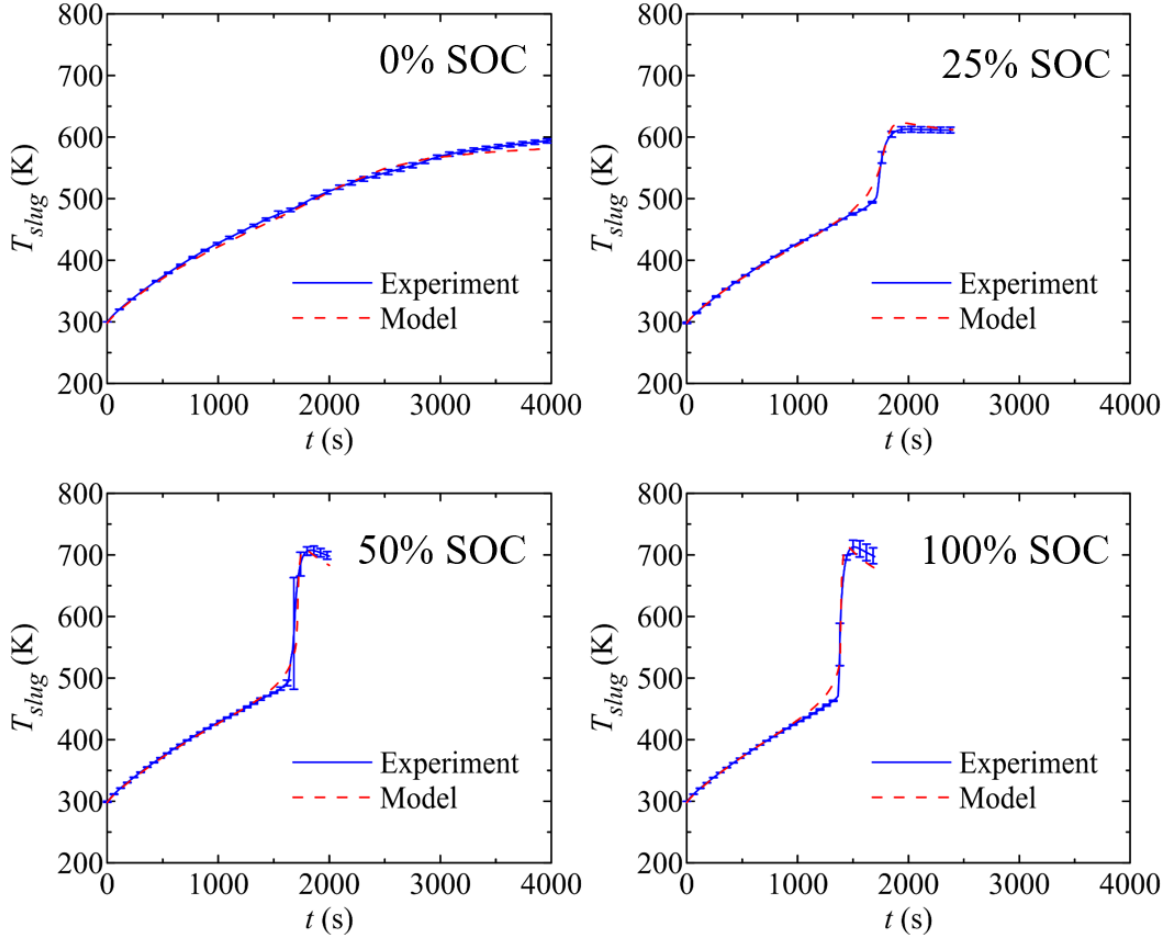


Figure 48. Results of thermo-kinetic model ($n \neq 1$) of the tested LIB cell's thermal failure observed in CSBC tests ($P_{in} = 20$ W), T_{slug} is simulated and compared with the experimental data.

The average deviation between the experimental and predicted T_{slug} curves turned out to be below 1.5% for all the four SOC's, and all the important patterns (such as sharp rise of T_{slug} at onset of thermal runaway) were fairly well simulated. Thus this second round of model parameterization was considered to be adequate and final.

The dependencies of all the Arrhenius parameters are expressed by the following equations:

$$\left(\frac{m_r}{V}\right)_{initial} = 859.9 \times SOC^2 - 164.1 \times SOC + 272.0 \quad [\text{kg m}^{-3}] \quad (16)$$

$$h_r = -1.0 \times 10^7 \times SOC^3 + 2.6 \times 10^7 \times SOC^2 - 1.6 \times 10^7 \times SOC - 1.9 \times 10^6 \quad [\text{J kg}^{-1}] \quad (17)$$

$$A = 0.4 \times SOC + 0.1 \quad [\text{s}^{-1}] \quad (18)$$

$$E_a = 1.4 \times 10^4 \times SOC^3 - 2.8 \times 10^4 \times SOC^2 + 5.2 \times 10^3 \times SOC + 6.1 \times 10^4 \quad [\text{J mol}^{-1}] \quad (19)$$

$$n = 0.1 \times SOC^2 - 0.6 \times SOC + 1.6 \quad (20)$$

In Equations (16) to (20), the SOC equals to 0 for 0% SOC, 0.25 for 25% SOC, etc.

6.3 Thermo-Kinetic Battery Failure Model Validation

6.3.1 LCO LIB at 100% SOC heated by P_{in} of higher than 20 W

The fully parameterized thermo-kinetic battery failure model was then validated against CSBC tests on 100% SOC LCO LIBs with (P_{in}) ranging from 40 W to 100 W with an increment of 20 W. In the model, all of the model parameters were kept the same as in the standard CSBC test simulation, except for P_{in} changed to 40 W, 60 W, 80 W and 100 W, respectively. In Figure 49, the T_{slug} curves predicted by this model (red dashed lines) for these tests are compared with the experimental T_{slug} data (blue solid lines) collected by CSBC.

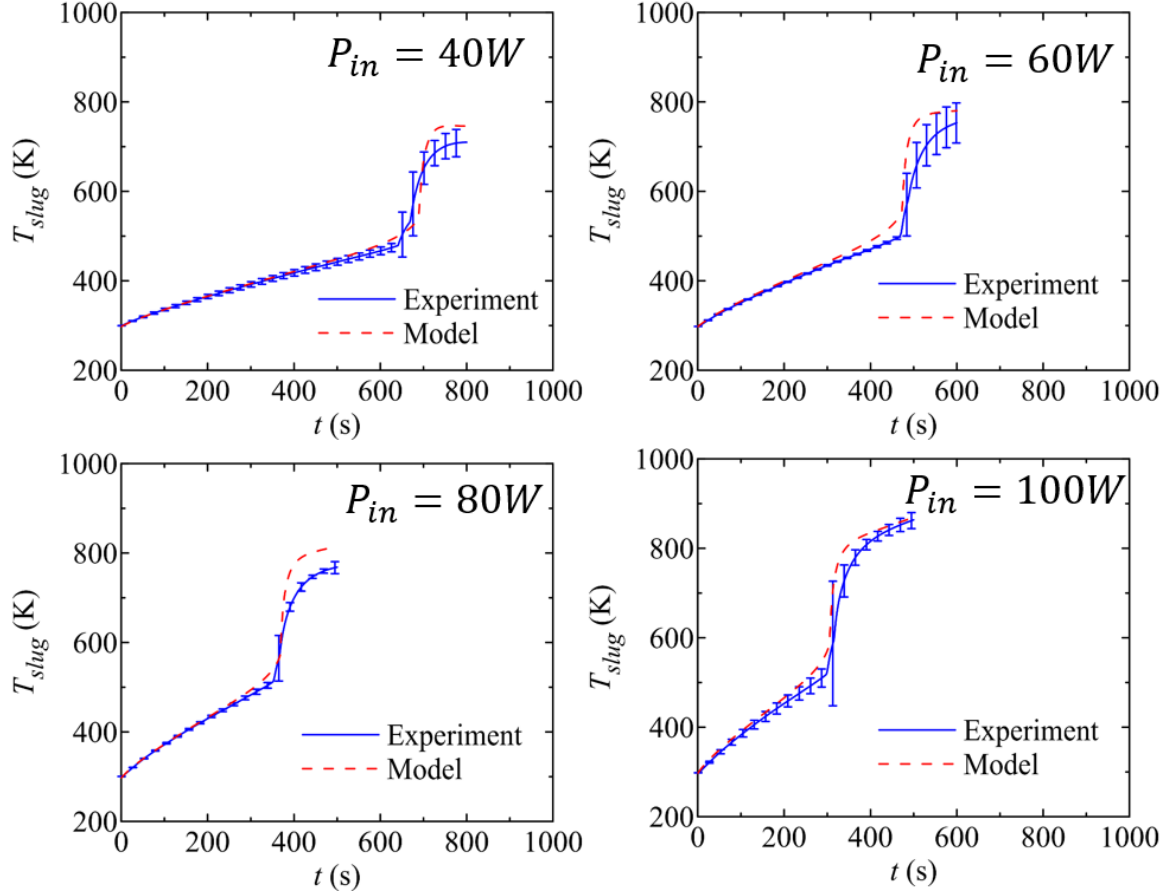


Figure 49. Results of thermo-kinetic model of the tested 100% SOC LIB cell’s thermal failure observed in CSBC tests (P_{in} ranging from 40 W to 100 W), T_{slug} is simulated and compared with the experimental data.

The simulated T_{slug} profiles show similar structure of a sharp increase at the onset of thermal runaway, and the peak value of T_{slug} were all with good agreements if compared with the experimental data. The average different between the experimental and predicted T_{slug} curves was found to be below 5% for all the four heating rates.

The onset time of thermal runaway in the simulations were defined to be the point where the temperature increasing rate ($\frac{dT_{slug}}{dt}$) was higher than 1 K s^{-1} (typical values observed in the experimental measurements when thermal runaway took place). Figure

50 shows the relationship between the onset time of thermal runaway and P_{in} for both experiments (shown as red triangles with error bars) and simulations (shown as blue crosses). Excellent agreements were found.

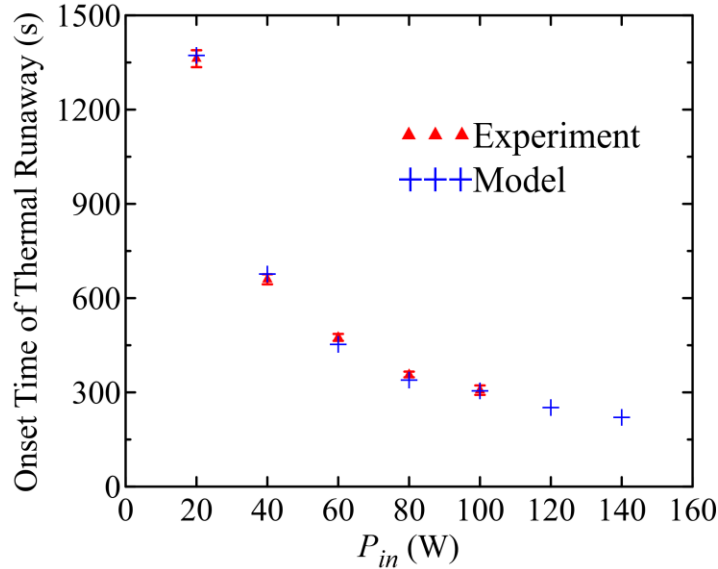


Figure 50. Relations between the heating rate P_{in} and the onset time of thermal runaway for LCO LIBs at 100% SOC, with comparisons to simulated data.

Additionally, simulations were conducted where the P_{in} was set to be 120 W and 140 W, respectively. The onset time of thermal runaway in these simulations are also included in Figure 50 as blue crosses. These results demonstrate how the model can be used to predict LIB failure behavior outside the range of conditions that can be realized in the current experiments.

6.3.2 LCO LIB at 75% SOC heated by P_{in} of 20 W

To further examine the generality of this thermo-kinetic model over a range of the SOC of an LIB cell, Arrhenius parameters for an LIB cell at 75% SOC was calculated by Equations (16) to (20) (with the value of SOC being 0.75). These parameters were input

in model and the P_{in} was set to be 20 W. The simulated T_{slug} profile for this case is compared with the experimental data (average of 3 tests) in Figure 51. Excellent agreement was achieved.

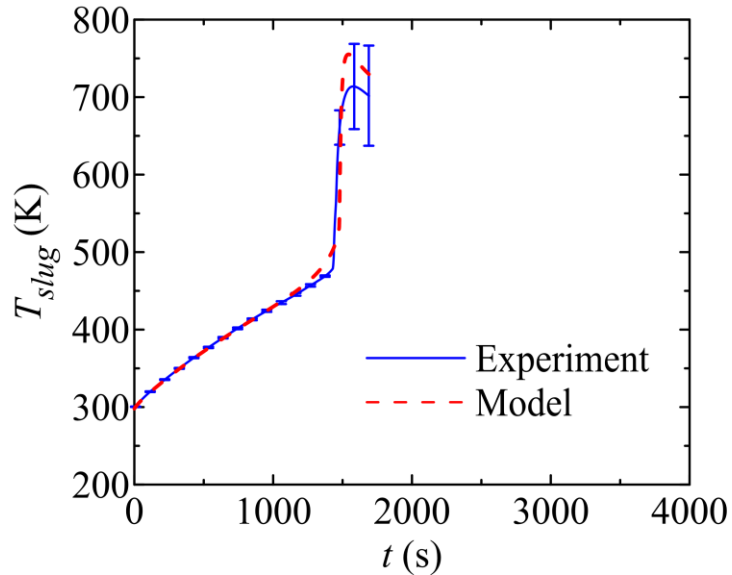


Figure 51. Results of thermo-kinetic model of the tested 75% SOC LIB cell’s thermal failure observed in CSBC tests ($P_{in}=20$ W), T_{slug} is simulated and compared with the experimental data.

This excellent agreements indicate that the thermo-kinetic model of battery thermal failure is well constructed and parameterized. This model has proved that the just-defined set of parameters was sufficient enough to effectively describe the battery failure of the LIB sample at all different SOC. The model parameters were all dependent on the SOC of the LIB cell. Moreover, the model didn’t require inputs describing battery structure or detailed battery component properties.

6.4 Application of Thermo-Kinetic Battery Failure Model in Cascading Battery Failure

6.4.1 Cascading battery failure model construction.

The fully parameterized thermo-kinetic battery failure model was then applied in COMSOL to simulate the cascading battery failure experiments, in order to test the extrapolation power of this model into more complex battery thermal failure scenarios. More specifically, the cascading battery failure test setup was constructed in COMSOL as a three dimensional model. The dimensions of the all the key elements were well defined to match those in the actual experimental setup (Figure 8).

The key thermal parameters were defined as followed: The density, thermal conductivity and heat capacity of the insulation material (Kaowool PM) were defined using previous studies' data [70-73]. The density of Kaowool PM is 256 kg m^{-3} ., the thermal conductivity of it is $0.052 \text{ W m}^{-1} \text{ K}^{-1}$, and the heat capacity of it is $1.07 \text{ J g}^{-1} \text{ K}^{-1}$. The heat capacity of the simulated LCO LIBs is $1.1 \text{ J g}^{-1} \text{ K}^{-1}$ as defined in Chapter 3.3 in current study. The thermal conductivity of these LIBs is initially set to be and $1.0 \text{ W m}^{-1} \text{ K}^{-1}$ as determined in Chapter 5.5. The just developed thermo-kinetic model as described in Chapter 6.2 is utilized in this cascading failure model to solve for the energy release kinetics by each failed LIB. The radiative heat loss from the surfaces was governed by its emissivity, ε . The emissivity of Kaowool PM is set to be 0.7 based on previous study [70-73]. The emissivity of LIBs' surfaces is set to be 0.5 as defined in Chapter 5.2. The temperature dependent natural convection coefficient as previously defined and shown in Figure 41 is also adopted in this cascading failure model for all the top surfaces of the LIBs. In addition, the same convection coefficient is also applied to all the insulation material outside surfaces. Because the insulation surface temperature is kept relatively

low throughout the simulation, the impact of using the same convection coefficient here is believed to be minor. In turns, simplifying the boundary conditions can help improve the simulation efficiency.

The LIBs are closely sitting next to each other in the model, and air is filled in the gaps in between all the LIBs. The air in this model is set to be static “gel” at constant atmospheric pressure. The default thermal properties of air in COMSOL are expressed by following equations [84-86]:

$$\rho_{air} = \frac{101325 \times 0.02897}{8.314 \times T} = \frac{353.1}{T} \quad [\text{kg m}^{-3}] \quad (21)$$

$$C_p = 1.3^{-10} \times T^4 - 6.0^{-7} \times T^3 + 9.5^{-4} \times T^2 - 0.4 \times T + 1047.6 \quad [\text{J kg}^{-1} \text{K}^{-1}] \quad (22)$$

$$k = -7.4 \times 10^{-15} \times T^4 + 4.1 \times 10^{-11} \times T^3 - 7.9 \times 10^{-8} \times T^2 + 1.2 \times 10^{-4} \times T - 2.3 \times 10^{-3} \quad [\text{W m}^{-1} \text{K}^{-1}] \quad (23)$$

The heat transfer from LIB to LIB is mainly by conduction via the air filled in LIB gaps as well as the direct contact between the LIBs. The conductive heat transfer directly from LIB to LIB is through the extremely small contacting areas that are about 0.04 mm² in the model. The size of these areas determined how fast the heat transfer directly from LIB to LIIB and these areas are independent of the mesh size. To guarantee that the conductive heat transfer via these contacting areas are effectively and reasonably taken into consideration, COMSOL can automatically reduce the local mesh size at these critical areas to an extremely small level. In this way, there will be enough amount of finite elements in these small areas to ensure simulation accuracy. For example, among the three meshing size utilized in this propagation model, no matter how globally coarse the mesh was set at, there were always at least ten finite elements assigned along these extremely small contacting areas. Moreover, COMSOL uses continuous meshing across these areas to eliminate the contact resistance.

The 40 W electrical heater was also simulated by distributing the supplied electrical power in a form of heat flux at the heater surface – the 1/3 side of the 1st row LIB. In simulation, this heater is turned on from the beginning to initiate the cascading battery thermal failure. Three different mesh options were selected in this model where average element volume are 2.2×10^{-8} , 3.9×10^{-8} and $6.2 \times 10^{-8} \text{ m}^3$, respectively. The default time step was set at 1s, and this time step can be automatically reduced in COMSOL to benefit the simulation convergence and accuracy at the points where chemical reaction rate is fast (e.g. at the onset of LIB thermal runaway). Temperatures at the same locations as TC#1 – TC#4 in experiments were calculated in the simulations. Additionally, the average temperature of each LIB was also calculated to determine the onset of thermal runaway.

Simulations were firstly ran with and without the face to face radiation in between LIBs taken in to account. The simulated temperature profiles and time to thermal runaway were found to be comparable in these two cases, indicating that the impact of this face to face radiation on the heat transfer along the battery pack was negligible. This factor was then removed from the model to improve simulation efficiency.

6.4.2 Modeling Results of Cascading Battery Failure

It should be noted that the initial value of thermal conductivity – $1.0 \text{ W m}^{-1} \text{ K}^{-1}$ – was quantified as the “radial thermal conductivity”. The heat transfer paths in this cascading battery failure simulation was actually significantly different because of the complex jelly-roll internal structure of the modeled LIB. In this cascading battery failure configuration, however, heat is transferred in the non-radial directions. For example, heat is likely to transfer faster along the steel casing and much slower along the central portion

of the cylindrical LIB. Thus it was suspected that this initial thermal conductivity value was not sufficient for accurate heat transfer simulations. To verify this, simulations of the temperature profiles during the first 250s in this cascading failure battery pack were firstly conducted and compared to experimental temperature measurements (TC#1 – TC#4). This period of time was selected because there were no significant physical or chemical changes taking place in the tested LIB cells yet. The simulated temperatures are compared to experimental measurements in Figure 52.

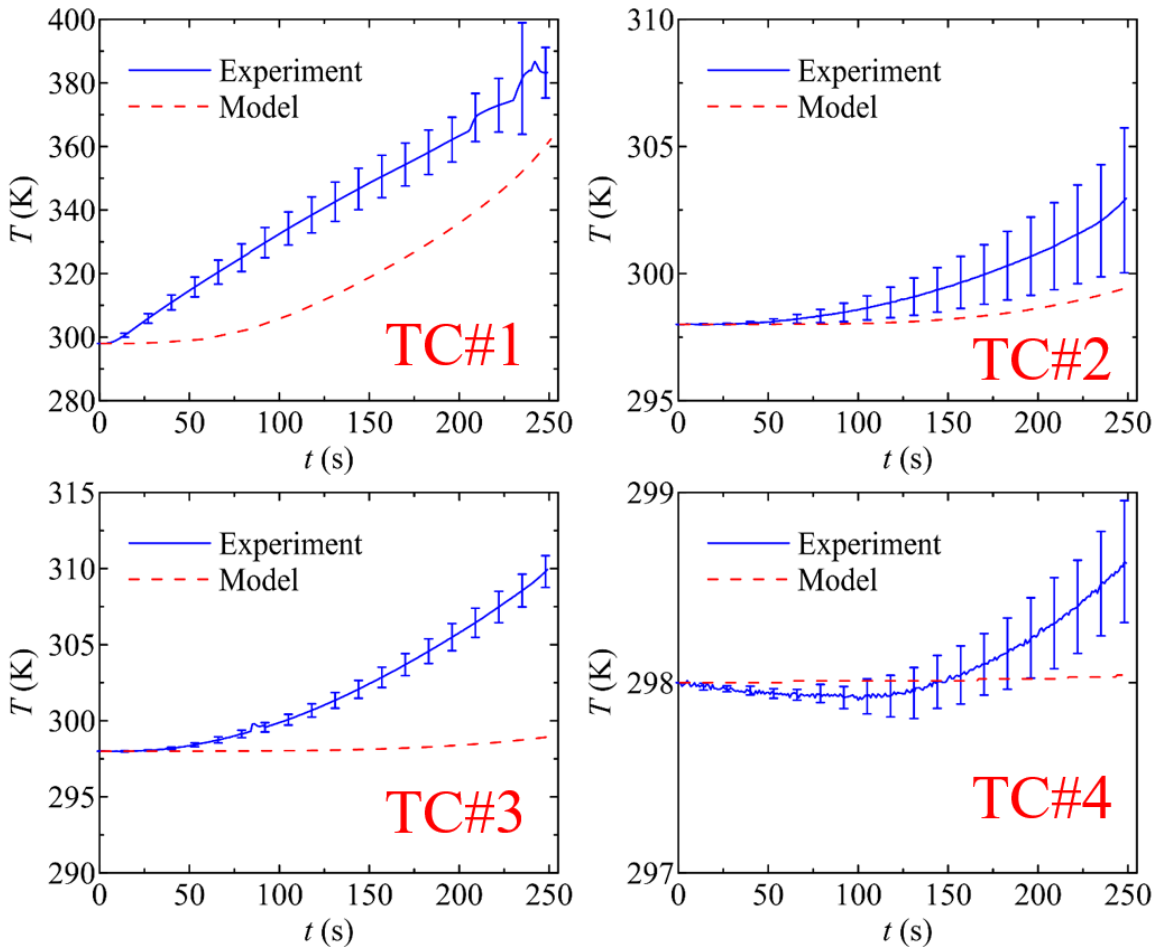


Figure 52. Results of simulation of the LIB cascading failure in billiard battery pack with $k_{LIB} = 1.0 \text{ W m}^{-1} \text{ K}^{-1}$, TC#1 to TC#4 measurements from the battery pack is simulated and compared with the experimental data.

The experimental temperature data turned out to be much under-estimated by the simulations. These discrepancies have proved that the radial thermal conductivity of this LIB was not sufficient to capture the heat transport mechanism in this cascading failure battery pack.

Efforts were taken to determine the effective thermal conductivity of the LIB cells so that the heat transfer mechanism can be better simulated. Much improved agreements in between experimental data and simulation results were found when the effective thermal conductivity of the LIB was increased to $2.6 \text{ W m}^{-1} \text{ K}^{-1}$. Figure 53 shows the comparisons at all of the four temperature measurements. This value was then carried on for the following cascading battery failure simulations.

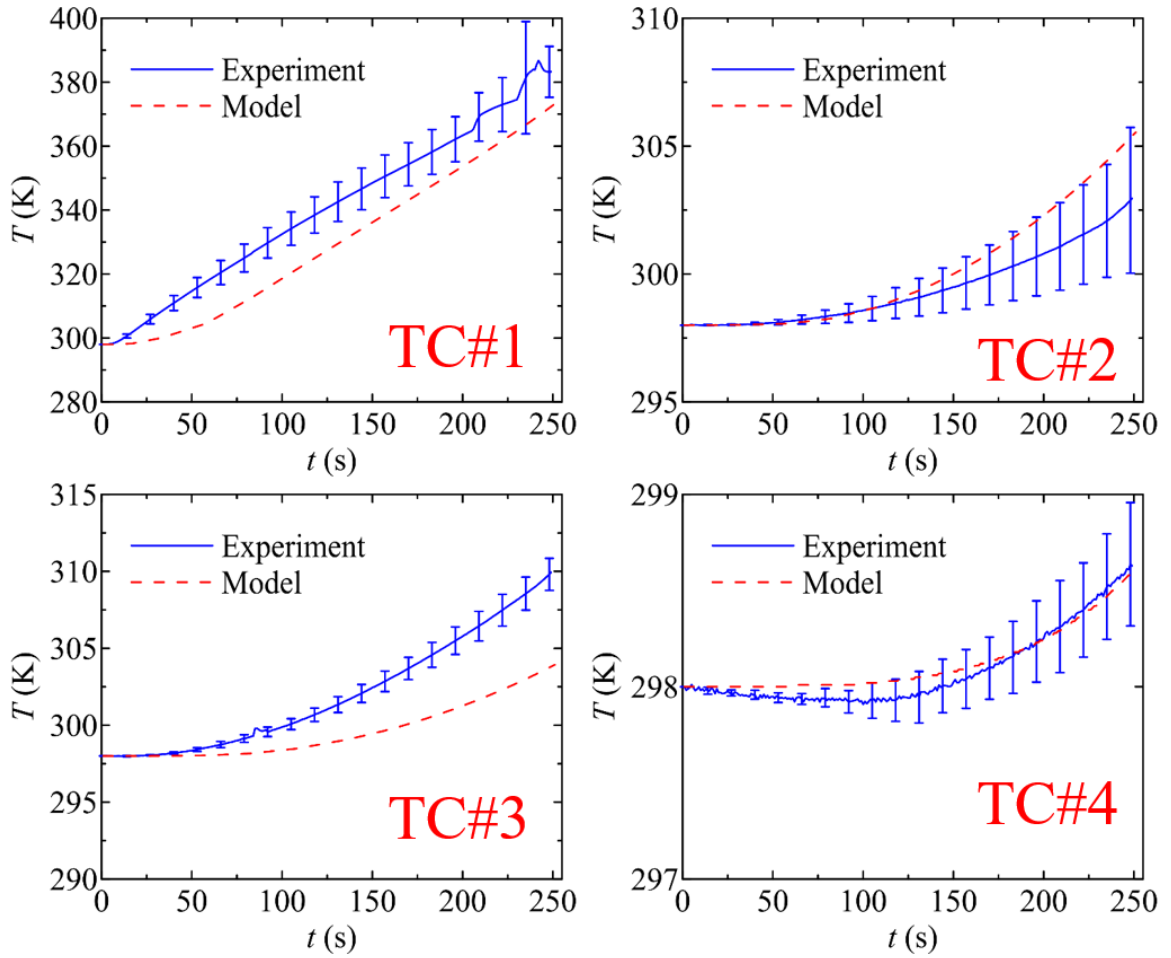


Figure 53. Results of simulation of the LIB cascading failure in billiard battery pack with $k_{LIB} = 2.6 \text{ W m}^{-1} \text{ K}^{-1}$, TC#1 to TC#4 measurements from the battery pack is simulated and compared with the experimental data.

At this point, the model configuration is finished and it's ready to simulate the entire cascading battery failure experiment. Figure 54 shows how LIB failure was propagating in this simulation.

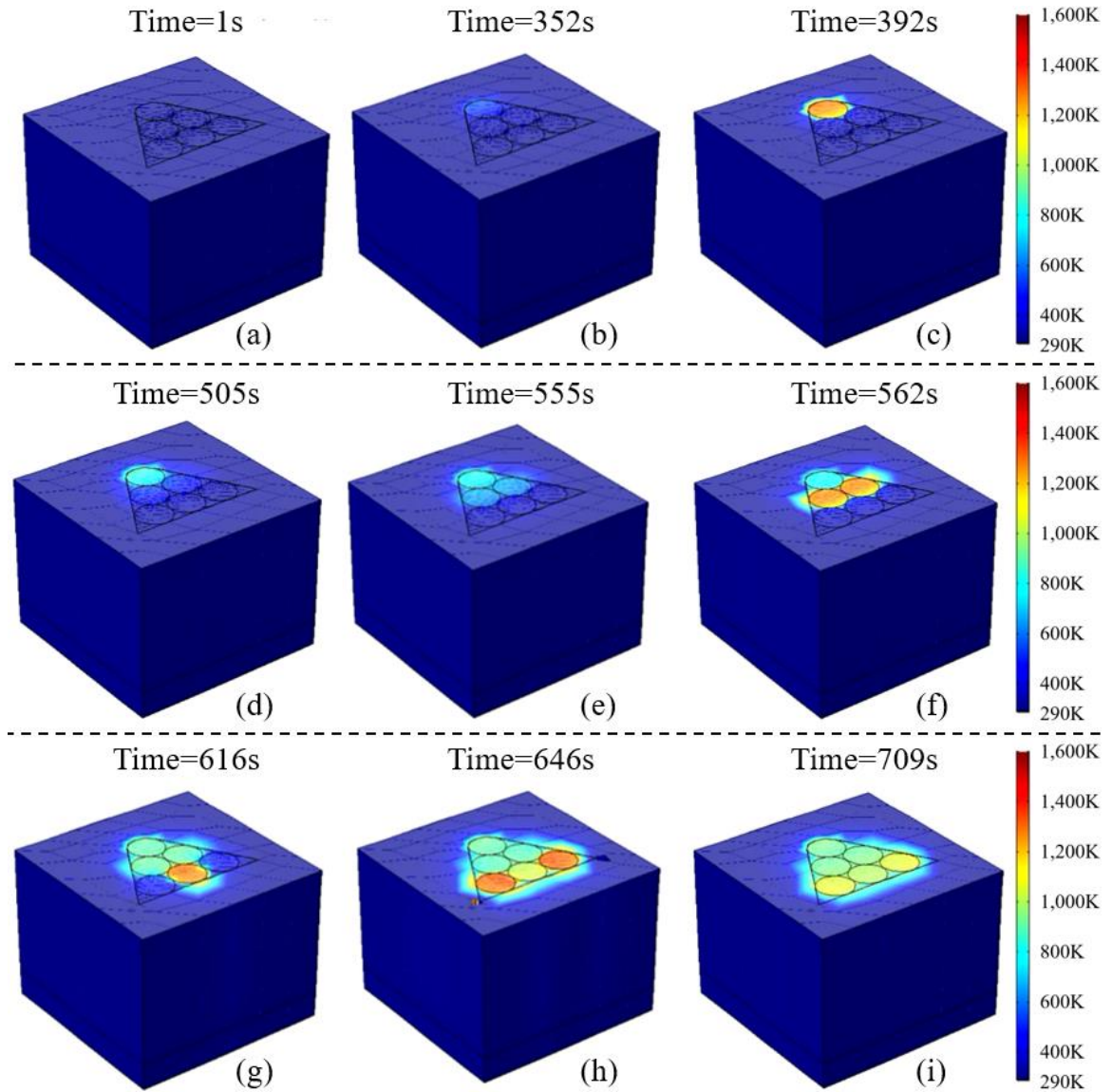


Figure 54. Simulated cascading battery failure behaviors, 0 mm spacing test in nitrogen. (a) – (c) show thermal runaway of the 1st row LIB, (d) – (f) show thermal runaway of the 2nd row LIBs, (g) – (i) show thermal runaway of the 3rd row LIBs.

In all the experiments conducted so far in this study, the onset of thermal runaway was defined as “the point of observing a sudden boost of venting intensity along with a sharp increase in T_{slug} measurement”. In simulations, however, the boost of venting is not simulated thus can’t be observed, only the detailed temperature profiles are calculated by the model. So, in this cascading battery failure model, the definition of the onset of

thermal runaway is based on the simulated temperature profile: the point where the increasing rate of the average LIB temperature is at its peak. Based on the observations from hundreds of experiments in this study, this slightly altered definition for simulation is believed to be reasonable.

The time to thermal runaway for each row of LIB with all three different meshing sizes (green circles) were then compared to the experimental measurements (red triangles) in Figure 55. To ensure consistency of thermal boundary conditions (the absence of external flaming in simulations), the model results are compared to 0 mm spacing tests in nitrogen.

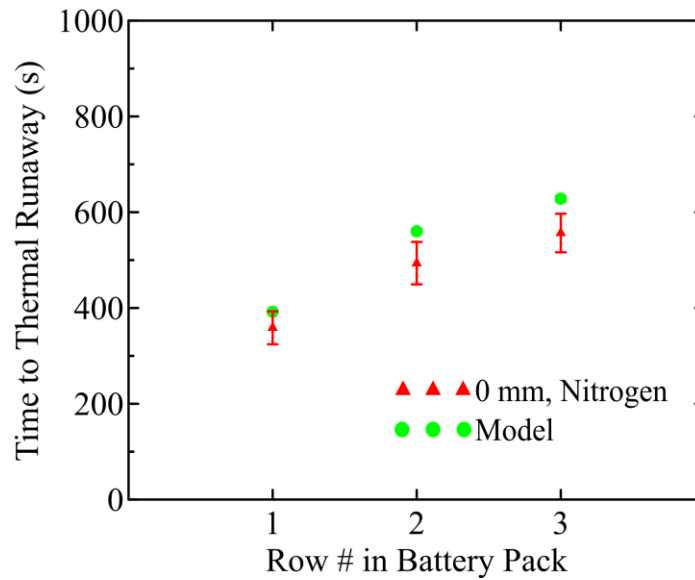


Figure 55. Results of simulation of the LIB cascading failure in billiard battery pack with $k_{LIB} = 2.6 \text{ W m}^{-1} \text{ K}^{-1}$, onset time of thermal runaway for each LIB in the battery pack is simulated with 3 different meshing sizes and compared with the experimental measurements.

Figure 55 shows negligible uncertainties for model data, which indicates that the different meshing sizes adopted in the simulation had no impact on the simulation results. It also shows that the onset time of thermal runaway for all LIBs in the battery pack were over-predicted (by 10%, 13% and 13% for 1st row, 2nd row and 3rd row, respectively).

The simulated result for LIB in 1st row is within the experimental uncertainties, while those for LIBs in 2nd and 3rd rows are out of experimental uncertainties. The slightly different definitions of the onset of thermal runaway in experiment (the point where there is a sudden boost of venting of battery materials and sharp increase of copper slug temperature) and in cascading battery failure simulation (the point where the increasing rate of the average LIB temperature reaches its peak) can contribute to these over-predictions. The pattern that, the failure propagates from 2nd row to 3rd row much faster than it does from 1st row to 2nd row, was well captured by the simulation. With the complexity of this simulation taken into consideration, the modeled results were found to be satisfactory.

Chapter 7: Conclusions

This dissertation presents efforts toward addressing the lithium ion battery (LIB) safety issue by developing and implementing a systematic methodology that includes both experimental quantification and numerical modeling of LIB's thermally-induced failure.

Copper Slug Battery Calorimetry (CSBC) is a newly developed experimental technique in this study for the characterization of thermal properties of LIBs and the measurement of the energetics of a thermally-induced failure of LIBs. This technique was demonstrated by investigating a widely used 18650-type LIB at various states of charge (SOCs). It was shown that this technique yields time and temperature resolved data on the rate of heat production inside a failing battery. The technique was found to be sufficiently sensitive to detect minor endothermic processes (such as vaporization of electrolyte) and exothermic chemical decomposition in fully discharged battery specimens. The integral heat production data were found to be highly repeatable. While this technique was used to measure only the heat released inside the battery casing, it was demonstrated how a relationship between the amount of ejected material and the total internal energy released (P_{IHG} Integral) observed for the 100% SOC batteries can be used to estimate the maximum energy that can be produced by reacting battery materials, assuming that all of them are allowed to react to completion in the absence of atmospheric oxygen. The CSBC was also coupled with cone calorimetry to enable measurement of the energy released due to a reaction of ejected battery materials with environmental oxygen in a non-premixed flame. The heats of flaming combustion ($P_{Flaming}$) associated with safety venting and thermal runaway phases of failure were

determined and their dependence on SOC was elucidated. It was found that the hot wire igniter (which was used to initiate and maintain combustion of the ejected materials) and the energy produced by continuous flaming combustion interfered with the CSBC internal energy release measurement, thus the CSBC and cone calorimetry technique cannot be combined into a single, simultaneous measurement technique.

This systematic experimental technique was utilized to investigate LIBs with 3 different battery chemistries: lithium cobalt oxide (T-Energy ICR18650, LCO), lithium nickel manganese cobalt oxide (Panasonic CGR18650CG, NMC) and lithium iron phosphate (K2 18650E, LFP), at various states of charge (SOCs). The heat capacity of these LIBs was evaluated to be $1.1 \pm 0.1 \text{ J g}^{-1} \text{ K}^{-1}$ for all three cathode types. It was shown that the total heat generated inside the batteries increases with increasing amount of electrical energy stored. The maximum total internal heat generated by fully-charged LIBs was found to be 37.3 ± 3.3 , 34.0 ± 1.8 and $13.7 \pm 0.4 \text{ kJ/cell}$ for LCO, NMC and LFP LIBs, respectively. Additionally, experiments were carried out in which the CSBC technique was combined with cone calorimetry to measure the heat produced in flaming combustion of vented battery materials. The released combustion heat did not show a clear dependence on the stored electrical energy; this heat varied between 35 and 63 kJ/cell for LCO LIBs, 27 and 81 kJ/cell for NMC LIBs, and 36 and 50 kJ/cell for LFP LIBs.

Beyond the experimental work, detailed heat transfer numerical modeling of the CSBC experiments was carried out on COMSOL software platform. The radial thermal conductivities of the LCO, NMC and LFP LIB cells were evaluated 1.0 ± 0.1 , 0.4 ± 0.1 and $0.4 \pm 0.1 \text{ W m}^{-1} \text{ K}^{-1}$, respectively. Moreover, this numerical modeling practice has

demonstrated the satisfactory accuracy of CSBC experimental analysis in the determination of the battery failure energetics for all examined battery types. Last but not least, a general methodology is presented in this dissertation to develop a thermo-kinetic model of thermally-induced failure of lithium ion batteries (LIBs), using COMSOL and experimental data collected by CSBC. This methodology is demonstrated specifically on LCO LIBs (T-Energy ICR18650), but it can be easily extended to other battery types. The model was parameterized based on Arrhenius' Law and via an iterative inverse modeling analysis of CSBC test results using COMSOL. These model parameters are dependent on the cells' states of charge (SOCs) and they can effectively represent the tested cells' heat production energetics during failure. The fully-parameterized thermo-kinetic model was then validated against CSBC tests that were not utilized in the model parameterization, and excellent agreement (within 5% on average) was found between experimental data and simulated results. To further validate the extrapolation power of this fully-developed thermo-kinetic model of LIB thermal failure, it is utilized in a more complex battery failure scenario – cascading battery thermal failure of 6 LCO LIBs in a billiard battery pack. Thermal conductivity of the battery was adjusted from $1.0 \text{ W m}^{-1} \text{ K}^{-1}$ to $2.6 \text{ W m}^{-1} \text{ K}^{-1}$ to fit the totally different heat transfer paths (from CSBC to cascading failure battery pack). Without changing the model's chemical kinetic parameters, it was found that the time to thermal runaway of each battery in this cascading failure was well predicted.

The major advantages of this systematic methodology include the following aspects: 1). The CSBC technique is easy to implement and ready to be adjusted to fit other form factors of LIB. 2). The CSBC technique can accurately capture not only

internal energetics but also external battery failure behavior, providing an integral understanding of potential battery thermal hazards. 3). Comparisons between the results obtained for different battery types (e.g. form factors, electrode chemistries, etc.) can provide insightful information to help better understand and optimize battery chemistries from the aspect of thermal safety. It can also help evaluate different battery protection mechanisms. 4). The novel way presented in this dissertation to construct the thermo-kinetic model is more straightforward and it doesn't require information such as: detailed internal structure of an LIB, thermal properties of each battery material, chemical reaction mechanism for each reaction in the battery during its failure. 5). The thermo-kinetic model has shown its capability of being utilized to adequately predict battery failure behavior in more complex scenarios – cascading battery failure test.

Chapter 8: Future Work

As an extension of current study, future work can include the following aspects:

1). To apply CSBC experimental technique to investigate thermally-induced failure behaviors of other form factors and chemistries of LIBs. These investigations can form a foundation of a battery safety database, which can provide fast and effective reference for future development of LIB technology from safety perspective. 2). To modify cascading battery failure experimental setup to evaluate the heat feedback from flaming combustion of vented battery material to LIBs during its failure propagation. And add these properties to the current version of cascading battery failure model to enable it to simulate cascading battery failure in air. 3). After this model is complete and validated, it can be employed to explore possible battery fire suppression methodologies, to help identify the most effective and cost-efficient way for battery fire suppression.

Reference

- [1] P. Balakrishnan, R. Ramesh, T. Prem Kumar, Safety mechanisms in lithium-ion batteries, *Journal of Power Sources*, 155 (2006) 401-414.
- [2] Q. Wang, P. Ping, X. Zhao, G. Chu, J. Sun, C. Chen, Thermal runaway caused fire and explosion of lithium ion battery, *Journal of Power Sources*, 208 (2012) 210-224.
- [3] M. Yang, J. Hou, Membranes in lithium ion batteries, *Membranes*, 2 (2012) 367-383.
- [4] T.M. Bandhauer, S. Garimella, T.F. Fuller, A critical review of thermal issues in lithium-ion batteries, *Journal of The Electrochemical Society*, 158 (2011) R1-R25.
- [5] J. Jeevarajan, W. Tracinski, Performance and Safety Tests of Lithium-Ion Cells Arranged in a Matrix Design Configuration, (2010).
- [6] J.A. Jeevarajan, Safety limitations associated with commercial 18650 lithium-ion cells, (2010).
- [7] R. Spotnitz, J. Franklin, Abuse behavior of high-power, lithium-ion cells, *Journal of Power Sources*, 113 (2003) 81-100.
- [8] X. Liu, Z. Wu, S.I. Stolarov, M. Denlinger, A. Masias, K. Snyder, Heat release during thermally-induced failure of a lithium ion battery: Impact of cathode composition, *Fire Safety Journal*, 85 (2016) 10-22.
- [9] K. Zaghbi, J. Dubé, A. Dallaire, K. Galoustov, A. Guerfi, M. Ramanathan, A. Benmayza, J. Prakash, A. Mauger, C. Julien, Enhanced thermal safety and high power performance of carbon-coated LiFePO₄ olivine cathode for Li-ion batteries, *Journal of Power Sources*, 219 (2012) 36-44.

- [10] M.-S. Wu, P.-C.J. Chiang, J.-C. Lin, Y.-S. Jan, Correlation between electrochemical characteristics and thermal stability of advanced lithium-ion batteries in abuse tests—short-circuit tests, *Electrochimica acta*, 49 (2004) 1803-1812.
- [11] S.-i. Tobishima, K. Takei, Y. Sakurai, J.-i. Yamaki, Lithium ion cell safety, *Journal of Power Sources*, 90 (2000) 188-195.
- [12] E. Roth, D. Doughty, Thermal abuse performance of high-power 18650 Li-ion cells, *Journal of Power Sources*, 128 (2004) 308-318.
- [13] D.H. Doughty, P.C. Butler, R.G. Jungst, E.P. Roth, Lithium battery thermal models, *Journal of Power Sources*, 110 (2002) 357-363.
- [14] K. Smith, G.H. Kim, E. Darcy, A. Pesaran, Thermal/electrical modeling for abuse-tolerant design of lithium ion modules, *International Journal of Energy Research*, 34 (2010) 204-215.
- [15] D. Doughty, E.P. Roth, A general discussion of Li ion battery safety, *Electrochemical Society Interface*, 21 (2012) 37-44.
- [16] D.H. Doughty, E.P. Roth, C.C. Crafts, G. Nagasubramanian, G. Henriksen, K. Amine, Effects of additives on thermal stability of Li ion cells, *Journal of Power Sources*, 146 (2005) 116-120.
- [17] M. Kise, S. Yoshioka, H. Kuriki, Relation between composition of the positive electrode and cell performance and safety of lithium-ion PTC batteries, *Journal of Power Sources*, 174 (2007) 861-866.
- [18] H. Yang, H. Bang, K. Amine, J. Prakash, Investigations of the exothermic reactions of natural graphite anode for Li-ion batteries during thermal runaway, *Journal of The Electrochemical Society*, 152 (2005) A73-A79.

- [19] P. Biensan, B. Simon, J. Peres, A. De Guibert, M. Broussely, J. Bodet, F. Perton, On safety of lithium-ion cells, *Journal of Power Sources*, 81 (1999) 906-912.
- [20] D. Choi, J. Xiao, Y.J. Choi, J.S. Hardy, M. Vijayakumar, M. Bhuvaneshwari, J. Liu, W. Xu, W. Wang, Z. Yang, Thermal stability and phase transformation of electrochemically charged/discharged LiMnPO₄ cathode for Li-ion batteries, *Energy & Environmental Science*, 4 (2011) 4560-4566.
- [21] A. Du Pasquier, F. Disma, T. Bowmer, A. Gozdz, G. Amatucci, J.M. Tarascon, Differential Scanning Calorimetry Study of the Reactivity of Carbon Anodes in Plastic Li-Ion Batteries, *Journal of The Electrochemical Society*, 145 (1998) 472-477.
- [22] C.-Y. Wen, C.-Y. Jhu, Y.-W. Wang, C.-C. Chiang, C.-M. Shu, Thermal runaway features of 18650 lithium-ion batteries for LiFePO₄ cathode material by DSC and VSP2, *Journal of thermal analysis and calorimetry*, 109 (2012) 1297-1302.
- [23] E. Roth, D. Doughty, J. Franklin, DSC investigation of exothermic reactions occurring at elevated temperatures in lithium-ion anodes containing PVDF-based binders, *Journal of Power Sources*, 134 (2004) 222-234.
- [24] E.P. Roth, C.C. Crafts, D.H. Doughty, J. McBreen, advanced technology development program for Lithium-ion Batteries: thermal abuse performance of 18650 Li-ion cells, Sandia National Laboratories, Albuquerque, NM. SAND2004-0584, (2004).
- [25] H. Maleki, G. Deng, A. Anani, J. Howard, Thermal Stability Studies of Li-Ion Cells and Components, *Journal of The Electrochemical Society*, 146 (1999) 3224-3229.
- [26] H. Maleki, J.N. Howard, Role of the cathode and anode in heat generation of Li-ion cells as a function of state of charge, *Journal of Power Sources*, 137 (2004) 117-127.

- [27] U. von Sacken, E. Nodwell, A. Sundher, J. Dahn, Comparative thermal stability of carbon intercalation anodes and lithium metal anodes for rechargeable lithium batteries, *Journal of Power Sources*, 54 (1995) 240-245.
- [28] R.M. Spotnitz, J. Weaver, G. Yeduvaka, D. Doughty, E. Roth, Simulation of abuse tolerance of lithium-ion battery packs, *Journal of Power Sources*, 163 (2007) 1080-1086.
- [29] A. Eddahech, O. Briat, J.-M. Vinassa, Thermal characterization of a high-power lithium-ion battery: Potentiometric and calorimetric measurement of entropy changes, *Energy*, 61 (2013) 432-439.
- [30] D. Abraham, E. Roth, R. Kosteki, K. McCarthy, S. MacLaren, D. Doughty, Diagnostic examination of thermally abused high-power lithium-ion cells, *Journal of Power Sources*, 161 (2006) 648-657.
- [31] M. Richard, J. Dahn, Accelerating rate calorimetry study on the thermal stability of lithium intercalated graphite in electrolyte. I. Experimental, *Journal of The Electrochemical Society*, 146 (1999) 2068-2077.
- [32] C.-Y. Jhu, Y.-W. Wang, C.-M. Shu, J.-C. Chang, H.-C. Wu, Thermal explosion hazards on 18650 lithium ion batteries with a VSP2 adiabatic calorimeter, *J Hazard Mater*, 192 (2011) 99-107.
- [33] C.-Y. Jhu, Y.-W. Wang, C.-Y. Wen, C.-M. Shu, Thermal runaway potential of LiCoO₂ and Li (Ni_{1/3}Co_{1/3}Mn_{1/3}) O₂ batteries determined with adiabatic calorimetry methodology, *Applied Energy*, 100 (2012) 127-131.
- [34] C.-Y. Jhu, Y.-W. Wang, C.-Y. Wen, C.-C. Chiang, C.-M. Shu, Self-reactive rating of thermal runaway hazards on 18650 lithium-ion batteries, *Journal of thermal analysis and calorimetry*, 106 (2011) 159-163.

- [35] Q. Wang, J. Sun, X. Yao, C. Chen, Micro calorimeter study on the thermal stability of lithium-ion battery electrolytes, *Journal of Loss Prevention in the Process Industries*, 19 (2006) 561-569.
- [36] Q. Wang, J. Sun, C. Chen, Effects of solvents and salt on the thermal stability of lithiated graphite used in lithium ion battery, *J Hazard Mater*, 167 (2009) 1209-1214.
- [37] Q. Wang, J. Sun, X. Yao, C. Chen, Thermal behavior of lithiated graphite with electrolyte in lithium-ion batteries, *Journal of The Electrochemical Society*, 153 (2006) A329-A333.
- [38] P. Ribière, S. Grugeon, M. Morcrette, S. Boyanov, S. Laruelle, G. Marlair, Investigation on the fire-induced hazards of Li-ion battery cells by fire calorimetry, *Energy & Environmental Science*, 5 (2012) 5271-5280.
- [39] D. Townsend, J. Tou, Thermal hazard evaluation by an accelerating rate calorimeter, *Thermochimica Acta*, 37 (1980) 1-30.
- [40] S. Al Hallaj, H. Maleki, J.-S. Hong, J.R. Selman, Thermal modeling and design considerations of lithium-ion batteries, *Journal of Power Sources*, 83 (1999) 1-8.
- [41] R.E. Lyon, R.N. Walters, Energetics of lithium ion battery failure, *J Hazard Mater*, 318 (2016) 164-172.
- [42] R. Walters, R. Lyon, Measuring energy release of lithium ion battery failure using a bomb calorimeter, *FAA Report DOT/FAA/TC-15/40*, 2016.
- [43] C.R. Pals, J. Newman, Thermal modeling of the lithium/polymer battery I. Discharge behavior of a single cell, *Journal of the Electrochemical Society*, 142 (1995) 3274-3281.

- [44] C.R. Pals, J. Newman, Thermal modeling of the lithium/polymer battery II. Temperature profiles in a cell stack, *Journal of the Electrochemical Society*, 142 (1995) 3282-3288.
- [45] C. Forgez, D.V. Do, G. Friedrich, M. Morcrette, C. Delacourt, Thermal modeling of a cylindrical LiFePO₄/graphite lithium-ion battery, *Journal of Power Sources*, 195 (2010) 2961-2968.
- [46] S.C. Chen, Y.Y. Wang, C.C. Wan, Thermal analysis of spirally wound lithium batteries, *Journal of the Electrochemical Society*, 153 (2006) A637-A648.
- [47] S.C. Chen, C.C. Wan, Y.Y. Wang, Thermal analysis of lithium-ion batteries, *Journal of Power Sources*, 140 (2005) 111-124.
- [48] Y. Chen, J.W. Evans, Thermal Analysis of Lithium-Ion Batteries, *Journal of The Electrochemical Society*, 143 (1996) 2708-2712.
- [49] Y. Chen, J.W. Evans, Three-Dimensional Thermal Modeling of Lithium-Polymer Batteries under Galvanostatic Discharge and Dynamic Power Profile, *Journal of The Electrochemical Society*, 141 (1994) 2947-2955.
- [50] G.H. Kim, A. Pesaran, R. Spotnitz, A three-dimensional thermal abuse model for lithium-ion cells, *Journal of Power Sources*, 170 (2007) 476-489.
- [51] T. Hatchard, D. MacNeil, A. Basu, J. Dahn, Thermal model of cylindrical and prismatic lithium-ion cells, *Journal of the Electrochemical Society*, 148 (2001) A755-A761.
- [52] G.F. Guo, B. Long, B. Cheng, S.Q. Zhou, P. Xu, B.G. Cao, Three-dimensional thermal finite element modeling of lithium-ion battery in thermal abuse application, *Journal of Power Sources*, 195 (2010) 2393-2398.

- [53] S. Santhanagopalan, P. Ramadass, J. Zhang, Analysis of internal short-circuit in a lithium ion cell, *Journal of Power Sources*, 194 (2009) 550-557.
- [54] S. Santhanagopalan, Q.Z. Guo, P. Ramadass, R.E. White, Review of models for predicting the cycling performance of lithium ion batteries, *Journal Of Power Sources*, 156 (2006) 620-628.
- [55] X.W. Zhang, Thermal analysis of a cylindrical lithium-ion battery, *Electrochimica Acta*, 56 (2011) 1246-1255.
- [56] D.H. Jeon, S.M. Baek, Thermal modeling of cylindrical lithium ion battery during discharge cycle, *Energy Conversion and Management*, 52 (2011) 2973-2981.
- [57] W. Fang, O.J. Kwon, C.Y. Wang, Electrochemical–thermal modeling of automotive Li-ion batteries and experimental validation using a three-electrode cell, *International Journal of Energy Research*, 34 (2010) 107-115.
- [58] M. Guo, G. Sikha, R.E. White, Single-particle model for a lithium-ion cell: Thermal behavior, *Journal of the Electrochemical Society*, 158 (2011) A122-A132.
- [59] S. Santhanagopalan, R.E. White, State of charge estimation using an unscented filter for high power lithium ion cells, *International Journal of Energy Research*, 34 (2010) 152-163.
- [60] L. Cai, R.E. White, An Efficient Electrochemical–Thermal Model for a Lithium-Ion Cell by Using the Proper Orthogonal Decomposition Method, *Journal of the Electrochemical Society*, 157 (2010) A1188-A1195.
- [61] L. Cai, R.E. White, Mathematical modeling of a lithium ion battery with thermal effects in COMSOL Inc. Multiphysics (MP) software, *Journal of Power Sources*, 196 (2011) 5985-5989.

- [62] R.M. Spotnitz, J. Weaver, G. Yeduvaka, D.H. Doughty, E.P. Roth, Simulation of abuse tolerance of lithium-ion battery packs, *Journal of Power Sources*, 163 (2007) 1080-1086.
- [63] C.F. Lopez, J.A. Jeevarajan, P.P. Mukherjee, Characterization of Lithium-Ion Battery Thermal Abuse Behavior Using Experimental and Computational Analysis, *Journal of The Electrochemical Society*, 162 (2015) A2163-A2173.
- [64] X. Liu, S.I. Stoliarov, M. Denlinger, A. Masias, K. Snyder, Comprehensive Calorimetry of the Thermally-Induced Failure of a Lithium Ion Battery, *Journal of Power Sources*, (2015).
- [65] ASTM E 1354-09: Standard Test Method for Heat and Visible Smoke Release Rates for Materials and Products Using an Oxygen Consumption Calorimeter, American Society for Testing and Materials, Philadelphia, PA., (1990).
- [66] COMSOL Multiphysics User's Guide, COMSOL Multiphysics User's Guide, Version: 5.0, (2014).
- [67] T-Energy ICR18650 Lithium Ion Battery Specification Approval Sheet, www.tenergybattery.com.
- [68] Product Safety Data Sheet: Panasonic CGR18650CG Lithium Ion Battery, Document No.: LIC-PSDS-2011-020, (2011).
- [69] High Capacity K218650E02 Energy Cell Data Sheet, https://www.master-instruments.com.au/cgi/ajax/get_file/62567/1.
- [70] M.A. Materials, Organic RCF Vacuum Formed Products, Datasheet Code US: 514-700.

- [71] M. McKinnon, Development of a model for flaming combustion of double-wall corrugated cardboard, Master of Science, University of Maryland, 2012.
- [72] M.R. Semmes, X. Liu, M.B. McKinnon, S.I. Stoliarov, A. Witkowski, A model for oxidative pyrolysis of corrugated cardboard, *Fire Safety Science*, 11 (2014).
- [73] X. Liu, Design and analysis of new gasification apparatus based on the standard cone calorimeter, Master of Science, University of Maryland, 2012.
- [74] F.P. Incropera, *Fundamentals of heat and mass transfer*, John Wiley & Sons, 2007.
- [75] M.W. Chase, Jr., NIST-JANAF thermochemical tables, Fourth Edition, *Journal of Physical Chemical Reference Data*, Monograph 9, (1998) 1-1951.
- [76] H. Maleki, S. Al Hallaj, J.R. Selman, R.B. Dinwiddie, H. Wang, Thermal Properties of Lithium-Ion Battery and Components, *Journal of The Electrochemical Society*, 146 (1999) 947-954.
- [77] H. Kawaji, T. Oka, T. Tojo, T. Atake, A. Hirano, R. Kanno, Low-temperature heat capacity of layer structure lithium nickel oxide, *Solid state ionics*, 152 (2002) 195-198.
- [78] J.G. Quintiere, S.B. Crowley, R.N. Walters, R.E. Lyon, D. Blake, *Fire Hazards of Lithium Batteries*, DOT/FAA/TC-TN15/17 (2016).
- [79] W.M. Haynes, *CRC handbook of chemistry and physics*, CRC press, 2013.
- [80] J. Holman, *Heat transfer*, 9th Edition, McGraw-Hill, Inc, New York, Boston, 2002.
- [81] S. Chen, C. Wan, Y. Wang, Thermal analysis of lithium-ion batteries, *Journal of Power Sources*, 140 (2005) 111-124.
- [82] J.D. Menczel, R.B. Prime, *Thermal analysis of polymers, fundamentals and applications*, John Wiley & Sons, 2009.

[83] J. Li, S.I. Stoliarov, Measurement of kinetics and thermodynamics of the thermal degradation for non-charring polymers, *Combustion and Flame*, 160 (2013) 1287-1297.

[84] ASHRAE Handbook of Fundamentals, American society of heating, Refrigerating and air conditioning engineers, 1993.

[85] E.R.G. Eckert and M. Drake, Jr., Analysis of heat and mass transfer, Hemisphere Publishing, 1987.

[86] R.C. Weast, M.J. Astle, W.H. Beyer, CRC handbook of chemistry and physics, CRC press, Boca Raton, FL, 1988.